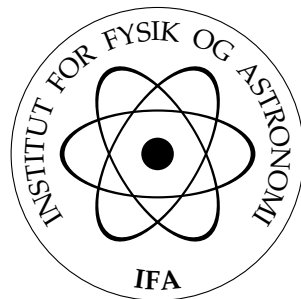

STRONG FIELD DYNAMICS

Scattering and Multiphoton Ionization

Lars Bojer Madsen

Institute of Physics and Astronomy
University of Aarhus



1998

Contents

Preface	v
List of publications	v
Acknowledgements	vi
1 Prologue	1
1.1 Thesis outline	2
2 Introduction to laser-assisted electron scattering	5
2.1 The Kroll-Watson theory	5
2.2 Current experimental and theoretical work	7
2.3 Questions addressed in this thesis	8
3 Classical theory of laser-assisted electron scattering	11
3.1 Quiver amplitude, ponderomotive potential and intensity	11
3.2 Classical theory of laser-assisted electron scattering	12
4 Theory of laser-assisted electron scattering	15
4.1 Non-resonant laser-assisted electron scattering	15
4.1.1 Classically allowed laser-assisted scattering ($ l \leq L$)	16
4.1.2 The semi-classical limit, $L \gg 1$	18
4.1.3 Classically forbidden laser-assisted scattering ($ l > L$)	19
4.1.4 The weak-field soft-photon theory	20
4.2 Scattering by the zero-range potential in circularly polarized light	26
4.3 Resonant laser-assisted electron scattering	27
4.4 Two-colour laser-assisted scattering	29
5 Laser-assisted electron scattering: calculations and conclusions	33
5.1 Laser-assisted electron scattering on the zero-range potential	33
5.2 Non-resonant electron scattering on argon	40
5.3 Resonant electron scattering on argon	47
5.3.1 Well-separated resonance series	47
5.3.2 Overlapping resonances	50

6	Dispersion and quantum coherence in general and in two-colour laser-assisted electron-atom scattering in particular	57
6.1	Introduction	57
6.2	Theory of interference experiments	58
6.3	Dispersion and coherence in two-colour experiments	60
6.4	Conclusions	65
7	Introduction to multiphoton ionization of molecules	67
8	Floquet approach to multiphoton ionization of H_2^+	73
8.1	Relation to wavepacket calculations	76
9	Multiphoton ionization of H_2^+: calculations and conclusions	79
9.1	Variation of ionization rates with frequency and intensity	79
9.2	Variation of ionization rates with internuclear separation	81
9.2.1	Diabatic and 2- and 30-state adiabatic potential energy curves	81
9.2.2	Large-scale Floquet calculations	86
9.3	Comparisons of wavepacket and Floquet ionization rates	91
9.4	Conclusions	100
10	Finale	103
10.1	Outlook	103
10.1.1	Laser-assisted electron scattering	103
10.1.2	Dissociative ionization of H_2^+	103
A	The weak-field soft-photon approximation	105
B	Inverse iteration and LU decomposition	107
C	Complex-scaling and complex-basis-function methods	109
D	Resumé	111
	Bibliography	113

Preface

The present thesis gives an account of some of the work done during my Ph.D. studies. The work has been carried out at the Institute of Physics and Astronomy at the University of Aarhus in collaboration with my supervisor Knud Taulbjerg. We have studied correlation effects in electron-excitation of hydrogen, laser-assisted electron scattering and aspects of dispersion and quantum coherence. Additionally, I have had the pleasure to work together with Jim McCann and Martin Plummer on multiphoton ionization of the molecular hydrogen ion. This work has taken place in the Atomic and Molecular Physics Group at the University of Durham during a six-month stay in the spring and summer of 1997. The collaboration with McCann and Plummer has continued after my return to Aarhus.

In order to obtain a coherent presentation, I have chosen only to discuss work related to non-perturbative processes in laser fields: laser-assisted electron scattering, dispersion and quantum coherence in laser-assisted scattering (and in general), and multiphoton ionization of the hydrogen molecular ion. Accordingly, the study of correlation effects in electron-excitation of hydrogen corresponding to paper 8 below is not treated. For a detailed discussion of these effects, the reader is referred to references [1, 2]. Very recent work on laser-induced l -mixing in a degenerate Rydberg manifold, corresponding to paper 10 below, is not included either.

List of publications

1. Lars Bojer Madsen and Knud Taulbjerg: “*A simple test of theories of laser-assisted electron-atom scattering*”, J. Phys. B: At. Mol. Opt. Phys. in print (1998).
2. Lars Bojer Madsen, Martin Plummer and Jim F. McCann: “*Multiphoton ionization of H_2^+ by intense light: comparison of Floquet and wave-packet approach*”, Phys. Rev. A **58**, 456 (1998).
3. Lars Bojer Madsen and Knud Taulbjerg: “*Probe dispersion and quantum coherence*”, in “*Photonic, Electronic and Atomic Collisions*” p. 169, editors F Aumayr and H Winter, World Scientific, (1998).

4. Lars Bojer Madsen and Martin Plummer: “ H_2^+ in intense laser fields: mechanisms for enhanced ionization in the multiphoton regime”, J. Phys. B: At. Mol. Opt. Phys. **31**, 87 (1998)
5. Lars Bojer Madsen and Knud Taulbjerg: “Probe dispersion and quantum coherence”, J. Phys. B: At. Mol. Opt. Phys. **30**, L419 (1997).
6. Lars Bojer Madsen and Knud Taulbjerg: “Laser-assisted electron-atom scattering and laser-induced resonance interference”, J. Phys. B: At. Mol. Opt. Phys. **30**, 1599 (1997).
7. Lars Bojer Madsen and Knud Taulbjerg: “Theory of laser-assisted electron-atom scattering: beyond the Kroll-Watson approximation”, J. Phys. B: At. Mol. Opt. Phys. **28**, 5327 (1995).
8. Lars Bojer Madsen and Knud Taulbjerg: “Polarization effect in electron-excitation of hydrogen”, Phys. Rev. A **52**, 2429 (1995).
9. Martin Plummer, Jim F. McCann and Lars Bojer Madsen: “The calculation of multiphoton ionization rates of the hydrogen molecular ion”, Computer Physics Communications, in print (1998).
10. Halvor M. Nilsen, Jan P. Hansen and Lars Bojer Madsen: “Optical l-mixing in a degenerate Rydberg manifold”, submitted to Phys. Rev. Lett., (1998).

Parts of papers 1-7 and 9 are included in appropriate chapters of this thesis.

Acknowledgements

Useful discussions with my supervisor Knud Taulbjerg are gratefully acknowledged. Many thanks also to Jim McCann and Martin Plummer for making my stay at the University of Durham possible.

Chapter I

Prologue

This thesis will deal with multiphoton laser-assisted and -induced dynamics. The laser frequencies and intensities considered are such that the laser-matter interaction is strong. It has, accordingly, to be treated non-perturbatively and non-linear processes either dominate or play a significant rôle.

Multiphoton processes occur in electron-atom scattering in an intense field [3, 4]. Strong continuum-continuum couplings are also present in the laser-assisted photoelectric effect [5] and laser-assisted Auger decay [6]. Simple theoretical models of these processes neglect the influence of the atomic or molecular potential on the continuum electron and hence describe the asymptotic electron state by a Volkov wave [7]. These models quite generally leads to the probability, P_l , that l photons are exchanged during the process

$$P_l = J_l^2(x). \quad (1.1)$$

Here $J_l(x)$ is a Bessel function of first kind. The argument of J_l is different for different laser-assisted processes, but depends in general on the quiver radius, i.e. the excursion amplitude in the oscillatory motion of the electron, the polarization of the laser field and the momentum of the electron. Theoretical predictions based on equation (1.1) give results which agree qualitatively with experiments [4, 5, 6]. The first part of this thesis will describe the theory of laser-assisted electron scattering in detail.

The second part of the thesis discusses multiphoton ionization of H_2^+ . Compared with the atomic case which is treated in detail in the review edited by Gavrila [8], the physics of strong laser-molecule interactions is enriched and complicated by the presence of other nuclei which break the spherical symmetry of the binding potential and introduce dissociation as an additional channel of disintegration. Due to the inherent multichannel character of the problem, a coherent picture of cause and effect is only gradually emerging. To gain quantitative insight, one has to resort to computational techniques as, for example, wavepacket simulations or the Floquet approach [9]. The quantity of principal physical interest is the ionization rate, Γ . In the atomic case, Γ depends primarily on the parameters of the field: frequency, polarization, and strength. In the

case of a molecule, the internuclear distance, R , is an extra parameter. In H_2^+ the dependence of Γ on R is pronounced. A series of peaks and troughs occur in Γ as R varies. Following extensive experimental and theoretical evidence for the existence of *critical internuclear distances* [10, 11, 12, 13, 14, 15], which are larger than the equilibrium separation, and at which ionization of the molecule appears to be strongly favoured, recent theoretical studies have concentrated on calculating ionization rates as a function of R [16, 17, 18, 19, 20, 21, 22, 23, 24]. The value of knowing ionization rates as functions of R is that they can be used for predicting the energy spectra of the fragment ions, and vice versa. A preliminary estimate of critical distances can be obtained using simple classical quasistatic barrier type models [12]. To obtain the detailed structure, however, quantum calculations are required.

1.1 Thesis outline

In 1993 Wallbank and Holmes initiated a series of experiments designed to make critical tests of the theory of free-free transitions, i.e. laser-assisted scattering processes in which the atom remains in its ground state while the electron exchanges photon quanta with the field [25, 26, 27]. Large discrepancies between the conventional theory of these processes, the Kroll-Watson theory [28], and experimental data emerged. These discrepancies have stimulated a lot of theoretical interest in free-free transitions (see, for example, the review by Ehlötzky *et al.* [29]). One of the main goals of the present thesis is to undertake an analysis of the theory of laser-assisted electron scattering and to compare different models. This is done in order to study the virtues and shortcomings of different approximation schemes and to understand the differences between theoretical predictions and experimental data.

Chapter 2 gives an introduction to laser-assisted scattering and a survey of the current experimental and theoretical situation. Chapter 3 gives a short account of the classical theory of laser-assisted scattering, while chapter 4 is concerned with a discussion of the quantum theory of laser-assisted scattering. Non-resonant as well as resonant scattering is discussed. Calculations and conclusions are presented in chapter 5.

Two-colour experiments and theory have played a prominent role in laser-atom interactions in recent years. In theory, amplitudes for the considered process are usually added and subsequently squared. This, of course, leads to signals which are dependent on the relative phase between the two colours. In two-colour multiphoton ionization experiments, for example, such a dependence has been reported [30, 31]. In chapter 6, we study in detail the dependence of the coherences on the preparation of the atom that probes the coherences in the two incoming laser beams in a two-colour electron-atom scattering experiment.

Chapters 7-9 are devoted to a discussion of ionization of H_2^+ in the multiphoton regime. After an introduction to the subject in chapter 7, the Floquet-Sturmian method of calculation is outlined in chapter 8. Results of calculations are presented in chapter 9. In particular, we study the variation of the

quasienergy as a function of internuclear distance. We find a new rich structure of multiphoton resonances. The mechanisms for enhanced ionization in the multiphoton regime are contrasted with those that apply in the tunnelling regime. A detailed comparison between Floquet and wavepacket calculations is also presented.

Chapter 10 points towards directions of future work.

Appendix A presents technical details in the derivation of the weak-field soft-photon transition amplitude of laser-assisted electron scattering.

Appendix B outlines how to find complex eigenvalues of the Floquet eigenvalue problem iteratively.

Appendix C sketches how to obtain complex eigenvalues by the complex-scaling method and by the use of the real Hamiltonian with complex-basis-functions.

Finally, in appendix D, a thesis resumé for the university yearbook is included.

Chapter II

Introduction to laser-assisted electron scattering

Laser-assisted elastic electron-atom scattering is a process of the type

$$e_{\mathbf{q}_i} + A_i \rightarrow e_{\mathbf{q}_f} + l\hbar\omega + A_i, \quad (2.1)$$

where the atom A remains in its ground state during the collision while the electron exchanges l quanta with the photon field ($l < 0$ for absorption and $l > 0$ for emission) to change momentum from \mathbf{q}_i to $\mathbf{q}_f = \mathbf{q}_i + \mathbf{Q}$. This kind of process, which is referred to as a free-free transition, has been studied extensively over the last two decades. For recent reviews, see [32, 29]. Also the textbooks of Mittleman [33, 34] and Faisal [35] discuss laser-assisted electron scattering.

2.1 The Kroll-Watson theory

The theory of free-free transitions was developed by Kroll and Watson [28] in the so-called soft-photon (SP) approximation, where terms to first order in the photon frequency ω are retained. The SP approximation presupposes that ω is small compared to the asymptotic kinetic energy, \mathcal{E} , of the scattered electron ($\hbar\omega \ll \mathcal{E}$). Considering a linearly polarized laser field with polarization vector $\boldsymbol{\epsilon}$ and vector potential amplitude A_0 , the Kroll-Watson (KW) approximation for the differential cross-section for free-free scattering may be expressed as

$$\frac{d\sigma}{d\Omega}(\mathbf{Q}, l) = \frac{q_f(l)}{q_i} J_l^2\left(\frac{A_0}{\omega} |\boldsymbol{\epsilon}\mathbf{Q}|\right) \frac{d\sigma^{\text{el}}}{d\Omega}(\mathbf{q}_f(l) + \boldsymbol{\gamma}, \mathbf{q}_i + \boldsymbol{\gamma}). \quad (2.2)$$

The last factor in this expression represents the elastic field-free differential scattering cross-section evaluated at suitably displaced momenta. The first factor on the rhs arises from the usual probability current analysis. Finally, $J_l(\frac{A_0}{\omega} |\boldsymbol{\epsilon}\mathbf{Q}|)$ is a Bessel function of first kind. [Here and throughout atomic units are used unless otherwise indicated. A factor $c/8\pi$ is absorbed in the definition of the atomic unit of intensity, $I_0 = 3.51 \times 10^{16} \text{ W cm}^{-2}$.] In the effective momenta $\mathbf{q}_j(l) + \boldsymbol{\gamma}$ ($j = i, f$) of equation (2.2), the momentum displacement vector is

given by

$$\gamma = \frac{l\omega\epsilon}{\epsilon\mathbf{Q}}. \quad (2.3)$$

In their derivation, Kroll and Watson [28] used the stationary phase approximation. As we shall see, the regions of stationary phase are determined by the classical energy transferred to the electron during the scattering. Not surprisingly, therefore, $d\sigma^{\text{el}}(\mathbf{q}_f(l) + \gamma, \mathbf{q}_i(l) + \gamma)$ is on the energy shell.

The factor $J_l^2(\frac{A_0}{\omega}|\epsilon\mathbf{Q}|)$ in (2.2) originates from the Volkov representation of initial and final electron states in the presence of the laser field [7] (see also [33, 35]). Since $J_l(x) \propto x^l$ for small arguments, it is clear that the KW approximation predicts a small cross-section for laser-assisted processes when the argument $A_0|\epsilon\mathbf{Q}|/\omega$ of the Bessel function is small. This may of course happen for sufficiently weak laser fields, but also in situations where \mathbf{Q} is parallel to the propagation direction of the laser beam. Notice, however, that the momentum displacement vector, γ , *diverges* in this latter situation. We refer to this experimental arrangement as the *critical* geometry. Due to the divergence of γ , it is not clear if the KW approximation remains valid as the critical geometry is approached. On the other hand, *if* the scattering conditions are such that γ is small it may be legitimate to consider the limit of the KW approximation where the l -dependent momentum shift and the corresponding energy transfer are ignored. We shall refer to this approach as the zero-order soft-photon (ZOSP) approximation. The ZOSP approximation is often used in practice when the relative laser-assisted signal

$$R = \frac{d\sigma(\mathbf{Q}, l)}{d\sigma^{\text{el}}(\mathbf{Q})} \quad (2.4)$$

is determined experimentally since the field-free cross-section then is common for all l -values and may be eliminated to obtain the simple result

$$R = J_l^2\left(\frac{A_0}{\omega}|\epsilon\mathbf{Q}|\right). \quad (2.5)$$

Notice that equation (2.5) holds whenever the Born approximation accurately describes the elastic process. In this case, the elastic cross-section depends upon the electron momentum transfer only.

It is convenient to classify laser-assisted scattering processes depending on whether they are classically allowed or forbidden [28] (see also [36, 37, 38]). Critical geometries may be defined, for arbitrary polarizations ϵ , as arrangements where the total photon energy exchanged with the scattered electron exceeds the classical limit of the energy transfer in an instantaneous collision [28] (see also chapter 3)

$$\Delta\mathcal{E}_{\text{max}}^{\text{cl}} = A_0|\epsilon\mathbf{Q}|. \quad (2.6)$$

Measuring energy transfer in units of laser photons, the maximum number of photons which can be exchanged classically during the interaction with the scatterer is given by the integer part of

$$L = A_0|\epsilon\mathbf{Q}|/\omega, \quad (2.7)$$

a quantity we may refer to as the classical cut-off in the number of exchanged photons. Note that the argument of the Bessel functions of equations (2.2) and (2.5) represents the cut-off in the number of photons that can be exchanged classically and that, consistently, $J_l(L)$ in general becomes small when $|l|$ exceeds L .

2.2 Current experimental and theoretical work

The first experiments on laser-assisted electron-atom scattering were due to Weingartshofer *et al.* [3, 39, 4], who studied free-free transitions in the classically allowed region ($|l| \leq L$). A direct comparison showed that equation (2.5) did account qualitatively for the experimental data. Quantitative agreement was obtained by suitably modelling the experimental conditions such as temporal and spatial variations in the laser beam and by using a multi-mode description [40]. [Aspects of photon statistics (mode model) had been considered by Zoller [41], who found that the cross-section for free-free scattering in a chaotic light model is $l!$ times larger than the corresponding cross-section in a classical laser field.]

To expose the theory to a more critical test, Wallbank and Holmes [25, 26, 27] studied free-free transitions under critical conditions where the angle between the field polarization plane and the electron momentum transfer vector is very close to 90° . The corresponding argument of the Bessel function in equations (2.2) and (2.5) is then much smaller than unity. Accordingly, the experiments are performed under conditions where exchange of photons during the scattering is classically forbidden ($|l| > L$). On the basis of the KW approximation, one might therefore expect a very small cross-section for photon-assisted scattering. This expectation is, however, not supported by experiments. Wallbank and Holmes consider various possibilities to explain the discrepancy between their experiments and the KW theory. One suggestion is that the electron-atom polarization potential ($\sim 1/r^4$) and especially the field-induced dipole potential ($\sim 1/r^2$) might be responsible. It has been shown, however, that the correction arising from the polarization of the target atom by the laser field is far below what is needed to explain the experimental observations [36, 42, 43].

The experiments by Wallbank and Holmes have stimulated theoretical work involving distorted-wave [44], Floquet close-coupling [45], R -matrix Floquet [46] and Floquet Lippmann-Schwinger [47] methods as well as evaluation of the impulse approximation [48]. A clear explanation of the experimental data has not yet emerged. The Floquet close-coupling calculations have indicated a significant departure from the KW formula (2.2), but the full Floquet close-coupling analysis of laser-assisted scattering is technically complicated and difficult to extend to the intensities used in experiments [45]. The implication by Jaroń and Kamiński [48], that the laser-assisted process in the classically forbidden region is strongly affected by off-energy-shell effects due to long-ranged polarization forces is, e.g., at variance with the results of Kylstra and Joachain [47] who conclude that a satisfactory explanation of the results has yet to be put forth.

The pronounced departure of the KW theory under critical conditions is not restricted to cases with long-range potentials, but persists in case of a short-range Yukawa-type potential, where off-shell effects are marginal [49, 50, 51], as well as in the case of laser-assisted scattering in the zero-range potential discussed in chapters 4 and 5, in which off-shell effects are absolutely absent.

The significance of exchange scattering was studied by Trombetta [52]. It was found that the exchange amplitude in the first Born approximation may be factorized according to ordinary free-free potential scattering provided the ponderomotive quiver energy (see equation (3.3) below) is much less than the energy of the incoming electron. Exchange scattering may then be understood to be included in the field-free scattering cross-section in (2.2). Although the validity of the first Born approximation may be questioned for the experimental conditions of Wallbank and Holmes, the important condition that the quiver energy is much less than the energy of the incoming electron is fulfilled and we expect the conclusion of Trombetta to remain approximately valid. This is supported by two-electron R -matrix Floquet calculations [46]

2.3 Questions addressed in this thesis

We have previously analysed the full quantum theory of potential scattering in a linearly polarized light field in a consistent weak-field expansion [44, 53]. Considering the first order expansion in the electromagnetic vector potential and using the soft-photon approximation to eliminate off-energy-shell effects in the intermediate propagation, the weak-field soft-photon (WFSP) approximation emerges. The WFSP T -matrix is derived in chapter 4 for general laser polarization, using time-dependent S -matrix as well as time-independent T -matrix theory. The WFSP approximation is applicable independently of geometrical constraints. The essential improvement is to avoid the additional expansion of the KW theory in the momentum displacement vector, γ , which, according to equation (2.3) may diverge in special experimental geometries and indeed is prohibitively large in the experiments of Wallbank and Holmes [26, 27]. As limiting cases the WFSP approximation includes the ZOSP approximation and, for linearly polarized light, also the KW approximation. To obtain a generalization of the KW approximation for arbitrary laser polarizations, we consider the impulse approximation (IA) and identify two regions of stationary phase to evaluate the corresponding T -matrix element in a peaking approximation [38]. The resulting peaked impulse approximation (PIA) reduces to the KW formula for linear polarization.

The zero-range potential scattering model [54] has been considered in detail in connection with multiphoton ionization [55, 56] and high-harmonic generation [57, 58, 59] and provides a fine description of observed phenomena such as the plateau and the cut-off in high-harmonic generation spectra. In the special case of a circularly polarized field, it offers an exact solution [55] for the laser-assisted scattering problem and thus provides a unique testing ground for approximations introduced in the various theories. Such tests are presented in

chapter 5. In comparison with exact model results we find that the IA very accurately describes one- and multiphoton processes in allowed and classically forbidden arrangements. For more realistic collision systems the IA is very hard to evaluate [48]. Theories like the WFSP approximation, the PIA or the zero order approximation therefore become of much interest. Our comparison with the exact results shows that the WFSP approximation is the only one of these models which is valid in the classically forbidden region. In the classically allowed region the PIA is shown to be superior: it depends on the parameters of the laser field in a less restrictive way than the WFSP approximation, and it accurately describes the cross section over an extended range of laser frequencies and intensities.

The Kroll-Watson theory is usually referred to as a soft-photon theory without specification of relevant auxiliary conditions: is it really meant to be a low-frequency approximation assuming constant field amplitude, F_0 , i.e. constant intensity, constant vector potential amplitude, $A_0 = F_0/\omega$, constant quiver radius, $\alpha_0 \propto F_0/\omega^2$, or what? The problem is, of course, that there are several steps in the derivation of the theory. Considering, for example, that the KW approximation and the PIA are derived from the impulse approximation [48], it is clear that the variation of the vector potential during the collision time, t_c , is assumed to be small compared to the incident momentum of the electron, i.e. $\omega A_0 t_c \ll q_i$ or $F_0 \ll \mathcal{E}/a$, where a is a measure of the effective range of the potential. It is, on the other hand, not easy to justify on these grounds that the smallness of F_0 should be a sufficient condition for the validity of the KW theory. The alternative derivation of the KW approximation in our previous work [44, 38] suggests that the KW approximation should be valid, provided that A_0 as well as ωA_0 are sufficiently small. These questions are further examined in chapters 4 and 5 and a firm assessment of the validity criteria of the PIA and the WFSP theory is given.

Chapter 5 also presents evaluations of non-resonant laser-assisted electron-argon for one-photon exchange. The calculations show that the WFSP theory is able to reproduce the pronounced structures observed in the experimental results of Wallbank and Holmes [26, 27]. The overall comparison is, however, rather poor and it is indicated that the departure between the strict theory and the experiments might be associated with uncertainties in the experimental definition of the scattering geometry.

The development in section 4.1 and the calculations presented in sections 5.1 and 5.2 below are restricted to situations in which the corresponding field-free cross-section varies slowly with the electron and photon energy. Cases where the atomic potential supports a resonance are thus excluded. Resonances are, however, particularly interesting in connection with free-free transitions as pointed out by Jung and Taylor [60]. These authors considered the zero-order soft-photon (ZOSP) approximation and realized that resonances should appear as pure Breit-Wigner peaks if experiments are performed in the critical geometry. This would allow a determination of the resonance energy and width with high accuracy. The Jung and Taylor conjecture has been studied experimentally

[61, 62, 63] but, the non-resonant background is generally significantly larger than predicted by theory. In section 4.3 the WFSP approximation is generalized to account for electron-atom scattering resonances. The application of the theory is illustrated in section 5.3 by the case of free-free transitions in electron-argon scattering near the 2P_J resonances at 11.10 eV and 11.27 eV in the radiation field of a CO₂ laser as well as in the field of a tunable laser, which may scan the energy splitting between the considered resonances. The WFSP approximation shows that the background amplitude may be orders of magnitude larger than in previous theories and that it may compete with the resonance part to produce characteristic Fano-type resonance signals [64] in situations where the ZOSP approximation predicts pure Lorentzians. The background is suppressed at lower laser intensities, leaving Lorentzian line-shapes, not only at the position of the corresponding field-free resonances, but also at positions separated from these by an integral number of laser photons. In case of a CO₂ laser, the two series of laser-assisted argon resonances are well separated, but considering tunable radiation fields, it is possible in principle to merge the two series to investigate the quantum mechanics of overlapping resonances under conditions where interference effects are possible [65].

We begin the more detailed discussion of laser-assisted scattering by summarizing some useful classical considerations in chapter 3.

Chapter III

Classical theory of laser-assisted electron scattering

To extract the basic physics of laser-assisted electron scattering, it is helpful to make classical calculations along the lines of Kroll and Watson [28]. In general the physical character of the process of scattering may be divided into two categories: firstly, classically allowed scattering in which the number of photons exchanged, $|l|$, is smaller than the classical cut-off ($|l| \leq L$) and secondly, classically forbidden in which the electron exchanges more photons with the field than classically allowed, $|l| > L$. Critical geometries are scattering arrangements in which photon-assisted scattering is classically forbidden.

In this chapter we first discuss the classical concepts of quiver amplitude and ponderomotive potential. Secondly, we discuss the classical theory of laser-assisted electron scattering. The relation to quantum and semi-classical calculations is discussed in the next chapter.

3.1 Quiver amplitude, ponderomotive potential and intensity

Classically, the electromagnetic vector potential, $\mathbf{A}(\mathbf{r}, t)$, for an elliptically polarized single mode laser of angular frequency ω propagating in the z -direction can be expressed as

$$\mathbf{A}(\mathbf{r}, t) = \frac{1}{2}A_0 (\boldsymbol{\epsilon} \exp[i(\mathbf{k}\mathbf{r} - \omega t)] + \boldsymbol{\epsilon}^* \exp[-i(\mathbf{k}\mathbf{r} - \omega t)]) \quad (3.1)$$

with the polarization vector

$$\boldsymbol{\epsilon} = \mathbf{e}_x \cos(\xi/2) + i\mathbf{e}_y \sin(\xi/2). \quad (3.2)$$

The ellipticity parameter, ξ , describes all degrees of elliptical polarization when varied in the range $\pi/2 \leq \xi \leq \pi/2$ ($\xi = 0$ and $\xi = \pi/2$ correspond to linear and circular polarization, respectively). In actual calculations, classical as well as quantum, it is simplifying to introduce the dipole approximation. The dipole approximation is usually justified by noting that the typical range of the atomic potential is a few atomic units, implying that $\mathbf{k}\mathbf{r} \ll 1$ in the spatial region of

interest. The electric field, $\mathbf{F}(t)$, is obtained by $\mathbf{F}(t) = -\partial_t \mathbf{A}(t)$. We note the relation $F_0 = \omega A_0$ between the amplitude of the electric field, F_0 , and the vector potential amplitude A_0 . Solving the classical equation of motion of an electron moving in the field $\mathbf{F}(t)$ gives the velocity as well as the position of the electron at any instant of time. The ponderomotive potential, i.e. the time-averaged kinetic energy of the electron in the transverse oscillatory motion of velocity v_{osc} , is then readily calculated:

$$U_p = \overline{v_{\text{osc}}^2}/2 = \frac{1}{4} A_0^2 = \frac{1}{4} \frac{F_0^2}{\omega^2}. \quad (3.3)$$

The bar denotes the time-average over one cycle of the field, $T = 2\pi/\omega$. We note that the ponderomotive energy is independent of the polarization of the field. In the weak-field limit, U_p can be neglected. In our discussion of multiphoton ionization of H_2^+ in chapters 7-9, it is important to account for U_p .

The maximum excursion amplitude along the principal axis in the oscillatory elliptical motion of the electron in the electromagnetic field is denoted the quiver radius, α_0 , and

$$\alpha_0 = \cos(\xi/2) \frac{A_0}{\omega}. \quad (3.4)$$

In the case of linearly and circularly polarized light, α_0 attains its maximum and minimum values, respectively. The quantity A_0/ω , and therefore the quiver radius, determines, together with the projection of the electron momentum transfer on the polarization vector, the coupling between the electron and the field in laser-assisted electron-atom scattering¹.

Finally, we note the relation to the intensity

$$I = \omega^2 A_0^2 = F_0^2, \quad (3.5)$$

which is obtained by considering the time-averaged Poynting's vector [69]. The energy flow is in the direction of propagation of the laser. Notice that the quiver radius is left unchanged going from linear to circular polarization if the intensity is doubled.

3.2 Classical theory of laser-assisted electron scattering

In the soft-photon limit ($\omega \ll \mathcal{E}$), the collision time is extremely short compared with $1/\omega$ and it is a good approximation to consider the classical collision to take place instantaneously. The instantaneous momentum of the electron is [28]

$$\mathbf{p}(t) = \mathbf{q}_j + \mathbf{A}(t). \quad (3.6)$$

¹Free-free transitions in intense high-frequency laser-fields as well as the phenomena of stabilization of intense field ionization are also crucially dependent on the magnitude of the quiver radius [66, 67]. In wavepacket calculations of ionization rates, the grid boundaries must be at least 2–3 times α_0 from the nucleus to give reliable results [68]. This imposes severe demands on computer resources and also gives rise to upper limits on the wavelengths and intensities that can be considered with wavepacket methods.

Here \mathbf{q}_j ($j = i, f$) are observable asymptotic linear momenta of the electron corresponding to the time-averaged value of $\mathbf{p}(t)$. The scattering takes place elastically from incident \mathbf{p}_i to final \mathbf{p}_f . The electron momentum transfer vector is independent of the field due to the absence of phase evolution in the instantaneous collision

$$\mathbf{Q} = \mathbf{p}_f - \mathbf{p}_i = \mathbf{q}_f - \mathbf{q}_i. \quad (3.7)$$

Since $p_f^2 = p_i^2$, the energy exchanged with the field is:

$$q_i^2/2 - q_f^2/2 = \mathbf{Q}\mathbf{A}(t) = A_0|\epsilon\mathbf{Q}|\cos(\tau - \omega t), \quad (3.8)$$

where we have introduced the phase

$$\tau = \text{Arg}(\epsilon\mathbf{Q}) = \arctan \frac{Q_y}{Q_x} \tan \xi/2. \quad (3.9)$$

The energy in (3.8) determines the phase of the field at the instant of collision and therefore the instantaneous momenta $\mathbf{p}_j(t)$. In particular, we see that the maximum energy exchanged with the field is given by (3.8) when the cosine is ± 1 . The maximum energy transfer is then given by (2.6). Assigning the value $L\omega$ to this energy, we rediscover the classical cut-off in the number of exchanged photons of equation (2.7). In the quantum treatment, we will encounter situations where equation (3.8) has no solutions on the real time axis. These situations correspond to classically forbidden laser-assisted scattering.

Following the derivation as presented by Kroll and Watson [28], but generalizing to arbitrary polarization, we can derive the classical expression for the differential scattering cross section in the presence of elliptically polarized light

$$\begin{aligned} \frac{d\sigma}{d\Omega dq^2} &= \frac{q_f}{q_i} \frac{1}{2\pi\omega L |\sin(\tau - \omega t_{1,2})|} \\ &\times \frac{1}{2} \left(\frac{d\sigma^{\text{el}}}{d\Omega}(\mathbf{p}_f(t_1), \mathbf{p}_i(t_1)) + \frac{d\sigma^{\text{el}}}{d\Omega}(\mathbf{p}_f(t_2), \mathbf{p}_i(t_2)) \right). \end{aligned} \quad (3.10)$$

Here the phase at the instant of scattering, $\tau - \omega t_{1,2}$, is determined by equation (3.8), and $t_{1,2}$ are the two instants of time solving this equation in the interval $[0; 2\pi/\omega]$. The cross sections on the rhs are, of course, purely classical. Notice that $\mathbf{p}_j(t_1) \neq \mathbf{p}_j(t_2)$ ($j = i, f$) except for linear polarization where the momenta are equal (this point is discussed in more detail in chapter 4). To relate to quantum mechanics, it is natural to introduce the 'bin' of energy, $dq^2 = 2\omega$, to obtain

$$\begin{aligned} \frac{d\sigma}{d\Omega} &= \frac{q_f(l)}{q_i} \frac{1}{\pi L |\sin(\tau - \omega t_{1,2})|} \\ &\times \frac{1}{2} \left(\frac{d\sigma^{\text{el}}}{d\Omega}(\mathbf{p}_f(t_1), \mathbf{p}_i(t_1)) + \frac{d\sigma^{\text{el}}}{d\Omega}(\mathbf{p}_f(t_2), \mathbf{p}_i(t_2)) \right). \end{aligned} \quad (3.11)$$

In the case of linearly polarized light, (3.10) and (3.11) simplify to results given in [28]. Referring to the $|\sin(\tau - \omega t_{1,2})|^{-1}$ factor in (3.10) and (3.11), it is seen

that the classical scattering cross-section possesses singularities when the classical energy transferred to the electron is at maximum. This kind of singularity is similar to the *rainbow singularity* in the classical approximation of ion-atom and atom-atom collisions [70]. In the vicinity of these singularities, a semi-classical or a full quantum mechanical rather than a classical theory is needed and this will be discussed in the next chapter.

Chapter IV

Theory of laser-assisted electron scattering

The impulse approximation is considered as a point of departure for a consistent derivation of the weak-field soft-photon approximation as well as for a generalization of the Kroll-Watson theory for electron-atom scattering in arbitrarily polarized laser light. General validity conditions and corresponding order parameters are identified with careful distinction between allowed and classically forbidden regions. We also discuss the full quantal approach. The emerging theory is the weak-field soft-photon approximation. The scattering by the zero-range potential is briefly discussed and finally the theory is extended to account for resonances and scattering in two-colour fields.

4.1 Non-resonant laser-assisted electron scattering

The laser field is described by the classical vector potential

$$\mathbf{A}(t) = \frac{1}{2} A_0 (\boldsymbol{\epsilon} e^{-i\omega t} + \boldsymbol{\epsilon}^* e^{i\omega t}) \quad (4.1)$$

with the polarization vector given by equation (3.2). Considering that the classical quiver radius of equation (3.4) is typically a few atomic units and that the range of the potential is of similar magnitude, it is a very accurate approximation to apply the dipole approximation, i.e. to ignore the spatial variation of the field. A similarly simple consideration shows that it is a very good approximation to ignore the time variation of the actual laser pulse since the collision time with the potential is much smaller than the pulse time of the relevant laser system and actually much smaller than $1/\omega$ in typical experiments.

The impulse approximation (IA) T -matrix for non-resonant l -photon free-free transitions is given by [28] (see, e.g., [48, 38] for more recent references)

$$\mathcal{T}_l^{\text{IA}}(\mathbf{Q}) = \frac{\omega}{2\pi} \int_0^{2\pi/\omega} dt \exp[-i(l\omega t + L \sin(\tau - \omega t))] T_{\mathbf{p}_i(t)}(\mathbf{Q}), \quad (4.2)$$

where $T_{\mathbf{p}_i(t)}(\mathbf{Q})$ is the elastic off-shell transition amplitude in which the laser-electron interaction is described by the instantaneous electron momentum

$$\mathbf{p}_j(t) = \mathbf{q}_j + \mathbf{A}(t), \quad (j = i, f), \quad (4.3)$$

and where τ is the phase given by equation (3.9). The IA is well-defined for allowed as well as classically forbidden processes.

4.1.1 Classically allowed laser-assisted scattering ($|l| \leq L$)

We introduce the variable $z = \omega t - \tau$ and use the 2π -periodicity to rewrite equation (4.2) as

$$\mathcal{T}_l^{\text{IA}}(\mathbf{Q}) = e^{-il\tau} \frac{1}{2\pi} \int_{-\pi}^{\pi} dz \exp[-i(lz - L \sin(z))] T_{\mathbf{p}_i((z+\tau)/\omega)}(\mathbf{Q}). \quad (4.4)$$

In the following, $e^{-il\tau}$ will be ignored as the cross-section is independent of this phase factor. In the limit, $L \gg 1$, the exponential factor will be rapidly oscillating as z varies over the integration interval and the principal contribution will come from z -values close to the regions of stationary phase

$$L \cos(z) = l. \quad (4.5)$$

Equation (4.5) has one solution, z_+ , for $0 \leq z \leq \pi$ and another, z_- , for $-\pi \leq z \leq 0$. The corresponding values of time are t_{\pm} and the pertaining vector potentials read

$$\boldsymbol{\gamma}_{\pm} \equiv \mathbf{A}(t_{\pm}) = A_0 (\mathbf{d}_1 \cos z_{\pm} + \mathbf{d}_2 \sin z_{\pm}) = A_0 \left(\mathbf{d}_1 \frac{l}{L} \pm \mathbf{d}_2 \sqrt{1 - \left(\frac{l}{L}\right)^2} \right), \quad (4.6)$$

with \mathbf{d}_1 and \mathbf{d}_2 defined as

$$\mathbf{d} = \mathbf{d}_1 + i\mathbf{d}_2 = \boldsymbol{\epsilon} e^{-i\tau}. \quad (4.7)$$

Inserting the fields from equation (4.6) into (3.6) leads to the shifted momenta

$$\mathbf{p}_j(t_{\pm}) = \mathbf{q}_j + \boldsymbol{\gamma}_{\pm}. \quad (4.8)$$

Identifying the classical energy transfer with $l\omega$ the condition in (4.5) may be re-derived in a classical treatment assuming instantaneous elastic scattering [28]. Correspondingly, $\boldsymbol{\gamma}_{\pm}$ are exactly the displacements needed to keep the T -matrix on the energy shell.

Note that the first term in the momentum shift in equation (4.6) is independent of A_0 and vanishes in the soft-photon limit while the second term is proportional to A_0 and independent of ω in the few photon exchange soft-photon ($L \gg 1$) limit. We also note that the displacement vectors $\boldsymbol{\gamma}_{\pm}$ become complex

in the classically forbidden region ($|l| > L$) as equation (4.5) is then solved by purely imaginary z -values.

In the classically allowed region, $|l| \leq L$, the laser-assisted T -matrix (4.2) may be evaluated on the energy shell at the real-valued displaced momenta of equation (4.8). We now assume that $T_{\mathbf{p}_i}(\mathbf{Q})$ is slowly varying as a function of \mathbf{p}_i . This condition is generally expected to be valid for off-resonance scattering by short-ranged potentials¹. We may therefore split the integration interval into two and replace the T -matrix element by its value at the corresponding points of stationary phase. We are thus lead to the peaked impulse approximation (PIA)

$$T_l^{\text{PIA}}(\mathbf{Q}) = \frac{1}{2\pi} \left(T_+(\mathbf{Q}) \int_0^\pi dz e^{-i(lz - L \sin(z))} + T_-(\mathbf{Q}) \int_{-\pi}^0 dz e^{-i(lz - L \sin(z))} \right), \quad (4.9)$$

where $T_\pm(\mathbf{Q})$ is shorthand for $T_{\mathbf{p}_i(t_\pm)}(\mathbf{Q})$. The remaining integrals may be recognized as linear combinations of Anger, $\mathcal{J}_l(L)$, and Weber, $\mathcal{E}_l(L)$, functions.

$$T_l^{\text{PIA}}(\mathbf{Q}) = \frac{1}{2} (\mathcal{J}_l(L)[T_+(\mathbf{Q}) + T_-(\mathbf{Q})] - i\mathcal{E}_l(L)[T_+(\mathbf{Q}) - T_-(\mathbf{Q})]). \quad (4.10)$$

For integer l the Anger function equals the Bessel function, $J_l(L)$. The PIA represents a generalization of the KW formula to arbitrary polarizations. In the case of linearly polarized light, the phase factor $e^{-i\tau}$ is real such that $\gamma_+ = \gamma_- = \gamma$ where γ is the KW displacement

$$\gamma = (l/L)A_0\mathbf{d}_1. \quad (4.11)$$

Consequently we find $T_+(\mathbf{Q}) = T_-(\mathbf{Q}) = T_{\mathbf{q}_i+\gamma}$. The second term in equation (4.10) accordingly vanishes for linearly polarized light while the first term simplifies to $J_l(L)T_{\mathbf{q}_i+\gamma}$ leading to the standard KW expression (2.2). For general polarization, however, $\gamma_+ \neq \gamma_-$ such that the Weber term makes an essential contribution. This excludes a standard KW factorization in accordance with the work of Kelsey and Rosenberg [72].

An analytical continuation of the PIA into the classically forbidden region ($|l| > L$) is obtained by solving equation (4.5) for purely imaginary z , corresponding to complex instants of time. The corresponding vector potential is then complex itself and its amplitude appears virtually to be larger than the classical amplitude, A_0 . Similarly, the displacement given by equation (4.6) become complex vectors, too. The PIA in the classically forbidden regime can be derived directly from equation (4.4) by deformation of the contour of integration into the complex plane such that the two saddle points appear along the contour. As in (4.9) T -matrices may be peaked at saddle points and the remaining integrals are evaluated by deformation back to the real axis. When formally

¹A recent calculation [48] has indicated that the on-shell approximation may be invalid for laser-assisted collisions in long-ranged polarization potentials, not to mention the peculiarities manifested, for example, in the theory of electron capture in ion-atom collisions [71].

extrapolating into the classically forbidden region the displacement vectors often become so large that the result is at variance with experiments as well as with alternative theories better founded in the classically forbidden region [44]. Figure 5.1 illustrates this point.

4.1.2 The semi-classical limit, $L \gg 1$

The semi-classical limit is characterized by $L \gg 1$. Kroll and Watson [28] obtained a semi-classical expression for the laser-assisted cross-section in linearly polarized fields. This was done using asymptotic expressions for the Bessel function. An equally transparent derivation is obtained from standard semi-classical considerations as applied, for example, in the semi-classical scattering theory of ion-atom collisions: when the two regions of stationary phase are well separated, corresponding to $|l| \ll L$, we may consider the two regions separately and coherently add the individual T -matrices to obtain the cross-section (see, e.g., [70]). This method applies for general polarization and simplifies in the case of linear polarization to the result presented in [28] (see also equations (3.10) and (3.11)). For elliptical polarization and well-separated regions of stationary phase, the result of the semi-classical T -matrix is

$$\begin{aligned} \mathcal{T}_l(\mathbf{Q}) &= \frac{1}{\sqrt{2\pi L |\sin z_{\pm}|}} (T_+(\mathbf{Q}) \exp[-i(lz_+ - L \sin z_+ + \pi/4)] \\ &+ T_-(\mathbf{Q}) \exp[-i(lz_- - L \sin z_- - \pi/4)]), \end{aligned} \quad (4.12)$$

which for non-linear polarization gives rise to an interference term proportional to $\cos(2(lz_+ - L \sin z_+)) \text{Re}(T_+(\mathbf{Q})T_-(\mathbf{Q}))$. The cos-factor indicates large fluctuations as the photon number changes by unity. For a mean behavior we take cos equal to zero, and hence the interference term cancels out in the classical limit as it should. In this way we recover the classical cross-section (3.11) with the important exception that the field-free cross-sections on the rhs are now fully quantum mechanical.

In the transition region, $|l| \sim L$, the two stationary phase regions coalesce and the scattering amplitudes cannot be treated separately. Instead, the phase of the exponential function of equation (4.2) is expanded to third order around the region of stationary phase. Evaluating the potential scattering T -matrix by the peaking approximation, we are left with the Airy integral. The result in the semi-classical transition region ($|l| \sim L \gg 1$) reads

$$\mathcal{T}_l^{\text{IA}}(\mathbf{Q}) \sim \left(\frac{2}{L}\right)^{1/3} \text{Ai}\left(2^{1/3} \frac{|l| - L}{L^{1/3}}\right) T_{\mathbf{q}_i + \gamma}(\mathbf{Q}). \quad (4.13)$$

Note that the T -matrix on the rhs depends only on the KW displacement vector of equation (4.11). This is due to the fact that the \mathbf{d}_2 components of the general displacement vectors can be neglected in the transition region. The expression in (4.13) extrapolates in an exponentially decreasing way into the classically forbidden region and merges with the KW term in the classically allowed region

in the sense that (4.13) may also be obtained by an asymptotic expansion of the Bessel function in equation (4.10) for $|l| \sim L \gg 1$. Equations (4.12) and (4.13) represent the semi-classical theory alluded to in the end of chapter 3.

4.1.3 Classically forbidden laser-assisted scattering ($|l| > L$)

For $|l| > L$ we enter the classically forbidden region, and the stationary phase condition (4.5) can no longer be fulfilled for real values of z . As discussed above and in chapter 5, the analytical continuation of the PIA to complex displacement vectors does not give a good estimate of the laser-assisted cross-section in the classically forbidden regime, except for sufficiently weak fields in the transition region, $|l| \simeq L$. We might instead try to evaluate the full expression in (4.2). This is easily done if a closed analytical expression of the off-shell scattering amplitude is available. The zero-range potential considered below is one such example [54]. The evaluation of the IA is also possible for more realistic potentials using modern super computers calculating the off-shell scattering amplitude numerically [48]. Alternatively, a Taylor expansion of the $T_{\mathbf{p}_i(t)}(\mathbf{Q})$ about $\mathbf{p}_i(t) = \mathbf{q}_i$ can be introduced. In the weak-field approximation, terms are kept to the first order in the vector potential $\mathbf{A}(t)$:

$$T_{\mathbf{p}_i(t)}(\mathbf{Q}) \simeq T_{\mathbf{q}_i}(\mathbf{Q}) + \mathbf{A}(t) \nabla_{\mathbf{q}_i} T_{\mathbf{q}_i}(\mathbf{Q}). \quad (4.14)$$

This approximation presupposes that the interaction of the electron with the laser field is sufficiently weak to justify the use of perturbation theory in the intermediate stages of the collision process, but allows an exact treatment of the electron interaction with the atomic potential. The effective order parameter in the expansion is A_0 . Equation (4.14) is thus a first order expansion. The soft-photon approximation additionally presupposes that $T_{\mathbf{p}_i}(\mathbf{Q})$ is a slowly varying function of \mathbf{p}_i in the near-shell limit. Inserting (4.14) into equation (4.2) allows an evaluation of the time-integrals using the generating function of the Bessel function. We then obtain the weak-field soft-photon (WFSP) transition amplitude (again we leave out an overall phase factor)

$$\mathcal{T}_l^{\text{WFSP}}(\mathbf{Q}) = J_l(L) T_{\mathbf{q}_i}(\mathbf{Q}) + \frac{A_0}{2} [\mathbf{d} J_{l+1}(L) + \mathbf{d}^* J_{l-1}(L)] \nabla_{\mathbf{q}_i} T_{\mathbf{q}_i}(\mathbf{Q}). \quad (4.15)$$

An alternative derivation based on the quantized field approach, discussed in detail by Kelsey and Rosenberg [72], is presented in section 4.1.4. The derivation in section 4.1.4 begins with the exact distorted-wave expression of the T -matrix. An expansion to first order in A_0 followed by an expansion to first order in ω gives the result in (4.15). Note, however, that the equivalence between the impulse approximation and the distorted wave theory only holds to first order; correction terms to the WFSP amplitude can only be consistently derived by inclusion of higher order terms in the distorted wave theory expansion.

We may rewrite the WFSP T -matrix as

$$\mathcal{T}_l^{\text{WFSP}}(\mathbf{Q}) = J_l(L) [1 + \gamma \nabla_{\mathbf{q}_i}] T_{\mathbf{q}_i}(\mathbf{Q}) - i A_0 J'_l(L) \mathbf{d}_2 \nabla_{\mathbf{q}_i} T_{\mathbf{q}_i}(\mathbf{Q}), \quad (4.16)$$

by resolving \mathbf{d} in real and imaginary parts as in (4.7) and by using the recurrence relations [73]

$$J_{n+1}(x) + J_{n-1}(x) = (2n/x)J_n(x) \quad (4.17)$$

$$J_{n-1}(x) - J_{n+1}(x) = 2J'_n(x), \quad (4.18)$$

for the Bessel function. In particular, note that while the KW displacement vector of equation (4.11) is proportional to l/L and thus becomes vanishingly small in the limit $|l| \ll L$, the second term of equation (4.16) remains finite in this limit except in the case of linearly polarized light where the \mathbf{d}_2 component of the general displacement vector (4.6) is identically zero. The KW factorization in terms of the field-free scattering cross-section and the field-induced photon-exchange probability factor, $J_l^2(L)$, can, accordingly, not be generalized to elliptical polarization even in the limit where the weak field correction is small. In the other extreme, $|l| \gg L$, it is readily seen by considering the pertaining power series expansion of $J_l(L)$ [73] that also the second term becomes effectively proportional to l/L such that both terms diverge in the classically forbidden limit. Thus, while often of minor importance for sufficiently weak fields in the classically allowed region ($|l| \leq L$), it is essential to account carefully for these displacements as the classically forbidden region is approached. For linearly polarized light, we obtain the KW formula from the first term of equation (4.16) by a linear approximation which is valid if $|\gamma| \ll q_i$ and additionally the variation in amplitude and phase of $T_{\mathbf{q}_i}(\mathbf{Q})$ is sufficiently small (see the discussion following equation (4.11)).

We obtain the zero-order soft-photon (ZOSP) approximation from the WFSP approximation by neglecting also terms linear in A_0

$$\mathcal{T}_l^{\text{ZOSP}}(\mathbf{Q}) = J_l(L)T_{\mathbf{q}_i}(\mathbf{Q}). \quad (4.19)$$

As is well known, this approximation merges with the KW approximation in the soft-photon limit in the classically allowed region for linearly polarized fields, but the soft-photon approximation is generally an insufficient condition for the coalescence of the ZOSP and KW theories since the generalized displacements include terms proportional to A_0 . This conclusion is further substantiated by the calculations presented in chapter 5.

4.1.4 The weak-field soft-photon theory

The weak-field soft-photon approximation was developed in [44] in case of linearly polarized light. In the preceding section, the WFSP theory was derived from the impulse approximation. This is a valid approach as long as only terms proportional to A_0 are accounted for. In this section, we present the general derivation of the WFSP amplitude. The relevant amendments for inclusion of higher order terms in A_0 are identified. Kelsey and Rosenberg also considered the quantum field approach for arbitrary polarization [72]. In the Schrödinger picture, the electromagnetic vector potential operator is taken as

$$\hat{\mathbf{A}} = \beta (\boldsymbol{\epsilon}\hat{a} + \boldsymbol{\epsilon}^*\hat{a}^\dagger). \quad (4.20)$$

We have introduced the dipole approximation, and \hat{a} and \hat{a}^\dagger are time-independent annihilation and creation operators pertaining to a single field mode, while ϵ is the polarization vector of elliptically polarized light given by (3.2). The parameter β depends formally on the quantization volume, but in the laser approximation which is characterized by a very large number of photons, N , in the considered mode, β is directly related to A_0 , and in turn according to equation (3.5) to the intensity, I , as

$$\beta = \frac{A_0}{2\sqrt{N}} = \frac{1}{2\omega} \sqrt{\frac{I}{N}}. \quad (4.21)$$

When $\hat{\mathbf{A}}$ is sandwiched between number states of the field, the photon number cancels perfectly out. The derivation of the WFSP T -matrix follows closely the presentation in [44]. The Hamiltonian describing the system is

$$H = \hat{\mathbf{p}}^2/2 + \omega \hat{a}^\dagger \hat{a} + V + \hat{\mathbf{A}}\hat{\mathbf{p}}, \quad (4.22)$$

where V is a local atomic potential and $\hat{\mathbf{A}}\hat{\mathbf{p}}$ is the electron-field interaction. Neglecting the $\hat{\mathbf{A}}^2$ -term is consistent with the weak-field approximation. Note that the relative phase between the two components of the field operator has been taken to vanish at the origin. It is readily shown that the theory is independent of this arbitrary choice, consistent with the fact that time is a dummy parameter in a scattering process involving a continuous wave.

In the time-independent formulation, exact scattering states, i.e. energy eigenstates satisfying suitable boundary conditions, are sought as solutions to the stationary Schrödinger equation

$$(E - H)|\Psi_{\mathbf{q}}^\pm, N\rangle = 0. \quad (4.23)$$

The independent parameters of the scattering states, $|\Psi_{\mathbf{q}}^\pm, N\rangle$, represent the asymptotic momentum of the electron, \mathbf{q} , and the asymptotic number of photons, N , in the considered mode of the laser field. [In the laser approximation, Thomson scattering can be ignored since stimulated processes exceed spontaneous ones by an enormous factor [29].] The total energy, E , is given by

$$E = \frac{1}{2}q^2 + N\omega. \quad (4.24)$$

In the absence of the atomic potential, the energy eigenstates satisfy

$$\left(E - (\hat{\mathbf{p}}^2/2 + \omega \hat{a}^\dagger \hat{a} + \hat{\mathbf{A}}\hat{\mathbf{p}}) \right) |\chi_{\mathbf{q}}, N\rangle = 0. \quad (4.25)$$

Solutions are sought in the form of an expansion in the complete set of unperturbed states [72]

$$|\chi_{\mathbf{q}}, N\rangle = |\mathbf{q}\rangle \sum_{n=-\infty}^{\infty} \gamma_n |N+n\rangle, \quad (4.26)$$

where $\langle \mathbf{r} | \mathbf{q} \rangle = \exp(i\mathbf{q}\mathbf{r})$ is an electron plane-wave state and $|N\rangle$ is a number state of the photon field. The sum over n represents a virtual distribution over photon number states relative to some very large photon number, N . Real transitions do of course only take place in the vicinity of another particle which can accommodate the momentum transfer. Substituting (4.26) into (4.25) gives a recursion relation in γ_n :

$$2n\gamma_n = -\frac{A_0}{\omega} |\boldsymbol{\epsilon}\mathbf{q}| e^{i\phi} \gamma_{n+1} - \frac{A_0}{\omega} |\boldsymbol{\epsilon}\mathbf{q}| e^{-i\phi} \gamma_{n-1}, \quad (4.27)$$

which is accurate to order $n/N \ll 1$. Here we have introduced

$$\boldsymbol{\epsilon}\mathbf{q} = |\boldsymbol{\epsilon}\mathbf{q}| e^{i\phi}. \quad (4.28)$$

Equation (4.27) is similar to the recursion formula for the Bessel function and it is fulfilled by $\gamma_n = J_{-n}(A_0|\boldsymbol{\epsilon}\mathbf{q}|/\omega)e^{-in\phi}$. The solutions are, accordingly,

$$|\chi_{\mathbf{q}}, N\rangle = |\mathbf{q}\rangle \sum_{n=-\infty}^{\infty} J_{-n}\left(\frac{A_0}{\omega} |\boldsymbol{\epsilon}\mathbf{q}|\right) e^{-in\phi} |N+n\rangle. \quad (4.29)$$

These states are the quantum equivalents of the Volkov states representing an electron in a classical field [7]. They were derived by Kelsey and Rosenberg [72] and they satisfy equation (4.25) with the energy

$$E = \frac{1}{2}q^2 + N\omega. \quad (4.30)$$

In the case of linear polarization, an analytical solution still exists if the $\hat{\mathbf{A}}^2$ -term is included in (4.25). The Volkov state is then expressed in terms of generalized Bessel functions [74] which depend upon the ponderomotive potential. Under the conditions of the experiments of Wallbank and Holmes [26, 27], $U_p \sim 0.01\omega$ and the ponderomotive term, and therefore the \mathbf{A}^2 -term, can be safely ignored.

Considering the scattering potential to be of short range and the actual laser field to be switched on and off adiabatically, the Volkov states may be taken to represent the asymptotic states for the scattering process. The scattering amplitude is accordingly to be extracted from the T -matrix element

$$\mathcal{T} = \langle \chi_{\mathbf{q}_f}, N_f | V | \Psi_{\mathbf{q}_i}^+, N_i \rangle, \quad (4.31)$$

where $|\Psi_{\mathbf{q}_i}^+, N_i\rangle$ is the scattering state which develops from the asymptotic Volkov state, $|\chi_{\mathbf{q}_i}, N_i\rangle$. The corresponding cross-section for laser-assisted scattering is obtained in the usual way from the absolute square of the T -matrix element. The scattering state is given by the Lippmann-Schwinger equation

$$|\Psi_{\mathbf{q}_i}^+, N_i\rangle = |\chi_{\mathbf{q}_i}, N_i\rangle + \mathcal{G}^+(E_i) V |\chi_{\mathbf{q}_i}, N_i\rangle, \quad (4.32)$$

where E_i , according to (4.30), is given by $E_i = \frac{1}{2}q_i^2 + N_i\omega$ and where \mathcal{G}^+ is the Greens function

$$\mathcal{G}^+(E) = \lim_{\eta \rightarrow 0^+} \frac{1}{E + i\eta - H}. \quad (4.33)$$

As usual in scattering theory, it is not possible to evaluate the T -matrix in exact form. The theory presented in the following will be based on two assumptions, which we shall refer to as the weak-field (WF) approximation and the soft-photon (SP) approximation. These approximations are independent of each other since the WF approximation depends upon the amplitude of the vector potential of the laser field while the SP approximation depends upon the frequency. However, since $A_0 = \omega\alpha_0\sec(\xi/2)$, where α_0 is the classical quiver radius, it is formally possible [33, 34] to identify ω as a common order parameter in combined WF and SP expansions. The drawback by such an approach is that keeping α_0 constant while letting $\omega \rightarrow 0$ implies that the intensity decreases (see equation (3.5)) and that the perturbative regime is unintentionally entered. A formal unification of the WF and the SF approximation is therefore physically misleading, and we shall carefully distinguish between the two different types of expansions in the following. First, we introduce the WF approximation. Hence, expanding the Lippmann-Schwinger equation (4.32) to first order in the interaction with the photon field, we get

$$|\Psi_{\mathbf{q}_i}^+, N_i\rangle \simeq [1 + \mathcal{G}_0^+(E_i)V + \mathcal{G}_0^+(E_i)\hat{\mathbf{A}}\hat{\mathbf{p}}\mathcal{G}_0^+(E_i)V]|\chi_{\mathbf{q}_i}, N_i\rangle, \quad (4.34)$$

where \mathcal{G}_0^+ is the interaction-free ($\hat{\mathbf{A}}\hat{\mathbf{p}}$ -free) Greens function

$$\mathcal{G}_0^+(E) = \lim_{\eta \rightarrow 0^+} \frac{1}{E + i\eta - (\hat{\mathbf{p}}^2/2 + V) - \omega\hat{a}^\dagger\hat{a}}. \quad (4.35)$$

The first order WF approximation for the T -matrix then reads

$$\mathcal{T}^{\text{WF}} = \langle \chi_{\mathbf{q}_f}, N_f | \hat{T}^{\text{WF}} | \chi_{\mathbf{q}_i}, N_i \rangle \quad (4.36)$$

with the weak-field transition operator given by

$$\hat{T}^{\text{WF}} = V + V\mathcal{G}_0^+(E_i)V + V\mathcal{G}_0^+(E_i)\hat{\mathbf{A}}\hat{\mathbf{p}}\mathcal{G}_0^+(E_i)V. \quad (4.37)$$

Higher order terms may become significant when multiphoton processes are considered in critical geometries corresponding to classically forbidden scattering processes. Note that the distorted-wave perturbation series generally combines photon exchange via virtual excitations in initial and final states with direct photon exchange via a sequence of dipole allowed interactions with the photon field during the intermediate propagation of the electron in the atomic potential. Using the Volkov state from (4.29) it is now, in principle, a simple matter to evaluate the T -matrix. The first term from (4.36) can be evaluated directly and gives the first Born result

$$\mathcal{T}_l^{(0)} = \sum_{n=-\infty}^{\infty} \langle \mathbf{q}_f | V | \mathbf{q}_i \rangle J_{-n}\left(\frac{A_0}{\omega} |\boldsymbol{\epsilon}\mathbf{q}_i|\right) e^{-in\phi_i} J_{l-n}\left(\frac{A_0}{\omega} |\boldsymbol{\epsilon}\mathbf{q}_f|\right) e^{-i(l-n)\phi_f}, \quad (4.38)$$

where $l = N_f - N_i$ describes the number of photons emitted ($l > 0$) or absorbed ($l < 0$) by the scattered electron. To evaluate the remaining terms in (4.36),

we introduce the SP approximation, i.e. we assume that $\omega \ll q_i^2/2$. Expanding to first order in ω in the second term in (4.36) gives two contributions. This follows from the result

$$\langle N_f + m | \mathcal{G}_0^+(E_i) | N_i + n \rangle = \delta_{N_f+m, N_i+n} G^+(E_i - (N_i + n)\omega), \quad (4.39)$$

where

$$G^+(E) = \lim_{\eta \rightarrow 0^+} \frac{1}{E + i\eta - (\hat{\mathbf{p}}^2 + V)} \quad (4.40)$$

is the Greens function for ordinary potential scattering and

$$G^+(E_i - (N_i + n)\omega) \simeq G^+(q_i^2/2) + G^+(q_i^2/2)n\omega G^+(q_i^2/2) \quad (4.41)$$

to first order in ω . Explicitly the two terms are

$$\begin{aligned} \mathcal{T}_{l,a}^{(1)} &= \sum_{n=-\infty}^{\infty} \langle \mathbf{q}_f | V G^+(q_i^2/2) V | \mathbf{q}_i \rangle \\ &\quad \times J_{-n} \left(\frac{A_0}{\omega} | \boldsymbol{\epsilon} \mathbf{q}_i | \right) e^{-in\phi_i} J_{l-n} \left(\frac{A_0}{\omega} | \boldsymbol{\epsilon} \mathbf{q}_f | \right) e^{-i(l-n)\phi_f} \end{aligned} \quad (4.42)$$

$$\begin{aligned} \mathcal{T}_{l,b}^{(1)} &= \sum_{n=-\infty}^{\infty} \langle \mathbf{q}_f | V G^+(q_i^2/2) n\omega G^+(q_i^2/2) V | \mathbf{q}_i \rangle \\ &\quad \times J_{-n} \left(\frac{A_0}{\omega} | \boldsymbol{\epsilon} \mathbf{q}_i | \right) e^{-in\phi_i} J_{l-n} \left(\frac{A_0}{\omega} | \boldsymbol{\epsilon} \mathbf{q}_f | \right) e^{-i(l-n)\phi_f}. \end{aligned} \quad (4.43)$$

The last term of (4.36) is analysed similarly. To first order in ω the result is

$$\begin{aligned} \mathcal{T}_l^{(2)} &= \sum_{n=-\infty}^{\infty} \langle \mathbf{q}_f | V G^+(q_i^2/2) \mathbf{p} G^+(q_i^2/2) V | \mathbf{q}_i \rangle \\ &\quad \times \frac{A_0}{2} \left[\boldsymbol{\epsilon} J_{-n} \left(\frac{A_0}{\omega} | \boldsymbol{\epsilon} \mathbf{q}_i | \right) e^{-in\phi_i} J_{l+1-n} \left(\frac{A_0}{\omega} | \boldsymbol{\epsilon} \mathbf{q}_f | \right) e^{-i(l+1-n)\phi_f} \right. \\ &\quad \left. + \boldsymbol{\epsilon}^* J_{-n} \left(\frac{A_0}{\omega} | \boldsymbol{\epsilon} \mathbf{q}_i | \right) e^{-in\phi_i} J_{l-1-n} \left(\frac{A_0}{\omega} | \boldsymbol{\epsilon} \mathbf{q}_f | \right) e^{-i(l-1-n)\phi_f} \right]. \end{aligned} \quad (4.44)$$

Notice that the present derivation assumes that the Greens functions are slowly varying on the scale of ω . If the potential supports a resonance in the vicinity of the energy of the incoming electron, this assumption does not remain valid since in this case it is possible to reach the resonance energy by exchange of a finite number of photons. Hence, the present development is restricted to situations where we are well off resonance energies. The theory is extended to include situations where the atomic potential supports a resonance in section 4.3. The terms in (4.38), (4.42), (4.43) and (4.44) may be simplified by application of Graf's addition theorem [73]. For example, with $z_j = r_j e^{i\phi_j}$ ($j = 1, 2, 3$), the following relations:

$$\sum_k J_k(r_1) e^{-ik\phi_1} J_{k+l}(r_2) e^{i(k+l)\phi_2} = J_l(r_3) e^{il\phi_3} \quad (4.45)$$

$$\sum_k k J_k(r_1) e^{-ik\phi_1} J_{k+l}(r_2) e^{i(k+l)\phi_2} = \frac{1}{2} \left(J_{l-1}(r_3) e^{i[(l-1)\phi_3 + \phi_1]} \right. \quad (4.46)$$

$$\left. + J_{l+1}(r_3) e^{i[(l+1)\phi_3 - \phi_1]} \right),$$

where $z_3 = z_1 - z_2$ are readily established. As detailed in appendix A, we obtain the following expression for the l -photon laser-assisted T -matrix element (leaving out an overall phase factor)

$$\mathcal{T}_l^{\text{WFSP}}(\mathbf{Q}) = J_l(L) T_{\mathbf{q}_i}(\mathbf{Q}) + \frac{A_0}{2} [\mathbf{d} J_{l+1}(L) + \mathbf{d}^* J_{l-1}(L)] \nabla_{\mathbf{q}_i} T_{\mathbf{q}_i}(\mathbf{Q}), \quad (4.47)$$

which is identical to the WFSP T -matrix given by (4.15). The WFSP T -matrix is reproduced in (4.47) due to the discussion in the following. The dependence on the number l of exchanged photons and on the electron momentum transfer $\mathbf{Q} = \mathbf{q}_f - \mathbf{q}_i$ is explicitly indicated. The half-shell potential-scattering T -matrix elements on the rhs of (4.47) are defined by

$$T_{\mathbf{q}}(\mathbf{Q}) = \langle \mathbf{q} + \mathbf{Q} | V + V G^+(q^2/2) V | \mathbf{q} \rangle, \quad (4.48)$$

while the displacement vector \mathbf{d} is given by equation (4.7). The phase, τ , is given by equation (3.9) and the argument of the Bessel functions, which governs the weight of the l -photon exchange channel, is given by the classical cut-off in the number of exchanged photons (2.7). (Note in passing that the gradient of the T -matrix in equation (4.15) was rewritten in [44] in terms of half-shell T -matrix elements evaluated at shifted momenta. This procedure is legitimate to first order in the frequency, but introduces an asymmetry in the dependence of the final result on the sign of ϵ . The expression in equation (4.15) does not have this asymmetry and is therefore to be preferred, despite the fact that equation (36) rather than equation (42) of reference [44] was denoted the main result of the WFSP theory.)

For $L = 0$ equation (4.47) simplifies to

$$\mathcal{T}_l^{\text{WFSP}}(\mathbf{Q}) = \delta_{l,\pm 1} \frac{A_0}{2} (\mathbf{d}_1 \nabla_{\mathbf{q}_i} T_{\mathbf{q}_i}(\mathbf{Q}) \mp i \mathbf{d}_2 \nabla_{\mathbf{q}_i} T_{\mathbf{q}_i}(\mathbf{Q})). \quad (4.49)$$

The rhs is readily traced to result from first order perturbation theory for free-free transitions. It is clear from (4.49) that the present form of the theory is invalid for $|l| \geq 2$ in some region around $L = 0$. In this region, it becomes important to retain terms in the perturbation expansion up to order $n = |l|$. In fact, examining the standard n 'th-order perturbation contribution and keeping track of powers of L for $L \ll 1$, it is readily seen that the effective order parameter appears in the combination

$$A_0^n L^{|l|-n}. \quad (4.50)$$

The present theory is accordingly expected to be valid for arbitrary l -values if $A_0 \ll L = A_0 |\epsilon \mathbf{Q}| / \omega$, i.e. when the following condition is satisfied

$$\rho = \frac{A_0}{L} = \frac{\omega}{|\epsilon \mathbf{Q}|} \ll 1. \quad (4.51)$$

In the region where $\rho \gtrsim 1$, however, the WFSP theory is applicable only for $l = \pm 1$. To obtain a proper theory in this region for $|l| \geq 2$, it is important to retain terms up to $|l|$ 'th order in the perturbation expansion for free-free transitions. This aspect of the theory is discussed in more detail in connection with figure 5.3. Notice that the condition in (4.51) is independent of l while the KW expansion parameter is proportional to the number of exchanged photons (see equation (4.11)).

The expression in (4.47) represents a consistent expansion of the weak-field approximation given by (4.36) to include all terms of first order in ω and is therefore referred to as the weak-field soft-photon (WFSP) approximation. Explicit evaluations of the WFSP will be presented in chapter 5. The off-shell character of the T -matrix element on the rhs of (4.47) is controlled by energy conservation, which trivially leads to the fact that the element $T_{q_i}(\mathbf{Q})$ is off-shell by the amount $l\omega$ and therefore clearly near the energy shell in the soft-photon limit. Since the T -matrix for scattering in a short-range potential generally behaves smoothly in the near-shell limit, it is a valid approximation to replace the half-shell T -matrix elements by their on-shell limits, i.e. by corresponding elastic scattering amplitudes

$$T_{\mathbf{q}}(\mathbf{Q}) \approx -2\pi f_q(\theta), \quad (4.52)$$

where $\tan \theta/2 = Q/(2q)$. Recent calculations indicate that the on-shell approximation is invalid for scattering in long-range polarization potentials [48]. The weak-field condition is satisfied in typical free-free experiments [26, 27, 75], but inclusion of the ponderomotive potential may become essential in the future when stronger laser fields are considered. Ponderomotive terms give rise to more pronounced off-shell effects. The expression in (4.47) with the approximation in (4.52) represents a form of the WFSP approximation which is readily evaluated since scattering amplitudes are available in the literature for many practical cases and can otherwise be generated by standard methods. Note that the phase variation of the scattering amplitude is important for a proper addition of the contributions in equation (4.47).

4.2 Scattering by the zero-range potential in circularly polarized light

The problem of scattering by a zero-range potential

$$V(r) = \frac{2\pi}{\kappa} \delta(\mathbf{r}) \frac{\partial}{\partial r} r \quad (4.53)$$

in circularly polarized laser light has been solved exactly by Berson [55]. The result for the scattering amplitude accompanied with the exchange of l photons

reads²

$$f_l = -i^l \sum_{n=-\infty}^{\infty} \frac{\exp(-in(\phi_f - \phi_i)) J_n(\alpha_0 q_i \sin\theta_i) J_{n+l}(\alpha_0 q_f \sin\theta_f)}{\mathcal{F}(\kappa, \alpha_0, n, \omega, q_i)}. \quad (4.54)$$

Here θ and ϕ denote the angular coordinates of the electron with respect to the laser beam direction while \mathcal{F} is given by

$$\mathcal{F}(\kappa, \alpha_0, n, \omega, q_i) = \kappa + i \sum_{s=0}^{\infty} \sum_{m=-s}^s (-1)^{m+s} \frac{\alpha_0^{2s} (q_i^2 + 2(m+n)\omega)^{s+1/2}}{(2s+1)(s-m)!(s+m)!}. \quad (4.55)$$

The parameter κ is related to the energy of the bound state in the zero-range potential, $\mathcal{E}_0 = -\kappa^2/2$ [55], or, equivalently, to the s -wave scattering length $a_0 = 1/\kappa$ [54] while $\alpha_0 = A_0/(\sqrt{2}\omega)$ is the quiver radius for circularly polarized light (see equation (3.4)). In the present treatment, κ is chosen to be $\kappa = 0.85$, corresponding to the s -wave scattering length for helium [76]. Although (4.54) provides the exact scattering amplitude, it is our experience that the structure of equation (4.55) impedes a practical evaluation of the cross-section for large values of α_0 , corresponding to high intensities and (or) very low frequencies.

An expansion to zero order in the field, or equivalently to zero order in α_0 , of \mathcal{F} gives

$$\mathcal{F}_0 = \kappa + i\sqrt{q_i^2 + n\omega}. \quad (4.56)$$

Inserting this approximation into equation (4.54) and using the low-frequency approximation, $\omega \ll q_i^2/2$, immediately provides the ZOSP factorization of the laser-assisted scattering cross-section as given by equation (4.19).

The field-free scattering from a zero-range potential has been studied in detail by Demkov and Ostrovsky [54]. The half-shell T -matrix is given by

$$T_{\mathbf{q}_i}(\mathbf{Q}) = -\frac{1}{2\pi(\kappa + iq_i)}, \quad (4.57)$$

which is isotropic and entirely independent of off-shell effects. Accordingly, the zero-range potential is ideal for testing weak-field aspects of the theory independently of the inherent application of the soft-photon approximation.

4.3 Resonant laser-assisted electron scattering

Ignoring the last term of the transition operator in equation (4.37) and using the expression (4.29) for the Volkov states, the zero-order approximation is obtained

$$\begin{aligned} \mathcal{T}_l^{\text{ZO}} &= \sum_{m=-\infty}^{\infty} J_{l-m} \left(\frac{A_0}{\omega} |\boldsymbol{\epsilon} \mathbf{q}_f| \right) e^{-i(l-m)\phi_f} \langle \mathbf{q}_f | V + VG^+(\epsilon_i - m\omega) V | \mathbf{q}_i \rangle \\ &\quad \times J_{-m} \left(\frac{A_0}{\omega} |\boldsymbol{\epsilon} \mathbf{q}_i| \right) e^{-im\phi_i}, \end{aligned} \quad (4.58)$$

²A minor correction has been made in the argument of the Bessel function since Berson [55] incorrectly includes the ponderomotive shift in the kinetic energy to define the asymptotic linear electron momentum of the Volkov waves.

where G^+ , as before, is the full Green function for the electron-atom system. The summation index in equation (4.58) represents the number of virtual photons absorbed ($m < 0$) or emitted ($m > 0$) before the scattering event while l denotes the number of exchanged photons. We consider a situation where the potential supports a resonance or a series of resonances located in the complex energy plane at $\mathcal{E}_n^r = \epsilon_n^r - \frac{1}{2}i\Gamma_n$. The Green function corresponding to the energy $\epsilon = q^2/2$ may then be expressed as $G^+(\epsilon) = G_{\text{bg}}^+(\epsilon) + G_{\text{r}}^+(\epsilon)$ in terms of a slowly varying background, $G_{\text{bg}}^+(\epsilon)$, and a resonance part, $G_{\text{r}}^+(\epsilon) = \sum_n [\epsilon - \mathcal{E}_n^r]^{-1} |\phi_n\rangle \langle \phi_n|$, where $|\phi_n\rangle$ may be interpreted as the n 'th resonance state. Neglecting the photon energy dependence in the non-resonant part, i.e. making the soft-photon approximation, we obtain

$$\begin{aligned} \mathcal{T}_l^{\text{ZOSP}} &= J_l(L) T^{\text{bg}}(\mathbf{q}_i, \mathbf{q}_f, \epsilon_i) \\ &+ \sum_{m=-\infty}^{\infty} J_{l-m} \left(\frac{A_0}{\omega} |\boldsymbol{\epsilon} \mathbf{q}_f| \right) e^{-i(l-m)\phi_f} \sum_n T_n^{\text{r}}(\mathbf{q}_i, \mathbf{q}_f, \epsilon_i - m\omega) \\ &\times J_{-m} \left(\frac{A_0}{\omega} |\boldsymbol{\epsilon} \mathbf{q}_i| \right) e^{-im\phi_i}, \end{aligned} \quad (4.59)$$

where the off-shell character of the T -matrix elements is explicitly indicated and where the resonant part is a sum of individual pole contributions. This result, first given by Jung and Taylor [60], has provided a frame for tests between experiments and theory [61, 62, 63]. The Bessel function factor in the first term suppresses the non-resonant contribution in the classically forbidden region. Accordingly, one expects to measure pure Breit-Wigner peaks in this situation if the considered resonances are well separated. Equation (4.59) has a nice physical interpretation. Consider, as an example, an experiment where the detected electron has emitted *one* photon during the scattering event ($l = 1$) and specialize, e.g. to the term $J_2(A_0 |\boldsymbol{\epsilon} \mathbf{q}_f| / \omega) T^{\text{r}}(\mathbf{q}_i, \mathbf{q}_f, \epsilon_i + \omega) J_1(A_0 |\boldsymbol{\epsilon} \mathbf{q}_i| / \omega)$. The resonance amplitude $T^{\text{r}}(\mathbf{q}_i, \mathbf{q}_f, \epsilon)$ only gives a significant contribution when ϵ is close to one of the resonance energies, i.e. when $\epsilon_i \sim \epsilon_n^r - \omega$. Thus, the above-mentioned term represents an electron that first absorbs a photon, then scatters resonantly off the target and finally emits two photons in leaving the scattering region. The remaining terms may be analysed similarly. Notice that the Bessel function amplitude eventually decreases with increasing order, leaving in practice only a few significant terms.

As discussed in section 4.1 and as documented in [44, 38], it is essential to go beyond the ZO approximation when studying free-free transitions in the classically forbidden region ($|l| \geq L$) corresponding to the critical geometry. Additionally, it is important *not* to make the linear approximation implied by the KW approach since the corresponding expansion parameter diverges as the critical geometry is approached. In the WFSP theory, we expand to first order in the coupling with the photon field and make an expansion to first order in the small photon energy, ω . When dealing with resonances we obviously have to go to the same order, at least. It is then intuitively obvious to make the

substitution $J_l(L)T^{\text{bg}} \rightarrow \mathcal{T}_{l,\text{bg}}^{\text{WFSP}}(\mathbf{Q})$ in equation (4.59) to obtain

$$\begin{aligned} \mathcal{T}_l^{\text{WFSP}} &= \mathcal{T}_{l,\text{bg}}^{\text{WFSP}}(\mathbf{Q}) \\ &+ \sum_{m=-\infty}^{\infty} J_{l-m}\left(\frac{A_0}{\omega}|\boldsymbol{\epsilon}\mathbf{q}_f|\right)e^{-i(l-m)\phi_f} \sum_n T_n^r(\mathbf{q}_i, \mathbf{q}_f, \epsilon_i - m\omega) \\ &\quad \times J_{-m}\left(\frac{A_0}{\omega}|\boldsymbol{\epsilon}\mathbf{q}_i|\right)e^{-im\phi_i}, \end{aligned} \quad (4.60)$$

where the explicit form of the first term is given by (4.47) in terms of appropriate background T -matrix elements. Starting from (4.36), it is not difficult to derive the expression in (4.60) following the expansion procedure outlined in [77]. The intermediate steps do, however, involve complicated terms describing multiple scattering sequences, and since an evaluation of these terms is beyond the scope of this presentation they shall not be reproduced here. Simple estimates of the discarded terms can be found in [77]. A strict justification for their elimination is difficult to find. The off-shell character of the T -matrix elements is controlled by energy conservation. As in section 4.1, it is seen that the T -matrix elements are near the energy shell in the soft-photon approximation. Since the T -matrix for scattering in a short-range potential is expected to behave smoothly in the near-shell limit, it is probably a valid approximation to replace the background component as well as the resonant part of the T -matrix by the corresponding on-shell limit, i.e. by corresponding elastic scattering amplitudes (see equation (4.52)). The resonant weak-field soft-photon theory in (4.60) is then readily evaluated. As in section 4.1, the on-shell approximation should be contrasted with recent results [48].

4.4 Two-colour laser-assisted scattering

Measurements on two-colour above-threshold ionization show a strong dependence on the relative phase between the two colours [30]. Two-colour interference effects are also seen in high harmonic generation [31]. Coherent phase control of free-free transitions in two-colour fields has been investigated theoretically [78, 43]. In the present section, we consider laser-assisted scattering with two parallel lasers. We will concentrate on photon correlation effects [41]. A discussion of decoherence introduced by dispersion in the electron-atom collision system is presented in chapter 6. Experiments on laser-assisted electron scattering demonstrate that the ZOSP approximation provides a good description of the scattering process in the classically allowed region [4]. We apply the ZOSP approximation in non-critical geometries in the following.

The number states used in the description of the asymptotic Volkov waves of section 4.1.4 are phase indeterminate. A theory accounting for interference effects between two laser beams is conveniently formulated with coherent (Glauber) states. The state of the field prior to the scattering is taken to be a product of two coherent states: $|\alpha_1\rangle|\alpha_2\rangle$. The relative dispersion in the field amplitude of a coherent state vanishes as $|\alpha| \rightarrow \infty$.

As the electron enters the laser field, the combined system of the field and the electron evolves adiabatically into a two-colour dressed state. For simplicity, we first consider the one-colour case. The coherent state is

$$|\alpha(t)\rangle = \sum_{N=0}^{\infty} \langle N|\alpha\rangle e^{-iN\omega t} |N\rangle. \quad (4.61)$$

The coefficient $\langle N|\alpha\rangle = \exp(-|\alpha|^2/2)\alpha^N/\sqrt{N!}$ peaks strongly at $|\alpha| = \sqrt{N}$. The summation in (4.61) is thus restricted to a narrow band of N -values and within this band, the coupling between each individual number state, $|N\rangle$, and the projectile electron is described by the Volkov states of section 4.1.4. Accordingly, we get the following state in the case of a coherent light field

$$|\chi_q, \alpha(t)\rangle = |\mathbf{q}\rangle \sum_N' \langle N|\alpha\rangle e^{-i(N\omega+q^2/2)t} \sum_n J_{-n}\left(\frac{A_0^\alpha}{\omega}|\boldsymbol{\epsilon}\mathbf{q}\right) e^{-in\phi} |N+n\rangle. \quad (4.62)$$

where the superscript α of the vector potential amplitude indicates its dependence on the field: $A_0^\alpha = 2\beta|\alpha| = 2\beta\sqrt{N}$ (see also equation (4.21)). The prime denotes the restricted set of N -values. This state clearly evolves into a plane wave times a coherent state as the field is adiabatically turned off and will be referred to as a *Glauber-Volkov* state. The time-dependent Glauber-Volkov state is the quantum analogue of the semi-classical Volkov state.

The Glauber-Volkov state is readily generalized to two-colour fields:

$$\begin{aligned} |\chi_q, \{\alpha_1, \alpha_2\}(t)\rangle &= |\mathbf{q}\rangle \sum_{N_1, N_2}' \langle N_1|\alpha_1\rangle \langle N_2|\alpha_2\rangle e^{-i(N_1\omega_1+N_2\omega_2+q^2/2)t} \\ &\times \sum_{n_1, n_2} J_{-n_1}\left(\frac{A_{01}^{\alpha_1}}{\omega_1}|\boldsymbol{\epsilon}_1\mathbf{q}\right) J_{-n_2}\left(\frac{A_{02}^{\alpha_2}}{\omega_2}|\boldsymbol{\epsilon}_2\mathbf{q}\right) e^{-in_1\phi_1} e^{-in_2\phi_2} \\ &\times |N_1+n_1\rangle |N_2+n_2\rangle, \end{aligned} \quad (4.63)$$

where the two fields are denoted by 1 and 2, respectively. The Glauber-Volkov states may be derived very elegantly with the displacement operator technique [29, 79, 80]. We use the time-dependent S -matrix theory to formulate the theory of scattering between Glauber-Volkov states. The time integral of the S -matrix leads to energy delta functions defining channels with different numbers of exchanged photons. This effectively leads to the T -matrix formulation of section 4.1, except for additional summations

$$\sum_{N_j} \langle \beta_j | N_j + l_j \rangle \langle N_j | \alpha_j \rangle. \quad (4.64)$$

This sum illustrates that $|\alpha_j\rangle$ develops into $|\beta_j\rangle$ while the electron exchanges l_j photons with the field ($j = 1, 2$). Remembering the peaked behaviour of $\langle N_j | \alpha_j \rangle$ the sum over N_j can be done with the result $e^{il_j\varphi_j} \langle \beta_j | \alpha_j \rangle$ which depends on the phase of the field φ_j . The two-colour ZOSP T -matrix is

$$\mathcal{T}_{l_1, l_2}^{\text{coh}}(\mathbf{Q}) = T_{\mathbf{q}_i}(\mathbf{Q}) \langle \beta_1 | \alpha_1 \rangle \langle \beta_2 | \alpha_2 \rangle e^{il_1(\varphi_1 - \tau_1)} e^{il_2(\varphi_2 - \tau_2)} J_{l_1}(L_1^{\alpha_1}) J_{l_2}(L_2^{\alpha_2}), \quad (4.65)$$

where the photons exchanged with the two fields enter the energy conserving relation : $q_f^2/2 - q_i^2/2 + l_1\omega_1 + l_2\omega_2 = 0$ and where $L_j^{\alpha_j}$ depends on α_j through $A_{0j}^{\alpha_j}$. The half-shell T -matrix on the rhs of (4.65) is given by equation (4.48). To construct the cross-section, we consider that different combinations of l_1 and l_2 contribute to the same $q_i^2/2 \rightarrow q_f^2/2$ process and coherently add $\mathcal{T}_{l_1, l_2}^{\text{coh}}(\mathbf{Q})$ -terms in accordance with energy conservation. We take the modulus squared, sum up unresolved final states and average over initial states to get the cross-section. Taking the ordinary kinematical factors into account and using the completeness relation, $\frac{1}{\pi} \int d^2\beta_j |\beta_j\rangle\langle\beta_j| = 1$, we get

$$\begin{aligned} \left\langle \frac{d\sigma}{d\Omega}(\mathbf{Q}, l_1, l_2) \right\rangle &= \frac{q_f}{q_i} \frac{d\sigma^{\text{el}}}{d\Omega}(\mathbf{Q}) \int d^2\alpha_1 \int d^2\alpha_2 P(\alpha_1, \alpha_2) \left| \sum'_{l_1, l_2} J_{l_1}(L_1^{\alpha_1}) \right. \\ &\quad \left. \times J_{l_2}(L_2^{\alpha_2}) e^{i(l_1(\varphi_1 - \tau_1) + l_2(\varphi_2 - \tau_2))} \right|^2, \end{aligned} \quad (4.66)$$

where $d\sigma^{\text{el}}(\mathbf{Q})$ is the field-free cross-section corresponding to $T_{q_i}(\mathbf{Q})$ and the joint P -representation of the fields α_1 and α_2 is $P(\alpha_1, \alpha_2)$. Expressions for P of a coherent state and a chaotic field state are available in [81]. In practice, the actual form of the P -representation is dictated by the way the two colours are made in the considered experiment. If the two colours are made by two different lasers, they are independent and $P(\alpha_1, \alpha_2)$ factorizes. In the following, we first consider two independent coherent fields and then two independent chaotic fields. For the coherent state, $P(\alpha) = \delta^2(\alpha - \tilde{\alpha})$, and we find

$$\left\langle \frac{d\sigma}{d\Omega}(\mathbf{Q}) \right\rangle_{\text{coh}} = \frac{q_f}{q_i} \frac{d\sigma^{\text{el}}}{d\Omega} \left| \sum'_{l_1, l_2} J_{l_1}(L_1) J_{l_2}(L_2) e^{i(l_1(\varphi_1 - \tau_1) + l_2(\varphi_2 - \tau_2))} \right|^2. \quad (4.67)$$

The phase dependence is due to the phase locking in the P -representation of the coherent state. In the case of chaotic states, $P(\alpha) = e^{-|\alpha|^2/|\tilde{\alpha}|^2}/(\pi|\tilde{\alpha}|^2)$ and the statistical average is a little more delicate. Writing $\alpha_j = r_j e^{i\theta_j}$ and using integrals from [73] we obtain

$$\left\langle \frac{d\sigma}{d\Omega}(\mathbf{Q}) \right\rangle_{\text{chao}} = \frac{q_f}{q_i} \frac{d\sigma^{\text{el}}}{d\Omega} \sum'_{l_1, l_2} I_{l_1}\left(\frac{1}{2}L_1^2\right) I_{l_2}\left(\frac{1}{2}L_2^2\right) e^{-\frac{1}{2}[L_1^2 + L_2^2]} e^{-il_1\tau_1} e^{-il_2\tau_2}. \quad (4.68)$$

Here I_l is the Bessel function with imaginary argument. It is interesting to compare (4.67) and (4.68): when the field states are coherent states, the cross-section exhibits a strong phase dependence which is absent in the case of chaotic field states. This is understood by noting that $P(\alpha)$ of the chaotic state only depends on the modulus of α and bears no phase correlations. In real two-colour experiments, one typically uses a pulsed laser, which is passed through a non-linear medium generating the second or third harmonic. The relative phase between the harmonic and the ordinary field is controlled by propagation through a dissipative medium [30]. The resulting two colours are clearly phase and amplitude correlated. In the case of a strong coherent pump field, we expect

two coherent fields after the harmonic generation and the result in (4.67) still holds. If the pump field is not coherent but e.g. chaotic, it is not clear how the statistics of the resulting fields will be. The joint P -representation will depend on the propagation in the non-linear crystal. To gain more insight into the problem of photon correlations in non-coherent field states, we have to abandon the description of the harmonic generation as a “black box event” and instead solve the Maxwell equations leading to a knowledge of α_1 and α_2 as a function of the actual incident field state. Our results show that phase dependence in two-colour experiments is very sensitive to the field statistics.

Equation (4.67) can be simplified if the two laser field frequencies are commensurable. In the case of the fundamental and the second harmonic, e.g., we introduce a new index $l = l_1 + 2l_2$, and the sum in (4.67) is restricted to l -values satisfying the energy relation $\frac{1}{2}q_f^2 - \frac{1}{2}q_i^2 + l\omega + 2l\omega = 0$:

$$\left\langle \frac{d\sigma}{d\Omega}(\mathbf{Q}) \right\rangle_{coh} = \frac{q_f}{q_i} \frac{d\sigma^{el}}{d\Omega} \left| \sum_{l_2=-\infty}^{\infty} J_{l-2l_2}(L_1) J_{l_2}(L_2) e^{il_2(\varphi_2 - \tau_2 - 2(\varphi_1 - \tau_1))} \right|^2. \quad (4.69)$$

Note, that the harmonic order enters the phase $\varphi_2 - \tau_2 - 2(\varphi_1 - \tau_1)$. This is a signature of the energy difference between the second harmonic and the fundamental frequency. We note the sum rule $\sum_l \left\langle \frac{d\sigma}{d\Omega}(\mathbf{Q}) \right\rangle_{coh} = \frac{d\sigma^{el}}{d\Omega}$ which is of relevance contemplating an experimental verification of the present theory. In chapter 6, we present results based on a generalization of equation (4.69) taking momentum transfers to target atoms into account.

It has been demonstrated that the one-colour cross-section data [82, 83] in non-critical geometries are located between the theoretical data for a coherent monochromatic laser field and a chaotic field [43]. This is not surprising since a multimode laser was employed. In two-colour free-free experiments we, therefore, expect results for the cross-sections that display phase dependencies, neither as strong as indicated in (4.67) or (4.69) nor totally absent as in (4.68).

To summarize, we have shown that the nature of the field has a very dramatic effect on the interference terms. Maximum signature of interference in two-colour experiments is presence when the two light beams are coherent. Interference terms gain decreasing weight when the light beams loose phase correlation. Interference is absent in the case of two independent chaotic beams, as well as in the case of some correlation between a chaotic light beam and, e.g., its second harmonic. Interference effects are totally absent in the extreme quantum mechanical number state limit. Intense lasers are nearly coherent and in strong field experiments the interference terms will, accordingly, have almost the maximum weight as obtained by using the semi-classical or the coherent quantum field description. This conclusion is generally expected to hold for two-colour dynamical processes, and it is in accord with experimental findings [30, 31].

Chapter V

Laser-assisted electron scattering: calculations and conclusions

5.1 Laser-assisted electron scattering on the zero-range potential

In this section, we perform a systematic comparison between exact results for laser-assisted electron scattering in the zero-range potential and corresponding results derived in the various approximations discussed in chapter 4, i.e. the impulse approximation (IA) and its peaked form (PIA) corresponding to a generalization of the Kroll-Watson theory, the weak-field soft-photon (WFSP) approximation and the zero-order soft-photon (ZOSP) approximation. The IA is readily evaluated numerically in the present case where the off-shell T -matrix is available in closed form and we find that it generally provides an accurate representation of the exact result in the range where it is supposed to be applicable, i.e. for sufficiently low laser intensities. This fact, however, does not imply that it is of less importance to study and understand the virtues and shortcomings of theories based upon alternative approximation schemes or on additional simplifying assumptions since such theories appear to be of most relevance under normal conditions where at best the on-shell scattering amplitude is readily accessible.

Figure 5.1 shows differential cross-sections (DCS) in the classically forbidden region ($|l| > L$) in the one-photon absorption channel for scattering of 10 eV electrons in the zero-range potential in a circularly polarized CO₂ laser field ($\omega = 0.117$ eV) at an intensity of 2×10^8 W cm⁻² as a function of the angle, θ_i , of the incident electron with respect to the laser beam. In the upper panel, the electron momentum transfer, \mathbf{Q} , is arranged to be exactly parallel to the laser propagation direction. Accordingly, the exchange of photons is classically strictly forbidden ($L = 0$). The geometry has been slightly changed in the lower panel: the laser beam is still confined to the electron scattering plane, but now the electron scattering angle is set to be bisected by the laser polarization plane $\theta_f = 180^\circ - \theta_i$. This implies that L is non-vanishing, but the exchange of photons is still classically forbidden since L remains much smaller than one.

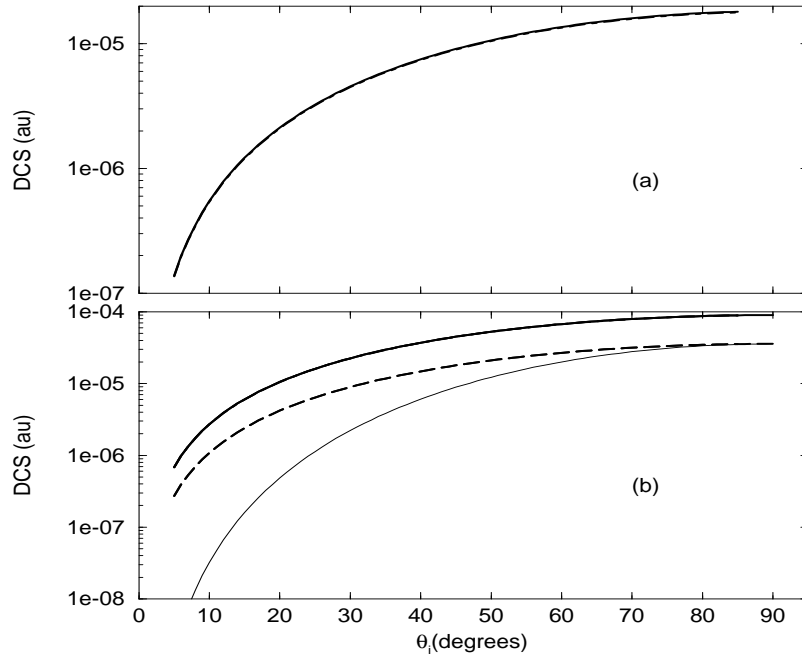


Figure 5.1: Differential cross-section for zero-range potential scattering of 10 eV electrons in the one-photon absorption channel versus the angle, θ_i , made by the incoming electron with respect to the circularly polarized laser beam. The laser beam is confined to the scattering plane: (a) \mathbf{Q} is parallel to the laser propagation direction and (b) the final electron momentum direction is $\theta_f = 180^\circ - \theta_i$. The intensity of the CO₂ laser ($\omega = 0.117$ eV) is 2×10^8 W cm⁻². The full curve represents the WFSP approximation while the dotted-dashed curve represents the indistinguishable results of the exact form [55] and the IA. In the lower panel, the dashed curve is the ZOSP approximation while the thin curve is the PIA with complex displacements.

Different curves in the figure correspond to different theoretical approximations as detailed in the caption. Both panels show that the WFSP approximation of equation (4.15) (or (4.47)) as well as the IA of equation (4.2) are in very good agreement with the exact result of equation (4.54). On the scale of the figure, the difference can hardly be resolved. The relative difference between the WFSP theory and the exact result is in fact less than $\sim 1\%$ over the entire range of the two panels.

The standard PIA is not defined in the classically forbidden region. As discussed in section 4.1, it is formally possible to make an analytical continuation of the PIA into the classically forbidden region by letting the displacement vectors

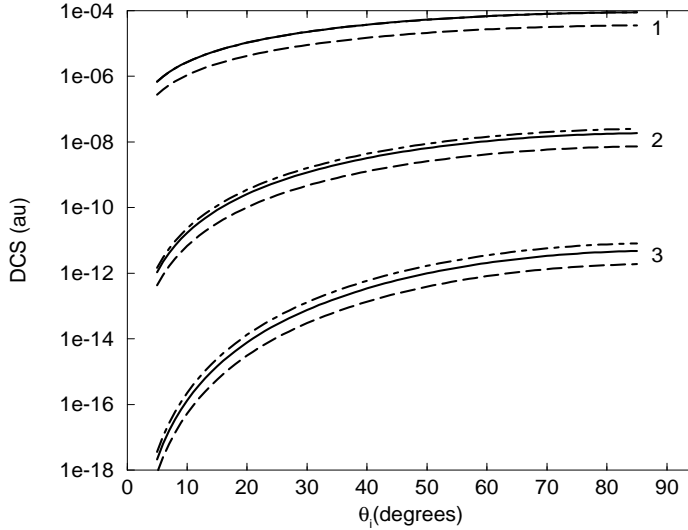


Figure 5.2: As figure 5.1(b), except that the study has been extended to include two- and three-photon exchange processes. Integers denote the number of exchanged photons. The full, dashed and dotted-dashed curves represent the WFSP approximation, the ZOSP approximation and the exact form, respectively. The IA cannot be distinguished from the exact result.

become complex. This approximation is nevertheless ill-defined in the upper panel since γ_{\pm} tends to infinity due to the orthogonality of \mathbf{Q} with respect to the polarization plane. The displacement vectors are finite in the experimental situation exhibited in the lower panel of figure 5.1. Except for small scattering angles ($\theta_i \sim 90^\circ$), however, the displacements are so large, $\gamma_{\pm} \gtrsim q_i$, that the PIA is meaningless. The corresponding cross-section is indeed off by orders of magnitude. As $\theta_i \rightarrow 90^\circ$, the PIA approaches the ZOSP approximation since $|\mathbf{q}_i + \boldsymbol{\gamma}_{\pm}| \rightarrow q_i$. The ZOSP approximation of equation (4.19) is generally well defined, but predicts a zero value ($J_l(0) = \delta_{l,0}$) when \mathbf{Q} is parallel to the laser propagation direction as in the upper panel. In the lower panel, the ZOSP approximation is off by a factor of ~ 2.5 .

Figure 5.2 shows results in the same bisecting geometry as the one corresponding to figure 5.1(b). Again laser-assisted scattering is classically forbidden and the PIA provides a very poor representation of the cross-section and is therefore not shown. The IA is, on the other hand, essentially indistinguishable from the results of the exact form. As indicated by the integers in the figure, the study includes two- and three-photon exchange processes (absorption and emission channels are indistinguishable on the scale of the figure). The ZOSP approx-

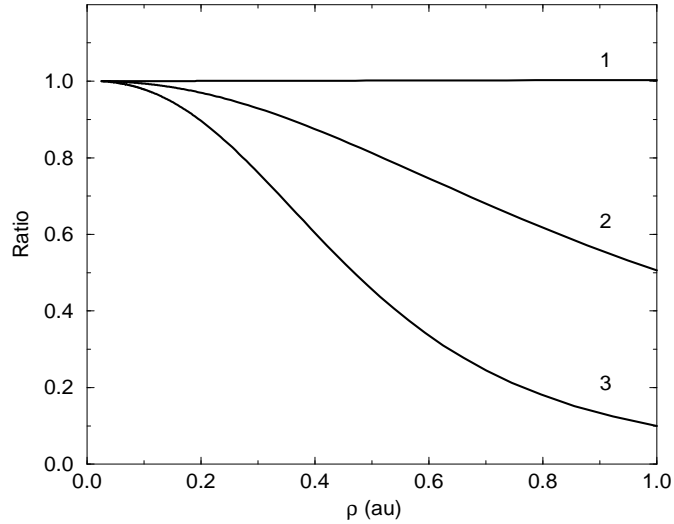


Figure 5.3: The ratio of the WFSP cross-section to the exact result in the classically forbidden region for laser-assisted zero-range potential scattering of 10 eV electrons. The electron scattering angle is kept fixed at 50° while the direction of the circularly polarized laser is varied in the electron scattering plane to scan a suitable range of the order parameter, ρ . The photon energy is 0.117 eV and the laser intensity is $2 \times 10^8 \text{ W cm}^{-2}$. Integers denote the number of absorbed photons.

imation is off by factors of ~ 2.5 , 3.5 and 4.3 for one, two and three photon processes, respectively. Similarly, as expected for a theory based on first order perturbation theory, the accuracy of the WFSP approximation is gradually reduced as the number of exchanged photons is increased. To account accurately for n -photon processes, it is anticipated that the WFSP theory must be extended to n 'th order in the electron-field interaction in the intermediate propagation between the asymptotic Volkov states [44]. This aspect of the WFSP theory is illustrated by figure 5.3. As noted in section 4.1.4, the order parameter in the expansion of the elastic off-shell T -matrix element in (4.14) – or equivalently in the expansion of the transition operator in (4.37) – is given by A_0 . However, in the classically forbidden geometry corresponding to $|l| > L$, the effective order parameter appears in the combination $\rho = A_0/L$ (see section 4.1.4). Figure 5.3 shows the ratio between the WFSP approximation and the exact theory in one, two and three photon absorption channels. The intersection angle between the laser beam and \mathbf{Q} is varied to scan the classically forbidden region $0 \leq L \lesssim |l|$ while keeping A_0 fixed at a value that is low enough to ensure that the weak-field expansion is valid in the classically allowed region. The

figure clearly shows that the extension of the WFSP approximation into the classically forbidden region describes one-photon exchange scattering precisely, whereas two- and three-photon exchange can only be described into classically forbidden regions provided $\rho \ll 1$.

In non-critical geometries corresponding to classically allowed regions ($|l| \leq L$), the strength of A_0 is expected to determine the adequacy of the WFSP approximation. This is confirmed by figures 5.4 and 5.5, which represent the ratio between model differential cross-sections and the exact result as a function of the order parameter, $A_0 = \sqrt{I}/\omega$, in case of scattering of 10 eV electrons on the zero-range potential in the one photon absorption channel. The results are qualitatively the same in other photon-exchange channels. The range of A_0 values in figures 5.4 and 5.5 corresponds to L values between 1 and 22. In figure 5.4, the laser frequency is kept fixed at $\omega = 1$ eV. Hence, in this representation, A_0 is proportional to the square root of intensity. The maximum field strength in the figure is $F_0 = \omega A_0 \simeq 0.02 \ll 1$. In figure 5.5, A_0 is varied by decreasing the laser frequency from $\omega \sim 5$ eV to $\omega \sim 1$ eV by keeping the laser intensity fixed at 2×10^{13} W cm⁻². Accordingly, A_0 is inversely proportional to the laser frequency in this figure while the field strength is constant, $F_0 = \sqrt{I} \simeq 0.02$. It should be noted that the differential cross-sections, from which the ratio in the two figures is derived, oscillate as a function of A_0 . These oscillations reflect the oscillatory behaviour of the Bessel function as the argument is increased and result in some structure in the ratio curves, particularly in the vicinity of the minima in the cross-sections since these minima are not perfectly aligned. The symbols in figures 5.4 and 5.5 represent the ratio at the maxima in the oscillatory behaviour of the cross-section. The lines in the figures represent the qualitative trend of the ratio, but, for simplicity, we have ignored resonance-like structures due to the misalignment of the minima in the considered cross-sections.

As demonstrated by figures 5.4 and 5.5 the WFSP theory is very accurate in the weak-field regime. As one would expect, the discrepancy between the WFSP approximation and the exact result increases with increasing A_0 . The same is true for the ZOSP approximation, which is generally less accurate than the WFSP approximation. The behaviour of the generalized KW approximation, i.e. the PIA, is markedly different, and it is clear that the vector potential amplitude is not an appropriate order parameter for the PIA. In fact, it appears from these figures that the small values of $F_0 = \omega A_0$, as anticipated, control the accuracy of the IA. For the low A_0 -values in figure 5.5, the laser frequency is as high as $\omega \simeq 5$ eV. The low-frequency approximation is consequently poorly fulfilled. The good agreement between the exact result and the PIA in this regime is possibly associated with the fact that the zero-range potential is independent of off-energy-shell effects [54].

As an alternative way of increasing A_0 , we may keep the quiver radius $\alpha_0 = A_0/(\sqrt{2}\omega)$ fixed while increasing ω . This is done in figure 5.6, which shows differential cross-sections as a function of A_0 in the two-photon absorption channel. The non-critical scattering conditions ($4.8 \leq L \leq 6.0$) are detailed in the caption. The constant value of $\alpha_0 \simeq 2.88$ au corresponds to a circularly polar-

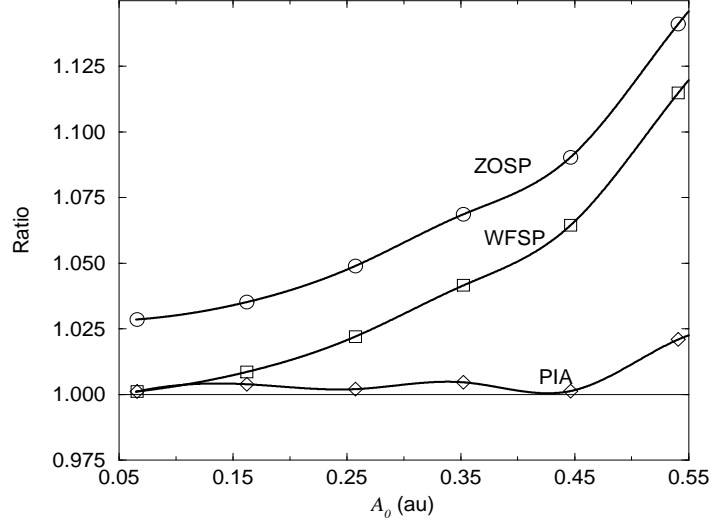


Figure 5.4: The ratio of the ZOSP (circles), the WFSP (squares) and the PIA (diamonds) one-photon absorption cross-sections to the exact result in the classically allowed region as a function of the vector potential amplitude A_0 . The scattering angle is fixed at 160° in a geometry with the scattering plane perpendicular to the laser propagation direction ($\Delta\phi = 160^\circ, \theta_i = \theta_f = 90^\circ$). The energy of the laser photons is 1 eV and A_0 is increased by increasing the intensity starting from $\sim 1.2 \times 10^{11} \text{ W cm}^{-2}$ at $A_0 = 0.05$. At $A_0 = 0.55$ the laser intensity is $1.4 \times 10^{13} \text{ W cm}^{-2}$. The electric field amplitude is $F_0 = \omega A_0 = 0.02$ at the highest intensity.

ized CO₂ laser field operating at an intensity of $2 \times 10^8 \text{ W cm}^{-2}$. In figure 5.6 the highest value of A_0 is obtained by considering a laser with photon energy $\omega = 13.4 \text{ eV}$ and intensity $\sim 3.4 \times 10^{16} \text{ W cm}^{-2}$. The figure indicates that the deviation between the exact result and the models to a large extent may be explained by the presence of *laser-induced* resonances in the exact treatment [55]. These are not accounted for in any of the approximate treatments. Resonances are introduced when n photons are emitted in the intermediate propagation to make the energy of the electron virtually degenerate with the bound state. This happens at frequencies determined by

$$\omega = \frac{1}{n} (\kappa^2/2 + q_i^2/2), \quad (5.1)$$

if frequency-dependent self-energy (AC Stark) shifts are ignored. Hence, an infinite series of resonances is in principle present. In figure 5.6 the positions of the resonances as calculated from equation (5.1) are marked on the A_0 -axis.

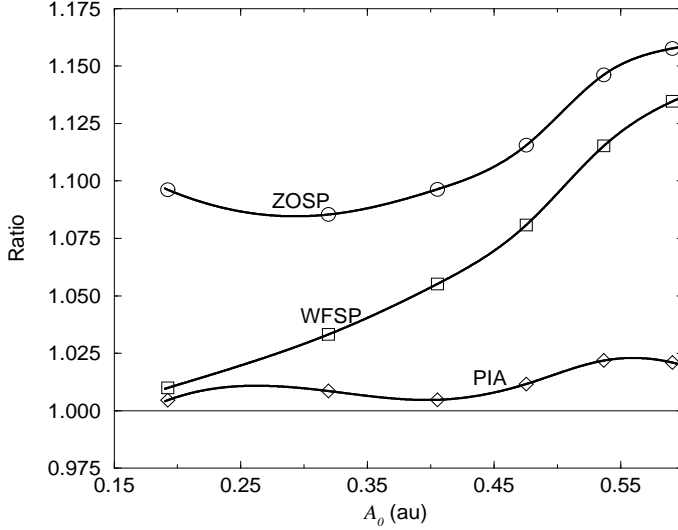


Figure 5.5: As figure 5.4, except that the intensity of the light is kept fixed at $2 \times 10^{13} \text{ W cm}^{-2}$ while A_0 is increased by decreasing the photon energy from 5 eV to 1 eV. The corresponding value of the field amplitude, F_0 , is 0.02 independently of the laser frequency.

The arrows correspond to a range of n -values from $n = 6$ at $A_0 \simeq 0.5$ to $n = 2$ at $A_0 \simeq 0.15$. Interestingly, the exchange of more than 5 photons is classically forbidden since $L \leq 5$ in the range below $A_0 \sim 0.5$, where these resonances are supposed to appear. Clearly the $n = 2$ and $n = 3$ photon resonances are at the positions predicted by equation (5.1). This is not the case for higher-order resonances. The shift and shape of these resonances might be an indication of a pronounced overlap between the resonances as the resonance spacing decreases [84].

Consistently with our experience from figures 5.4 and 5.5, the WFSP theory converges towards the exact theory in the weak-field region. At $A_0 \simeq 0.15$, for example, the relative difference between the exact result and the WFSP approximation is $\sim 1.9\%$. At $A_0 \simeq 0.35$ the relative difference has increased to $\sim 2.1\%$, but there is still no resonance signature. For comparison, the relative differences between the PIA and the exact result at these A_0 -values are $\sim 1.3\%$ and $\sim 5\%$, respectively. The differential cross-section is strongly influenced by resonances for larger values of the order parameter, but it appears that the WFSP cross-section represents the background quite accurately even at fairly large values of A_0 . This is, however, somewhat fortuitous since we have found cases for other photon exchange channels and for other electron energies where

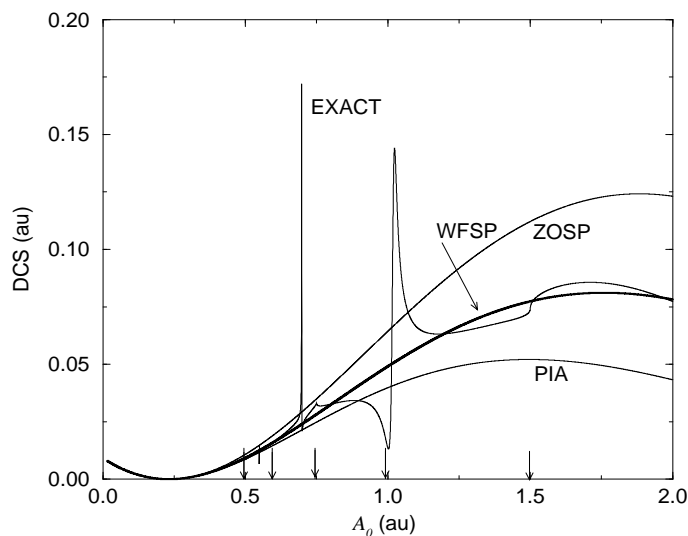


Figure 5.6: Differential cross-sections in the two-photon absorption channel at a scattering angle of 160° in a plane including the circularly polarized laser beam ($\Delta\phi = 180^\circ, \theta_i = 90^\circ, \theta_f = 110^\circ$) as functions of the vector potential amplitude, A_0 . The quiver radius is kept fixed at $\alpha_0 = 2.88$, corresponding to an intensity of $2 \times 10^8 \text{ W cm}^{-2}$ for 0.117 eV photons. Locations of resonances as calculated by equation (5.1) for $n = 6$ to $n = 2$ are marked by arrows.

the background is better represented by the PIA.

5.2 Non-resonant electron scattering on argon

Free-free transitions are usually studied in low-energy electron scattering. Then the scattering amplitude used in the on-shell approximation of the WFSP approximation may be represented by a few terms in the partial wave expansion

$$f_q(\theta) = \frac{1}{2iq} \sum_{\lambda=0}^{\infty} (2\lambda + 1) [e^{2i\delta_\lambda(q)} - 1] P_\lambda(\cos\theta). \quad (5.2)$$

For the $e + Ar$ case, the phase shifts, $\delta_\lambda(q)$, may be taken from [85]. These phase shifts give values for the field-free elastic scattering cross-section in good agreement with the experimental results [86].

Differential cross-sections for free-free transitions with $l = \pm 1$ and $l = \pm 2$ in $e + Ar$ scattering at 10 eV, $I = 10^8 \text{ W cm}^{-2}$ and $\omega = 0.117 \text{ eV}$ (CO_2 laser) are

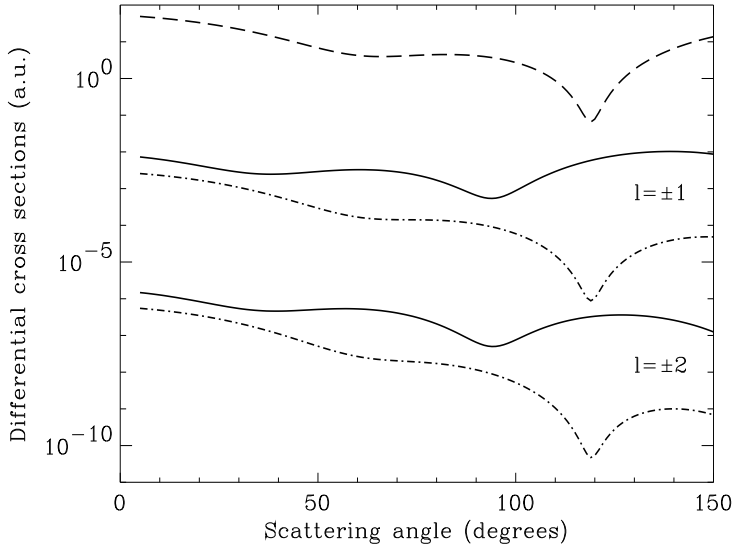


Figure 5.7: Differential cross-sections versus scattering angle for 10 eV electrons on argon in a geometry where ϵ bisects the electron scattering angle. The field-free elastic cross-section is represented by the broken curve. Photon-assisted cross-sections ($\omega = 0.117$ eV, $I = 10^8$ W cm $^{-2}$) are represented by full curves in the WFSP theory and by dotted-dashed curves in the ZOSP approximation.

presented in figure 5.7 in the WFSP approximation as well as in the ZOSP approximation. Throughout this section, the laser is linearly polarized. The scattering geometry is chosen to correspond to the critical experimental arrangement of Wallbank and Holmes [26, 27]. Specifically, the linear polarization vector of the laser field, ϵ , bisects the electron scattering angle [27]. The maximum in the classically allowed number of exchanged photons is much smaller than unity: $0.0025 < L < 0.008$, making photon exchange classically forbidden. The projection of \mathbf{Q} on ϵ is non-vanishing in this geometry only because $q_f \neq q_i$ for $l \neq 0$. This in turn allows for a small but non-vanishing value of the factor $J_l^2(L)$ that determines the relative cross-section in the ZOSP approximation, but gives rise to a prohibitively large value of the KW displacement vector of equation (4.11). The KW momentum displacement is, in fact, larger than the incident electron momentum itself. The WFSP approximation, on the other hand, is well defined for $l = \pm 1$ irrespective of the value of the KW displacement. The condition (4.51) for the applicability of the WFSP theory for multiphoton processes is, however, not well fulfilled. The WFSP results in figure 5.7 for $l = \pm 2$ should, accordingly, be considered with some reservation. It is seen from figure 5.7 that the one-photon assisted cross-section is one to four orders of magnitude

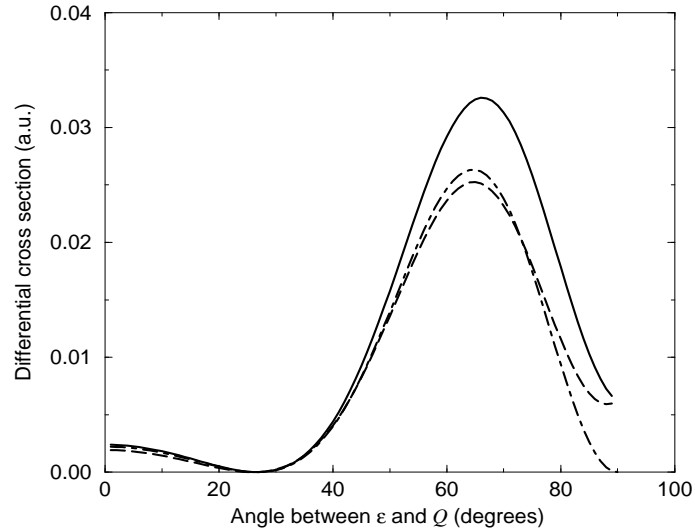


Figure 5.8: Single-photon assisted differential cross-section ($\omega = 0.117$ eV, $I = 10^8$ W cm $^{-2}$) as a function of the angle β between ϵ and \mathbf{Q} for 10 eV electrons on argon. The scattering angle is kept fixed at 120° . Full and broken curves represent the WFSP theory for absorption and emission, respectively. The dotted-dashed curve is the ZOSP result.

below the field-free cross-section and that the two-photon process is reduced by another few orders of magnitude. The figure clearly shows that the zero-order approximation is absolutely useless under the considered critical conditions. It also shows that the laser-assisted differential cross-section may reveal structures not apparent in the field-free elastic cross-section. The differential cross-sections for absorption and emission are essentially identical in figure 5.7 due to a simple symmetry property in the considered scattering geometry. When this symmetry is broken, however, there is a pronounced distinction between photo-absorption and photo-emission, as illustrated by the one-photon assisted cross-sections in figure 5.8. In this figure, the electron scattering angle is fixed at $\theta = 120^\circ$ while the angle β between ϵ and \mathbf{Q} is varied corresponding to a rotation of the laser beam relative to the electron scattering arrangement. Consistent with the results in figure 5.7, the curves for absorption and emission merge at $\beta = 90^\circ$, but a pronounced deviation between emission and absorption is apparent when β is reduced. At $\beta = 80^\circ$ absorption is about 50% more efficient than emission in the considered case with a scattering angle of 120° . The effect is strong enough to propose an experimental test. It should be noted, however, that the sign and magnitude of the deviation is a sensitive probe of the energy variation of

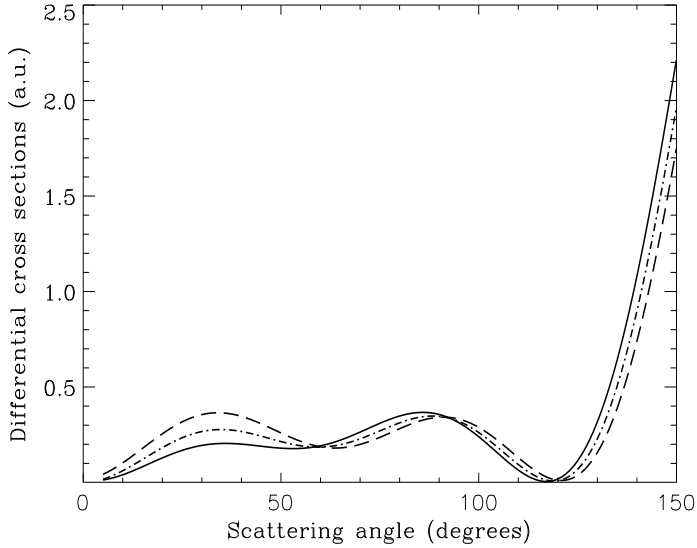


Figure 5.9: Single-photon assisted differential cross-sections ($\omega = 0.117$ eV, $I = 10^8$ W cm $^{-2}$) versus scattering angle for 10 eV electrons on argon in a geometry where the angle β between ϵ and \mathbf{Q} is 80° . Full and broken curves represent the WFSP theory for absorption and emission, respectively. The dotted-dashed curve is the ZOSP result. In the figure $L \sim |\mathbf{Q}|$, i.e. the classically allowed region is for $\theta > 71.4^\circ$.

the elastic scattering amplitude including variations in its phase. The effect is therefore expected to be system specific and to vary with electron scattering angle. The proximity of the WFSP and the ZOSP approximation for emission is fortuitous. In the figure $L \sim 8.8 \cos \beta$, i.e. the classically allowed region for one photon absorption terminates at $\beta \sim 83^\circ$. The difference between the WFSP and the ZOSP approximation persists in the classically allowed region because the field-free cross-section varies very abruptly in the region around $\theta \simeq 120^\circ$, as seen from figure 5.7. The gradient terms of the WFSP amplitude therefore make essential contributions not accounted for in the ZOSP approximation.

The variation with electron scattering angle for fixed angle between \mathbf{Q} and ϵ , $\beta = 80^\circ$, is illustrated in figure 5.9. It is seen that the ratio between absorption and emission cross-sections varies strongly with electron scattering angle. Absorption is, for example, about a factor of two more efficient than emission at $\theta \sim 120^\circ$ and vice versa at $\theta \sim 30^\circ$. It is noted that the mean value of absorption and emission apparently is well represented by the ZOSP approximation.

The relative laser-assisted signal corresponding to the WFSP results in figure 5.7 is compared with experimental data by Wallbank and Holmes for $l = \pm 1$ in figure 5.10. While the relative signal is so small in the ZOSP approximation

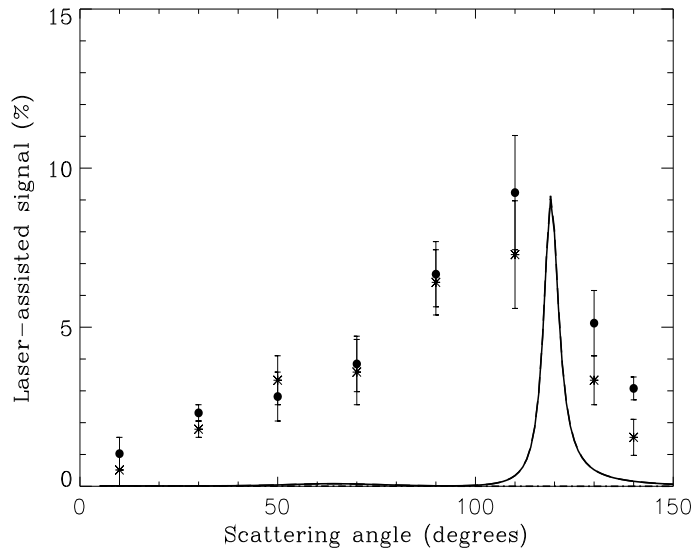


Figure 5.10: The relative laser-assisted one-photon free-free signal expressed as percentage of the field-free elastic scattering signal for 10 eV electrons on argon. The full curve represents the WFSP theory. The ZOSP approximation is hardly visible above the baseline. The experimental data are from [27]. The dots represent data from the first microsecond of the applied CO₂ laser pulse while the crosses are from the second microsecond. The theoretical curves are calculated at an intensity of 10^8 W cm^{-2} .

that it is invisible on the linear scale of the figure, it is seen that the WFSP theory predicts a pronounced peak for scattering angles around 120° . The shape of the peak is readily traced to reflect the pronounced dip in the field-free cross-section as shown in figure 5.7. The position of the peak is in good accord with the experimental results. The peak is, however, much narrower than the corresponding structure in the data. In this connection, we have noted that the experiments are performed with a rather poor collimation of the incident electron beam and with a wide acceptance angle of scattered electrons. Wallbank and Holmes [26, 27] do not specify the corresponding uncertainties in the angular definitions except that the angular resolution of the electron detector is 2° . There are, however, other important contributions to the angular uncertainties. In particular, it appears that the extent of the collision region might provide another few degrees of uncertainty in the definition of the exit angle. The divergence of the incident beam is unknown to us, but clearly not negligible either. In an earlier publication on experiments with a similar piece of apparatus, Weingartshofer and co-workers [4] quote that the total uncertainty in the experimental scattering angle is 8° . Since the laser-assisted signal is particu-

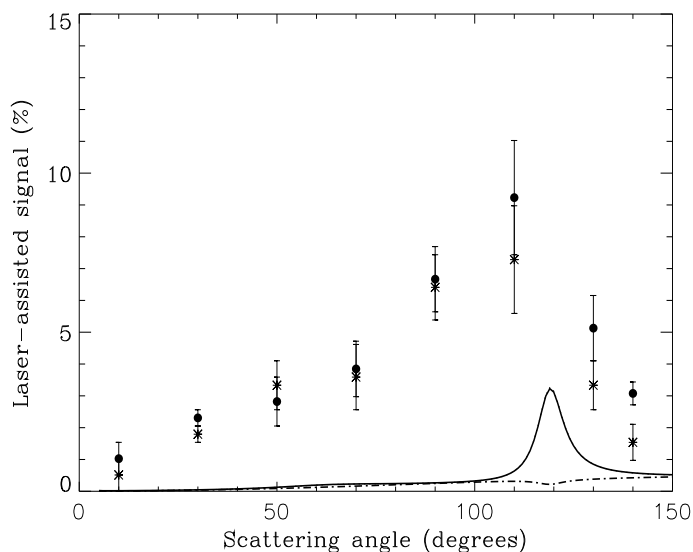


Figure 5.11: Similar to figure 5.10, except that the theory has been averaged over angular distributions with a width of 4° .

larly sensitive to variations in the scattering geometry under the experimental conditions reported by Wallbank and Holmes, we have performed an average of the relevant cross-sections over uniform angular distributions of incoming and scattered electrons corresponding to uncertainties of $\pm 4^\circ$. The resulting relative signal is shown in figure 5.11. Note that the ZOSP approximation result is now visible though still orders of magnitude too small compared to the data. As a result of the angular spread, the peak in the cross-section has broadened as expected, but the disagreement between theory and experiment clearly remains. To further examine the effect of the angular resolution, we have computed the relative signal for a sequence of values for the width. When the angular width arbitrarily is increased to around 20° , the data is matched quite well in the region below the peak at 120° , but the theory then overshoots the data points above the peak as shown in figure 5.12. Although the angular uncertainty may depend upon the electron scattering angle, for example because of a variation in width of the target zone as seen from the detector, it does not appear reasonable to attempt modelling the experimental conditions of Wallbank and Holmes in finer details at the present stage. We consider that it suffices to reproduce the pronounced structure in the experimental data and to trace a possible cause of the remaining differences. The structures in the data of Wallbank and Holmes [26, 27] at other electron energies are reproduced in a similar fashion.

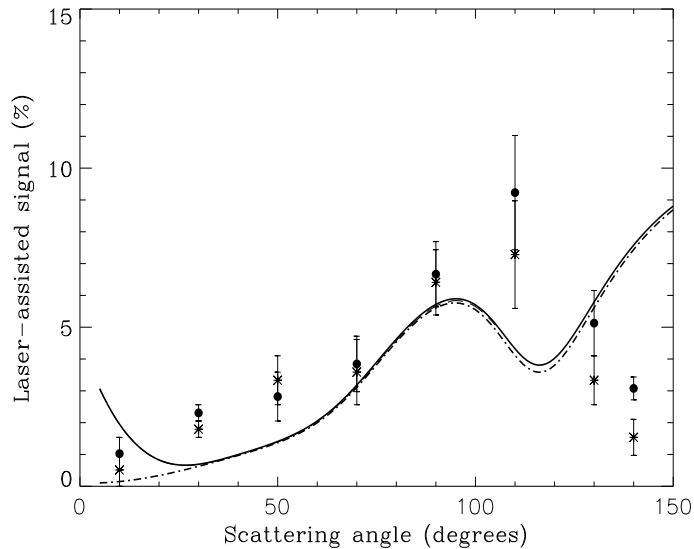


Figure 5.12: Similar to figure 5.11, except that the theory has been averaged over angular distributions corresponding to a width of 20° .

The application of the present theory for $|l| \geq 2$ is questionable under the geometrical conditions of the experiments of Wallbank and Holmes since $\rho \sim 1$ and the condition of equation (4.51) therefore is violated (see also figure 5.3 and the accompanying discussion). The experimental results for two and three photon processes are indeed found to be orders of magnitude larger than what would be predicted by the present WFSP theory. According to equation (4.50), however, we generally expect that a theory that includes sufficient orders of perturbation theory should be composed of terms $\propto L^{|l|-n}(A_0)^n$ and accordingly be dominated by a term $\propto A_0^{|l|}$ for sufficiently small L -values. Thus, under the experimental conditions of Wallbank and Holmes, on general grounds, but in apparent conflict with the data, we expect, the relative laser-assisted signal to decrease rapidly with photon multiplicity. We therefore consider that a broad angular distribution is needed in order to explain the multiphoton data by Wallbank and Holmes.

In conclusion, the pronounced structure in the experimental results of Wallbank and Holmes is qualitatively reproduced by the WFSP theory and explained on physical grounds. We have found that the theory is extremely sensitive to variations in the parameters that determine the electron-scattering geometry with respect to the polarization vector of the laser field. In fact, it is indicative that a full account of the data may have to rely upon a careful determination

of the angular-resolution profile of the experimental arrangement.

5.3 Resonant electron scattering on argon

5.3.1 Well-separated resonance series

In this section, we use the resonant weak-field soft-photon theory of section 4.3 for studying resonant scattering in argon in a linearly polarized laser field. We consider, as a case study, scattering near the $(3p^5 4s^2)^2P_{3/2}$ and $^2P_{1/2}$ resonances positioned at $\epsilon_1^r = 11.10$ eV and $\epsilon_2^r = 11.27$ eV [87]. The widths of the lines are not accurately known. For simplicity, we follow [62] and take $\Gamma_1 = \Gamma_2 = 2.1$ meV (see also [87]). We calculate elastic scattering amplitudes by an expansion in partial waves denoted by λ ($\lambda = 0, 1, 2, \dots$) and use phase-shifts from [62] for $\lambda \leq 3$, while the contribution from higher partial waves is calculated using the Born expression [88] with a polarizability of 11.0 au for argon. The photon field is assumed to be generated by a linearly polarized CO₂ laser operated at intensities 10^7 - 10^9 W cm⁻² and, consistent with the assumptions of the WFSP theory, the attention is focused on single-photon exchange processes. We consider classically forbidden scattering in the critical geometry. In practice, we let the laser polarization vector, ϵ , bisect the electron scattering angle. Although this is only treated in detail in section 5.3.2, we mention, that there is a marked difference between absorption and emission processes. Figures 5.13 and 5.14 present cross-sections for one-photon absorption ($l = -1$) in electron-argon scattering through 20° and 120°, respectively, at a laser intensity of 10^7 W cm⁻². Figure 5.13 presents the WFSP theory (full curve) as well as the ZOSP approximation (broken curve). Corresponding background contributions are represented by essentially horizontal lines. The peaks at 11.10 eV and 11.27 eV will be referred to as *principal lines* since they appear at the positions of the resonances in the field-free cross-section (full curve in the upper part of the figure). The assisting photon ($l = -1$) of the principal lines is accordingly absorbed after the scattering event. The peaks at 10.98 eV and 11.15 eV correspond to the principal lines, but represent a situation where the photon is absorbed before the atomic collision. Hence, we refer to these as *time reversed principal lines*. The peaks at 11.22 eV and 11.39 eV correspond to a process where the electron first emits a photon to the field, scatters at the $^2P_{3/2}$ and $^2P_{1/2}$ resonances, respectively, and subsequently absorbs two photons from the field. Lines as these, involving a number of virtual photons, shall be referred to as laser-induced side resonances. The principal lines as well as their time-reversed counterparts are essentially the same in the WFSP and ZOSP approximations although a clear difference in background contribution is present when exhibited on the logarithmic scale of figure 5.13. On a linear scale, however, the two theories would be indistinguishable and the central resonances accurately represented by pure Lorentzians. This is consistent with Bader [62], who concludes that “the shape of the resonance structures are as predicted by the soft-photon approximation”. The laser-induced side resonances, on the other hand, are so much weaker at

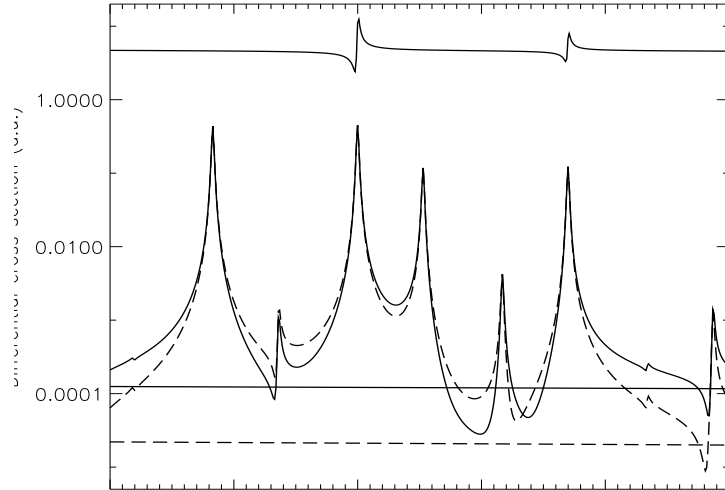


Figure 5.13: Differential cross-section for laser-assisted electron-argon scattering in the one photon absorption channel at a scattering angle of 20° as a function of the incident electron energy. The intensity of the linearly polarized CO_2 laser is 10^7 W cm^{-2} . The full curve and the broken curves represent the WFSP and ZOSP approximations, respectively. Also shown are the background contributions from the non-resonant parts. The full curve in the upper part of the figure is the field-free signal. ϵ bisects the electron scattering angle ($L \ll 1$).

the laser intensity considered in figure 5.13 that they clearly exhibit the characteristics of interference with the background.

The differential cross-section for laser-assisted scattering under critical geometrical conditions in electron argon collisions at 10 eV was studied in detail in section 5.2. It was found that the ZOSP theory is particularly poor for scattering through angles around 120° . As illustrated by figure 5.14, this conclusion also holds in the present energy region where the WFSP background is a factor of $\sim 10^3$ larger than the ZOSP background. This is sufficient to modify the spectrum in a more significant way even in the region of the central resonances. The question is of course if the detailed structures exhibited on a logarithmic scale in figures 5.13 and 5.14 may be resolved on the linear scale of actual experiments.

Since experiments are facilitated by a higher count rate if the laser intensity is increased, it is interesting to study the laser-intensity dependence of the resonance spectra. Due to the very low background in the field-free cross-section at a scattering angle of 120° , it is natural to make the investigation with this particular angular choice. Figure 5.15 shows the electron scattering cross-section

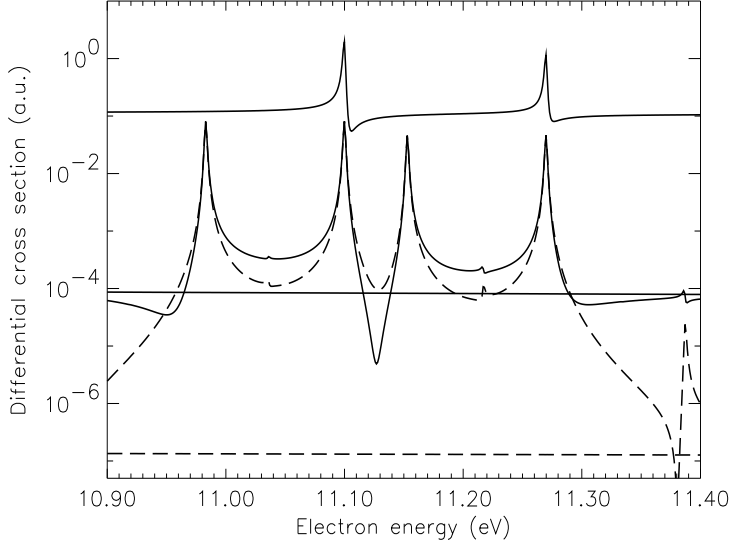


Figure 5.14: As figure 5.13, except that the electron scattering angle has been changed from 20° to 120° .

in the single-photon absorption channel for an intensity of 10^9 W cm^{-2} . Notice that the WFSP and ZOSP theories now differ so much that it clearly shows on a linear scale. The central resonances appear in pairs as in figures 5.13 and 5.14 although the small difference between q_i and q_f , when scaled by the quiver radius in the relevant Bessel function factors, is sufficient to induce a slight asymmetry between the principal lines and their time-reversed counterparts. As before, the laser-induced side lines are all interpreted in terms of virtual photon exchanges during the initial and final electron propagation. The structure at 10.92 eV belongs to the $^2P_{1/2}$ resonance and corresponds to absorption of three photons before the scattering event and subsequent re-emission of two photons. Similarly, the structure at 11.33 eV belongs to the $^2P_{3/2}$ resonance and corresponds to emission of two photons before and absorption of three photons after the scattering event. Compared with figures 5.13 and 5.14, the distribution in the different resonance channels has changed conspicuously. In fact, it is interesting to note that the intensity is high enough that laser-induced side peaks dominate over principal lines as clearly illustrated by the 10.92 eV and 11.33 eV lines representing one-photon assisted scattering with virtual exchange of two photons during the initial and final course of the scattering event. This dominance reflects the fact that the higher-order Bessel functions in equations (4.59) and (4.60) gain more weight as the argument is increased at higher laser intensities. Comparing the two theories, it is seen that the underestimation of the

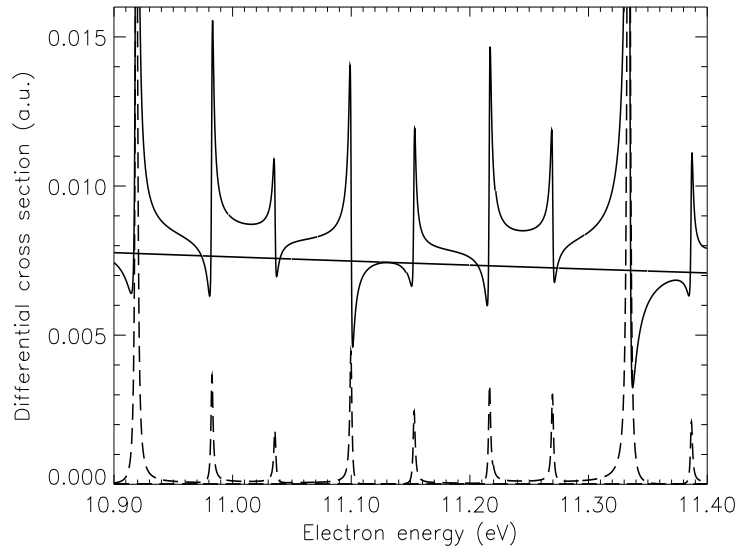


Figure 5.15: As figure 5.14, except that the laser intensity is increased to 10^9 W cm^{-2} and that the vertical scale is changed from logarithmic to linear.

background amplitude in the ZOSP approximation in this case is fatal. While the ZOSP spectrum is composed of pure Lorentzians, the WFSP approximation gives rise to characteristic interference structures even for the principal lines in the spectrum. The Jung-Taylor conjecture is accordingly not generally valid. Detailed studies of the intensity variation of the laser-assisted argon resonances have shown that a laser intensity around 10^7 W cm^{-2} is an optimal choice for the observation of nearly pure Lorentzians. This conclusion is in accord with experimental experience [63].

We have found that the background contribution depends in a very sensitive way on the geometrical arrangement. The disparity between WFSP and ZOSP results disappears as expected as one moves away from the critical geometry. High angular resolution and accurate fulfilment of single-collision conditions are therefore essential for proper experiments in this area.

5.3.2 Overlapping resonances

In the preceding section, the radiation field was assumed to be generated by a CO_2 laser. CO_2 lasers have commonly been used in low-frequency laser-assisted scattering experiments [26, 27]. In principle, however, it is possible to use tunable lasers that might scan the photon energy region around the splitting between the principal resonances pertaining to the considered target

atom. Then it becomes possible to study overlapping resonances and their interference patterns in a systematic way as illustrated below. For practical reasons, we continue to consider the $\text{Ar}^- \ ^2\text{P}_J$ resonances separated by 0.17 eV, but most of the features that we shall discuss are generic and may be adopted for a broader class of systems. In order to allow for a flexible study, we further take the liberty of varying the widths of the two lines rather freely. It should be noticed that interference effects between overlapping resonances in certain cases may be ruled out by symmetry or completeness arguments [65], but interference between fine-structure components is not precluded in this way.

Figures 5.16-5.18 present results for laser-induced resonance-interference in electron scattering in the one-photon exchange channel. The laser intensity is chosen to be 10^7 W cm^{-2} and the experimental geometry is critical so that the exchange of photons is classically strictly forbidden and such that the background amplitude, according to the discussion in section 5.3.1, may be safely ignored. Specifically, the laser polarization vector bisects the electron scattering angle. All three figures focus on the interference between the 11.10 eV $^2\text{P}_{3/2}$ principal line and lines having parentage in the 11.27 eV $^2\text{P}_{1/2}$ resonance. In the absorption channel it is the time-reversed principal line of the $^2\text{P}_{1/2}$ resonance that is involved while in the emission channel it is the corresponding laser-induced side line representing absorption of one photon before and emission of two photons after the atomic scattering event that enters.

In figure 5.16, the widths of the two lines are equal ($\Gamma_1 = \Gamma_2 = 2.1 \text{ meV}$) while the detuning, δ , of the laser with respect to the fine-structure splitting is varied. Since the differential cross-section is essentially symmetric with respect to red and blue detunings, only results with red detuning are shown. The full curves represent one-photon absorption, while the broken curves represent one-photon emission. The upper and lower panels correspond to electron scattering angles of 20° and 120° , respectively, and exhibit characteristically different interference patterns. There is also a pronounced difference when the emission and absorption channels are compared. The laser-induced side peak being involved in the emission channel is, in fact, so weak that the spectrum is totally dominated by the $^2\text{P}_{3/2}$ principal line. Even when detuned by one width unit, $\delta = 1$, there is no observable trace of the laser-induced side-peak in the emission channel in figure 5.16. The emission spectrum may therefore be viewed as a convenient standard of reference in the following discussion of the pronounced interference effect observed in the absorption channel. Comparing the absorption spectrum for zero detuning with the emission spectrum, it is seen that the interference is destructive at 20° scattering, but constructive at 120° . As discussed further below, this represents the distinctly different phase properties of the interfering amplitudes in the direct and the spin-flip scattering channels by which the scattering cross-section is composed. As the laser is detuned, the lines move apart and the interference patterns become more complicated, though still primarily destructive at 20° and constructive at 120° . As the detuning is further increased, the overlap between the lines is strongly reduced and the resonances eventually evolve into well-separated Lorentzian-shaped lines discussed in figures 5.13 and

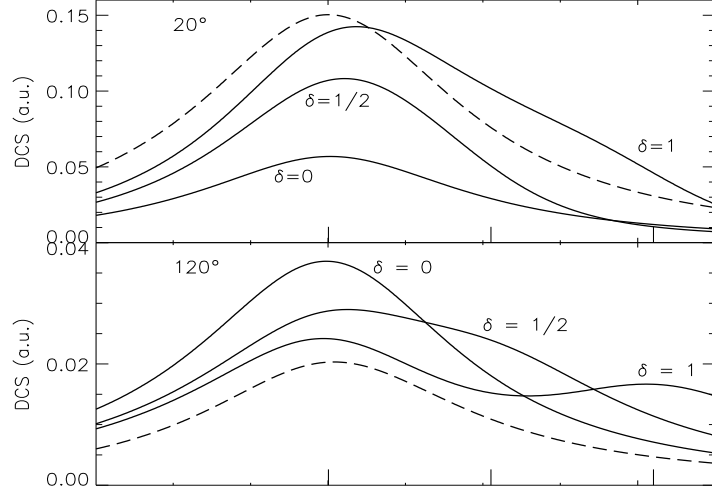


Figure 5.16: Laser-assisted differential scattering cross-section in the proximity of the argon 11.10 eV ${}^2P_{3/2}$ resonance in the one photon absorption (full curves) and the one photon emission (broken curves) channels as a function of the energy of the projectile electron for the selection of laser detunings, δ , as indicated, in width units, in the figure. The corresponding positions of the time-reversed principal lines of the ${}^2P_{1/2}$ resonance are marked on the horizontal axis. The laser intensity is 10^7 W cm^{-2} for both panels, representing scattering through 20° and 120° , respectively. The spectrum is essentially independent of detuning in the emission channel.

5.14.

The pronounced distinction in figure 5.16 between absorption and emission can be understood as follows. Considering electron energies around the principal resonance ϵ_1^r there are two essential contributions to the T -matrix in the considered geometry

$$\begin{aligned} \mathcal{T}_l^{\text{WFSP}} \simeq & J_l\left(\frac{A_0}{\omega}|\epsilon\mathbf{q}_f|\right)T_1^r(\mathbf{q}_i, \mathbf{q}_f, \epsilon_i)J_0\left(\frac{A_0}{\omega}|\epsilon\mathbf{q}_i|\right) \\ & + J_{l+1}\left(\frac{A_0}{\omega}|\epsilon\mathbf{q}_f|\right)T_2^r(\mathbf{q}_i, \mathbf{q}_f, \epsilon_i + \omega)J_1\left(\frac{A_0}{\omega}|\epsilon\mathbf{q}_i|\right). \end{aligned} \quad (5.3)$$

Here the first term represents the contribution from the central resonance, while the second term is due to the resonance ϵ_2^r , which is brought into overlap by absorption of a photon. Replacing T -matrix elements by scattering amplitudes as in (4.52) and using that $\frac{A_0}{\omega}|\epsilon\mathbf{q}_f| \simeq \frac{A_0}{\omega}|\epsilon\mathbf{q}_i| (\equiv x)$ in the considered geometry,

equation (5.3) may be expressed as

$$f_l \simeq J_l(x)J_0(x)f_1^r(\epsilon_i, \theta)[1 + \nu_l(x)\mu_l(\epsilon_i, \theta, \omega)], \quad (5.4)$$

where ν_l is a generalized contrast parameter controlled primarily by laser intensity while μ_l determines the spectral shape of the interference signal:

$$\nu_l(x) = \left| \frac{J_{l+1}(x)J_1(x)}{J_l(x)J_0(x)} \right| \quad (5.5)$$

and

$$\mu_l(\epsilon, \theta, \omega) = s_l \frac{f_2^r(\epsilon + \omega, \theta)}{f_1^r(\epsilon, \theta)}, \quad (5.6)$$

where s_l represents the sign of the function appearing in the definition of the contrast parameter,

$$s_l = \left[\frac{J_{l+1}(x)J_1(x)}{J_l(x)J_0(x)} \right] / \nu_l(x). \quad (5.7)$$

The shape function μ_l is of order unity for small detunings as discussed below. The strength of the interference signal is therefore largely controlled by the contrast parameter ν_l . For the considered choice of laser parameters, $\nu_1 \simeq 0.005$ in the case of one photon emission. Interference is accordingly strongly suppressed in this case. In the case of one photon absorption, on the other hand, $\nu_{-1} = 1$, allowing for pronounced interference effects. This explains the differences in the behaviour of the emission and absorption curves of figure 5.16 as well as in figure 5.17 discussed below¹. Note, in passing, that the overlapping resonance signal is reduced by approximately a factor of four compared with the signal corresponding to the CO₂ laser. This reduction is primarily due to the ω^{-2} dependence in the argument of the Bessel function factors in the WFSP amplitude.

More interesting spectral features are observed if the widths of the considered resonance lines differ appreciably as illustrated in figure 5.17 where, somewhat arbitrarily, we have reduced Γ_2 by a factor of five leaving all other parameters unchanged. The upper panel corresponding to 20° scattering exhibits clear examples of destructive interference of a narrow resonance on the background of a broader line. In the lower panel corresponding to 120° scattering, the interference pattern is, on the other hand, distinctly constructive. Notice that the hole-burning and peak-enhancement effects at small detunings would appear as line broadening and line narrowing, respectively, if experiments were performed with poor resolution. The interference signature is modified significantly when

¹For intense fields where the harmonic approximation to the Bessel functions may be applied, the $\nu_l(x)$ -factor simplifies to

$$\nu_l(x) = \begin{cases} |\tan^2(x - \pi/4)| & \text{if } l \text{ even} \\ 1 & \text{if } l \text{ odd.} \end{cases}$$

Hence, the laser dressing effects on interference phenomena are asymptotically equal in absorption and emission channels.

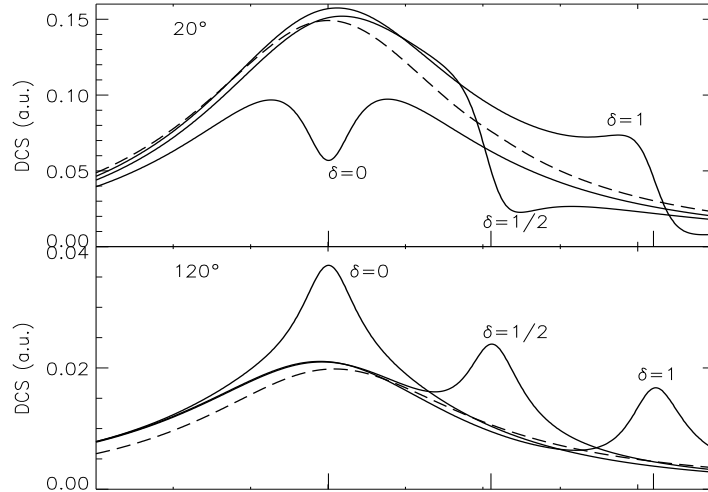


Figure 5.17: As figure 5.16, except that the resonance width Γ_2 has been reduced by a factor of five ($\Gamma_2 = \Gamma_1/5$).

the narrow resonance is scanned over the profile of the broader resonance. Particularly clear examples of asymmetric Fano-type interference signals may be found in the wings of the broader resonance at forward scattering.

In accordance with the current status of laser-assisted experiments, we have implicitly understood that the incident electron beam is unpolarized, i.e. the cross-section is the sum of direct and spin-flip contributions. The direct and spin-flip contributions in the absorption channel corresponding to the differential cross-section shown in figure 5.17 are displayed in figure 5.18 in case of a vanishing detuning, $\delta = 0$. It is clearly seen that the direct scattering amplitudes add destructively while spin-flip amplitudes add constructively at both angles. These characteristics are, as discussed below, embedded in the spectral shape functions and plainly reflect general phase properties of the two fine-structure components ($J = 3/2, 1/2$) as they are added to form the individual amplitudes corresponding to direct and spin-flip scattering. Note in this connection that the above discussion of interference signatures and contrast parameters is presumed to be applied at the level of individual amplitudes, i.e. for the direct and spin-flip amplitudes, separately. The analysis of the shape function is particularly simple in cases where only a single partial wave is involved in the scattering off the considered resonances. This simplification is applicable since the 2P_J resonances only appear in the p -wave. To be specific, we introduce the

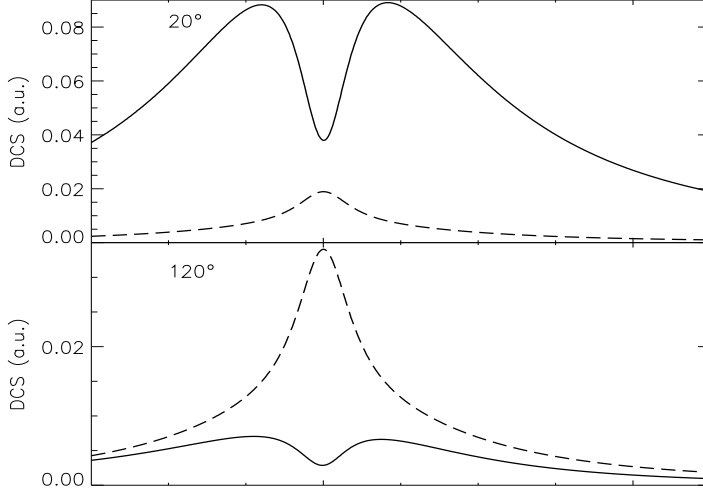


Figure 5.18: Differential cross-sections for direct (full curves) and spin-flip (broken curves) scattering at 20° and 120° in the one photon absorption channel corresponding to the zero detuning case represented in figure 5.17.

resonance phase-shifts pertaining to the interfering lines, $\eta_1^r(\epsilon)$ and $\eta_2^r(\epsilon)$ and apply standard partial-wave expansions for the direct and spin-flip amplitudes (see, e.g., [89]). In the absorption channel where $s_{-1} = -1$, we then find

$$\mu_{-1}(\epsilon_i, \omega) = -\frac{1}{2} \cdot \frac{1 - \exp[2i\eta_2^r(\epsilon_i + \omega)]}{1 - \exp[2i\eta_1^r(\epsilon_i)]} \quad (5.8)$$

in case of direct scattering, and

$$\mu_{-1}(\epsilon_i, \omega) = \frac{1 - \exp[2i\eta_2^r(\epsilon_i + \omega)]}{1 - \exp[2i\eta_1^r(\epsilon_i)]} \quad (5.9)$$

in case of spin-flip scattering.

Notice that these expressions are independent of scattering angles, a property that is due to the fact that the considered resonance scattering is restricted to one partial wave. This property clearly explains why the characteristics of the interference patterns in figure 5.18 are similar at small and large scattering angles. We also note that the expressions (5.8) and (5.9) are exactly out of phase. This property implies that direct and spin-flip channels generally exhibit complementary interference signatures. Finally, we note that the phase of the shape function in the direct scattering channel is approximately π for small

detunings, $\delta \ll \Gamma_1$, implying that the interference effect is destructive. In the spin-flip channel, on the other hand, the phase of the shape function vanishes at small detunings corresponding to a constructive effect of the interference between the two lines. The factor $\frac{1}{2}$ in the shape function of equation (5.8) is partial-wave specific and would more generally be replaced by $\lambda/(\lambda + 1)$ for the λ 'th partial wave. The presence of this factor implies that the destructive interference is incomplete in the direct scattering channel while the conditions for constructive interference in the spin-flip channel according to equation (5.9) are optimal since the contrast parameter ν_{-1} is unity in the considered case. Thus, even the magnitudes of the interference effect exhibited in figure 5.18 can be interpreted in simple terms.

It is seen from figure 5.18 that the direct amplitude is dominant at 20° scattering, whereas the spin-flip amplitude is dominant at 120° . This is consistent with the geometrical fact that the direct amplitude is dominant at forward angles for p -wave scattering, while the corresponding spin-flip amplitude is dominant for scattering angles around 90° . The destructive interference exhibited in figures 5.16 and 5.17 at 20° is accordingly a simple manifestation of the dominance of direct scattering at forward angles, while the constructive interference at 120° reflects the fact that spin-flip takes over in a broad range of scattering angles around 90° .

Chapter VI

Dispersion and quantum coherence in general and in two-colour laser-assisted electron-atom scattering in particular

The dispersion of the initial state of the probe system, be it a quantum object itself or a macroscopic system in a classical interference experiment, is in general an essential element in the analysis of quantum interference phenomena. The general situation is briefly discussed in this chapter with particular reference to generic cases in two-colour atomic-physics experiments. The effect of dispersion is, at first sight, somewhat counter-intuitive: if the probe is dispersion-free, there is no interference except in special cases, while *quantum interference* gains full weight in the *classical limit*, where the dispersion is large. We propose experiments in which a continuous transition between the two regimes may be observed [90, 91].

6.1 Introduction

The laws for probability-amplitude combination are basic ingredients in the analysis of quantum interference phenomena. The lesson usually taught may be formulated as follows [92]: To obtain the total probability for a given process, it is not what is actually measured, but what *in principle* could be measured that dictates whether competing amplitudes are coherently or incoherently added. Addition of amplitudes introduces phase-dependent interference terms, while addition of corresponding probabilities reflects the statistical distribution in various distinguishable channels. We focus on physical situations where a clear distinction between these two cases becomes ambiguous. We shall discuss the theory covering the full range from coherence to non-coherence and propose an experiment providing such delicate information as the momentum dispersion of the combined electron-atom probe in two-colour free-free experiments or of individual target atoms in two-colour multiphoton ionization processes [30, 31]. The essential point is that distinguishability of final states is controlled not

only by competing quantum paths belonging to the process, but also, due to quantum entanglement, by the initial preparation of the probe used for testing the coherence phenomenon under consideration [93].

Basically, an interference experiment consists of a coherent superposition of waves and a *probe* that registers a diffraction-type process. The probe may have macroscopic components as the double-slit in classical [94, 95] and modern [96] interference experiments or as the mirrors in Michelson interferometers and in modern quantum-marker–quantum-eraser experiments [97]. Alternatively, it may be entirely microscopic as the electron-atom probe in two-colour free-free transitions, the target atom in two-colour ionization experiments [30, 31] or the correlated trapped ions in modern Young’s type experiments [98]. Our main emphasis is on characteristics of probe systems and their signature in the contrast of interference patterns. We shall show that the contrast is governed by overlaps between final states of the probe and that these overlaps are determined essentially by the dispersion in the initial quantum state of the probe.

Without essential loss of generality, we describe the initial quantum state of the probe by a centre-of-mass wavepacket assuming the internal state to be dispersion free. We further understand that a suitable ensemble average may have to be incorporated. Such statistical effects are, however, of minor importance for the present discussion and will be ignored. Practical realizations of macroscopic probes are initially in superpositions of momentum states with distributions so broad that final states belonging to competing components of the process cannot be distinguished. This is the justification for the approach normally taken when discussing interference experiments. The other extreme is the case where also the external degrees of freedom of the probe are represented by a quantum eigenstate. The difference in probe momentum transfer corresponding to competing quantum routes can now, in principle, be measured and the interference will be lost. More generally, a partial loss of coherence could be expected as intermediate cases as thoroughly discussed by Wootters and Zurek in the context of two-slit *Gedanken* experiments [93]. While it is unrealistic to prepare the macroscopic double-slit of a classical interference fringe experiment in a sufficiently compact superposition of quantum eigenstates that the transition to the non-coherence regime may be observed, it is our conjecture that modern two-colour experiments may provide a *realistic frame* for testing such intriguing phenomena.

6.2 Theory of interference experiments

A basic postulate of quantum mechanics is that the probability of a measurement on a system described by the state, $|\Psi\rangle$ is $P = \langle\Psi|\mathcal{P}|\Psi\rangle$, where \mathcal{P} is the projection operator pertaining to the Hilbert space selected by the detection system. For notational convenience, we assume that the detection system selects a single state, $|\varphi\rangle$, and write $\mathcal{P} = |\varphi\rangle\langle\varphi|$. Accordingly, we can express the detection probability as $P = \langle\Psi_f|\Psi_f\rangle$, where $|\Psi_f\rangle = \mathcal{P}|\Psi\rangle$ is the state consistent with the measured signal. The entangled state, $|\Psi_f\rangle$, may be expressed

in terms of a restricted summation corresponding to the various paths leading to the detected state, $|\Psi_f\rangle = \sum_n' c_n |\Phi_n\rangle |\varphi\rangle$. The path-dependent probability amplitudes are represented by c_n , while the corresponding residual degrees of freedom of the system are represented by $|\Phi_n\rangle$. The detection probability may then be expressed as

$$P = \sum_{n,m}' c_m^* c_n \langle \Phi_m | \Phi_n \rangle. \quad (6.1)$$

When interference experiments are considered, the diagonal terms in equation (6.1) represent probabilities associated with individual channels while the overlaps between probe states corresponding to different quantum routes control the degree of coherence. The final states of the probe are determined by the quantum process under consideration and by *the initial preparation of the probe*. In case of classical interference experiments, it is clear that the relevant overlaps in equation (6.1) approach unity, leading to complete coherence and optimum fringe visibility. The macroscopic probes in question are plainly not initially prepared in sufficiently accurately defined quantum states that different reaction amplitudes may be resolved. This is the key to a simple understanding of classical interference experiments. Note that the Heisenberg uncertainty principle is unessential in this connection, although in special cases, such as the classical two-slit experiment discussed by Bohr and Einstein [99], interference fringes may *also* be lost due to complementarity-induced uncertainties¹.

The discussion can be made more quantitative by assuming that individual quantum paths specify a definite momentum transfer to the centre of mass of the probe, \mathbf{Q}_n . This is indeed the case in two-colour processes with microscopic probes as well as in interference fringe experiments with probes composed of macroscopic mirrors. In a Gaussian model, appropriate as a standard representation of quantum states for the external centre-of-mass motion, we may write

$$\langle \Phi_m | \Phi_n \rangle = \exp\left(-\frac{1}{8\sigma_Q^2} |\mathbf{Q}_m - \mathbf{Q}_n|^2\right), \quad (6.2)$$

illustrating generically how contributions from interference terms depend on the difference between characteristic momenta and on the character of the initial quantum state of the centre of mass of the probe, here represented by the momentum dispersion, σ_Q . When σ_Q is small, corresponding to an initial wavepacket with narrow momentum distribution, the coherence terms decrease steeply with the difference in characteristic momenta. Contrary, in the case of a broad momentum distribution, the different reaction amplitudes cannot be resolved and all coherences contribute to the sum of equation (6.1). In the

¹Bohr's application of the Heisenberg uncertainty relation rests upon the fact that the two components of the wave that scatters off the double-slit, or, equivalently, the *two coherent waves* that scatter off individual slits on the screen, are parallel. If the two components of the wave intersect at a finite angle, the question about interference or not is controlled solely by the initial momentum dispersion of the double-slit compared to the momentum difference between photons in the two beams.

following, we present the theory of a realistic experiment in which the entire coherence range can be scanned by controlling the probe preparation and suitably varying the parameters of the coherent waves under consideration.

6.3 Dispersion and coherence in two-colour experiments

As discussed in detail in previous chapters, free-free transitions are laser-assisted electron-atom scattering processes in which the atom remains in its ground state while the electron exchanges quanta with the field. Two-colour free-free transitions with parallel lasers have been studied in [43, 90]. In the following, we assume that the laser fields are represented by coherent states, or Glauber states as they are often called², although relevant elements of photon statistics may be readily incorporated (see section 4.4). Due to the inherent factorization property in the free-free transition, it is natural to form the relative laser-assisted signal as the ratio, R , between laser-assisted and field-free cross-sections. In the case of an energy exchange corresponding to l units from the fundamental component in a field also including the s 'th harmonic ($s = 1, 2, \dots$), we obtain the following expression³ in a well-established distorted-wave approximation [44, 53, 38],

$$\begin{aligned}
 R_l(\tau, \mathbf{Q}) &= \sum_{m,n} J_{l-sn}(\alpha_0 \mathbf{Q} \boldsymbol{\epsilon}) J_n(\alpha_s \mathbf{Q} \boldsymbol{\epsilon}_s) \\
 &\quad \times J_{l-sm}(\alpha_0 \mathbf{Q} \boldsymbol{\epsilon}) J_m(\alpha_s \mathbf{Q} \boldsymbol{\epsilon}_s) \\
 &\quad \times \cos((n-m)(\varphi_s - s\varphi)) \langle \Phi_{l-sm,m} | \Phi_{l-sn,n} \rangle_{\tau}.
 \end{aligned} \tag{6.3}$$

The electron momentum transfer, \mathbf{Q} , refers to the relative electron-atom coordinate; α_0 and α_s are the quiver radii of the ordinary field and its s th harmonic (see equation (3.4)), $\boldsymbol{\epsilon}$ and $\boldsymbol{\epsilon}_s$ the linear polarizations and finally φ and φ_s the phases of the fields. The Bessel functions originate as usually from the exact dressing of incoming and outgoing asymptotic Glauber-Volkov states (see section 4.4). The elements, $\langle \Phi_{l-sm,m} | \Phi_{l-sn,n} \rangle_{\tau}$, are overlaps between wavepackets of the external centre-of-mass motion of the probe. The two indices on the wavefunctions denote the number of exchanged photons with the fundamental field and with the s 'th harmonic, respectively. The overlaps depend upon the laser intersection angle, τ . Equation (6.3) is a sum of terms corresponding to specific numbers of exchanged photons, defining competing quantum paths consistent with overall energy conservation. The expression in equation (6.3) rests upon the zero-order soft-photon approximation of section 4.4 and is considered to be valid in the weak-field and soft-photon limit, $\omega \ll q^2/2$, except for small electron scattering angles, where field-dressing effects of the target atom may

² The overlaps between field states corresponding to different quantum paths should, in principle, also be considered. As discussed in section 4.4 these overlaps are, however, essentially complete if the fields are represented by Glauber states and the laser limit of large photon numbers is understood. Then there is no coherence loss due to the fields.

³As discussed in section 4.3, the situation is slightly more complicated if the atomic potential supports resonances which can be reached realistically.

be of importance [100, 101]. Furthermore, it is understood that the classically forbidden region corresponding to the special critical geometry with both lasers aligned along \mathbf{Q} is avoided.

In the Gaussian model, the overlaps in (6.3) may be expressed as

$$\langle \Phi_{l-sn,n} | \Phi_{l-sm,m} \rangle_{\tau} = \exp(-2[\frac{\pi s(m-n)\hbar}{\sigma_Q \lambda} \sin \frac{\tau}{2}]^2), \quad (6.4)$$

where the wavelength, λ , of the fundamental field has been introduced. Equation (6.4) is a special realization of the more general expression in equation (6.2). In the considered case of free-free transitions, the centre-of-mass coordinate of the combined electron-atom probe system is practically coincident with the coordinate of the target atom. Hence, it is the dispersion of the wavepacket of the target atom that governs the degree of coherence. Notice that all overlaps are complete for aligned lasers corresponding to the fact that the recoil of the probe system is the same in this case for all quantum routes compatible with energy conservation. In this *special* case, therefore, there is maximum contrast in the interference fringes. When the two beams are counter-propagating, the overlaps are as small as possible and the fringe visibility is minimal. It is interesting that the full range from complete coherence to non-coherence may be scanned without high-resolution measurements by varying $\sigma_Q \lambda$. Traditionally, there has been little incentive to experimentally control the probe dispersion. Two-colour experiments have until now been restricted to the special $\tau = 0^\circ$ geometry [30, 31] corresponding to “accidental” indistinguishability of the final states. The control of probe (target atom) dispersion should, however, be within experimental reach using highly-collimating atomic-beam machines [102] or trap techniques to prepare cold atomic targets. In turn, coherence studies might provide a technique for *measuring* characteristic parameters of the wavepackets of trapped atoms. A simple possibility would be to study the variation of the coherence signal, R_l , as the intersection angle of the lasers, τ , is varied. A detailed discussion of practical realizations is beyond the scope of this presentation, but we may note that since the coherence signature is controlled by the combined parameter $\sigma_Q \lambda$, consistency might be checked and higher sensitivity achieved by suitable variations of the wavelength of the applied laser fields. The expression of final-state overlaps in (6.4) shows that the loss of coherence increases with the order, s , of the harmonic field. The laser-assisted signal is, on the other hand, reduced if s is increased since the quiver radius in the Bessel functions in (6.3) scales as α_0/s^2 . Somewhat arbitrarily we have chosen to consider the second harmonic, $s = 2$, in the following explicit examples. Figure 6.1 shows the laser-assisted two-photon absorption signal for scattering of 10 eV electrons as a function of the intersection angle for a set of values of the dispersion parameter and a vanishing relative phase. The experimental conditions correspond closely to those of reference [4] as detailed in the caption. The curves in figure 6.1 clearly show that free-free scattering is a sensitive measure of the dispersion of the atomic probe and particularly so for anti-parallel beams. The curve labelled ∞ represents a momentum distribution so broad that all the coherences con-

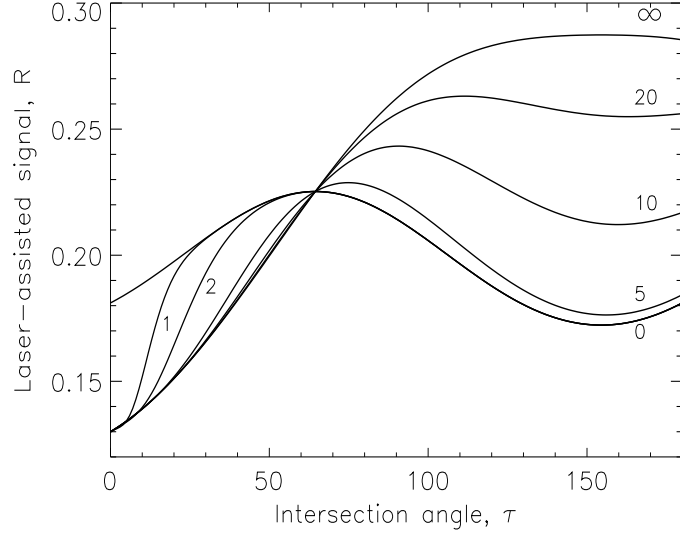


Figure 6.1: Relative two-photon two-colour free-free signal for potential scattering of 10 eV electrons as a function of the laser intersection angle. The laser intensity is $4 \times 10^7 \text{ W cm}^{-2}$ for both colours and the fundamental energy unit is $\hbar\omega = 0.117 \text{ eV}$. The relative phase, $(\delta\varphi = \varphi_2 - 2\varphi)$, is zero. The electron scattering angle is 155° and the angle between the laser polarization of the fundamental field and the incident electron beam is 38° . The curves represent values of $\sigma_Q \lambda / \hbar$ as indicated.

tribute to the sum of equation (6.3). The coherence effect is gradually lost as σ_Q is reduced. In the limit, $\sigma_Q \rightarrow 0$, all coherences disappear. For parallel beams, on the other hand, the coherence effect is completely independent of the value of the dispersion. This explains the pathological behaviour at small intersection angles in the limit, $\sigma_Q \rightarrow 0$. The common intersection at $\sim 64^\circ$ corresponds to a situation where the second harmonic is inactive since the polarization ϵ_s is orthogonal to \mathbf{Q} . Note that the effect of coherence is destructive for angles smaller than this “magic” angle while the effect is constructive for larger angles. In the angular range 180° – 360° , the features discussed appear in a qualitatively similar way.

The variation of the laser-assisted scattering signal with the relative phase between the two colours is illustrated in figures 6.2 and 6.3. The coherence effect is complete and independent of the dispersion for parallel beams. Accordingly, there is no signature of dispersion in this case, although the variation with the relative phase is very pronounced as shown in figure 6.2. For reference purposes, the non-coherence signal, corresponding to the contributions from diagonal terms in equation (6.3), is also indicated. This curve is equivalent

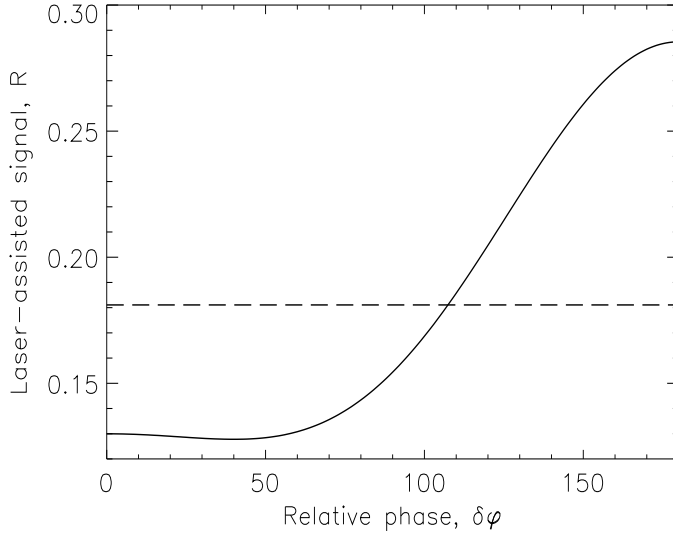


Figure 6.2: Laser-assisted signal for parallel beams as a function of the relative phase, ($\delta\varphi = \varphi_2 - 2\varphi$). The experimental conditions are similar to those in figure 6.1. The full curve corresponds to coherent beams while the dashed curve represents the case of phase indeterminate incoherent laser beams.

to the one obtained with phase indeterminate light fields, thus indicating that beam statistics might be essential to consider (see also section 4.4). As before, the coherence effect may be constructive as well as destructive. When the two beams intersect at a finite angle, there is a very pronounced signature of dispersion. The case of anti-parallel beams is shown in figure 6.3. For vanishing dispersion, all coherences disappear and we obtain the same phase-independent reference result as in figure 6.2.

We now illustrate free-free transitions in two intersecting coherent light fields of equal frequencies. We assume that the two phase-coherent fields are obtained by letting a single laser beam pass through a beam splitter. The relative phase between the two components of the beam is now easily controlled experimentally by varying the difference in their individual optical path lengths. Coherent control is just as feasible with two laser beams of equal frequency as with, for example, beams as considered above consisting of the fundamental and the second harmonic mode, respectively. We assume a Gaussian with momentum dispersion σ_Q for the wavepacket of the initial state of the probe atom. The laser-assisted signal is depicted in figure 6.4. As detailed in the caption the curves show the two-photon absorption laser-assisted signal, $R_2(\tau, \mathbf{Q})$, as a function of the relative phase between two counter-propagating laser beams ($\tau = 180^\circ$). The figure

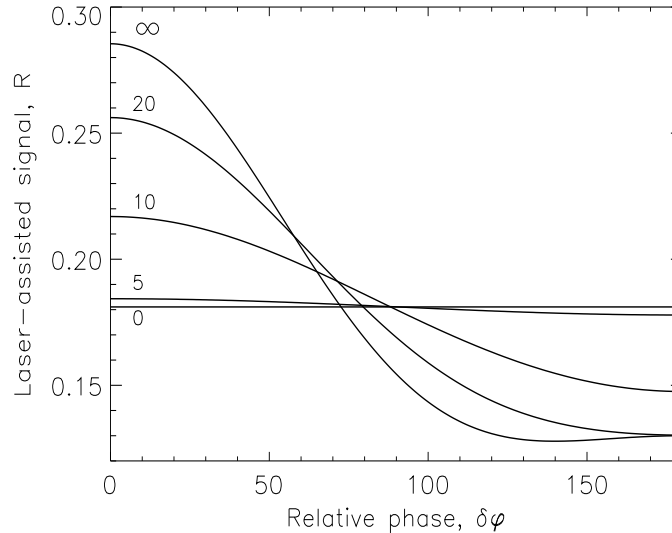


Figure 6.3: Laser-assisted signal for anti-parallel beams as a function of the relative phase, ($\delta\varphi = \varphi_2 - 2\varphi$). The experimental conditions are similar to those in figures 6.1 and 6.2. The curves represent values of $\sigma_Q\lambda/\hbar$, as indicated.

clearly shows that free-free scattering is a sensitive measure of the dispersion of the atomic probe. Again, the curve labelled ∞ represents a momentum distribution so broad that all the coherences contribute to the sum of equation (6.3). The coherence effect is gradually lost as σ_Q is reduced. In the limit, $\sigma_Q \rightarrow 0$, all coherences disappear. For parallel beams, on the other hand, the coherence effect is completely independent of the value of the dispersion as it is, in principle, impossible to say from which light beam the photons are absorbed. As an alternative, one may vary the intersection angle of the two fields at a suitable fixed relative phase as in figure 6.1.

A feature which is common to all values of τ and which is also present in figure 6.3 and 6.4 is a continuous reduction in the contrast as $\sigma_Q\lambda/\hbar$ is decreased from infinity to zero: the dispersion is literally a switch that allows one to scan the whole spectrum between complete coherence and no coherence at all. Unfortunately, we have to await future experimental effort to confirm that the quantum dispersion of probe states may be studied and measured with the two-colour technique indicated above. Alternatively, the present discussion is readily generalized to apply for the case of two-colour multiphoton ionization. Single-photon excitation or ionization experiments with two coherent light sources may also be considered. The relevant radiation sources in the ultraviolet or soft x-ray range are currently under development [5, 103]. The dispersion of target

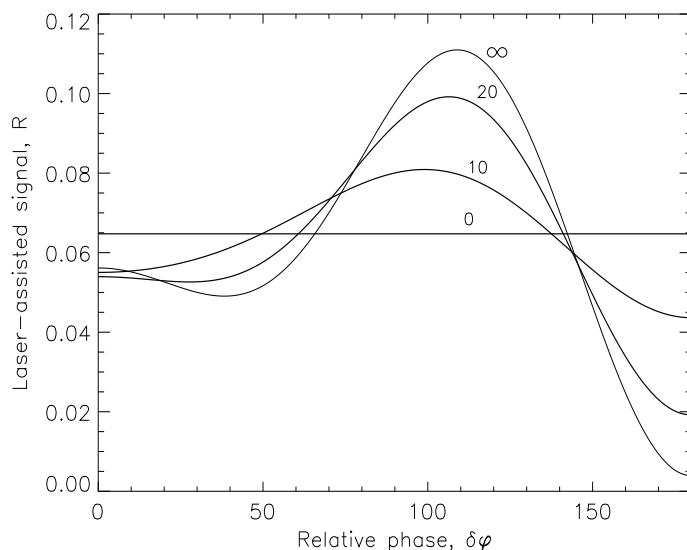


Figure 6.4: Relative two-photon absorption two-laser-beam free-free signal for potential scattering of 10 eV electrons as a function of the relative phase between the two beams. The laser intensity is $4 \times 10^7 \text{ W cm}^{-2}$ for both fields which are counter propagating ($\tau = 180^\circ$). The photon energy is $\hbar\omega = 0.117 \text{ eV}$. The electron scattering angle is 155° . The angle between the laser polarization, ϵ_1 , and the incident electron beam is 38° . The curves represent values of $\sigma_Q \lambda / \hbar$ as indicated.

wavepackets would, in principle, also enter the contrast of the experimental signal in studies of $(N + 1)$ -colour ir-uv photoionization of atoms with higher harmonics designed to measure the relative phase of successive harmonics as proposed in [104].

6.4 Conclusions

In summary, we have discussed how the degree of coherence of the detected signal may be controlled by careful probe preparation. Interference fringes disappear if the probe is prepared initially in a single quantum state while optimum contrast conditions prevail for quantum interference if the probe is a “classical” system with a broad population spectrum on the microscopic scale. We have proposed a new experiment and developed the pertinent theory to study the continuous transition from full coherence to non-coherence utilizing the *microscopic* character of target atoms and a careful probe preparation. Finally, we have indicated how such an experiment may provide direct information on wavepacket properties of suitably prepared cold atoms.

Chapter VII

Introduction to multiphoton ionization of molecules

Compared to the atomic case, the physics of strong laser-molecule interactions is enriched and complicated by the presence of other nuclei which break the spherical symmetry of the binding potential and introduce dissociation as an additional channel of disintegration. While molecular dissociation energies are generally much smaller than their ionization potentials, irradiation by sufficiently intense laser light will lead to strong ionization, which causes the dissociation to occur through highly-charged ionic channels, bypassing the lowest-order dissociation pathway [10, 105]. This form of photodissociative ionization has been termed Coulomb explosion and gives rise to fast fragment ions, whose energy spectra carry information on the ionization process. Due to the inherent multi-channel character of the problem, a coherent picture of cause and effect is only gradually emerging. In fact, most understanding of intense field dissociative ionization is limited to diatoms, though recently more complex systems have been studied experimentally [106, 107, 108]. Recent detailed experimental studies of molecular hydrogen are evidence of the enormous technical advances made in this field [109, 110, 111, 15]. The hydrogen molecule and molecular ion are ideal prototypes for observing the relative importance of the different channels in the dissociative ionization process. We are mainly interested in determining how molecular dissociation affects the ionization rate and the consequent effect on the spectrum of the emerging ions.

In the theoretical analysis of dissociative ionization it has been of great importance to make use of experimental [112, 106, 107, 108, 113] and theoretical (see ,e.g., [21]) evidence showing that linear molecules in an intense laser field have large ionization rates in arrangements with linearly polarized light polarized along the molecular axis. The cylindrical symmetry simplifies the theoretical treatment significantly. Experiments seem to demonstrate that molecules *align* in the laser field with the internuclear axis parallel to the electric field vector [112, 106, 107]. The question of alignment, however, is still a subject of debate and current experimental work [113]. Theoretically, the simplest molecular

system, H_2^+ , has been investigated non-perturbatively using either wavepacket approaches with fixed and, more recently, moving nuclei (see reference [114] and references therein), or by the Floquet approach [19, 22, 115, 9]. Experimentally, strong-field laser-molecule interactions have primarily been studied in the low-frequency DC-like regime [105, 13, 14]. An important finding is that the kinetic energy of the fragment ions appears to be an approximately constant fraction (independent of the laser pulse and ionization fraction) of the Coulomb energy of the ions at the molecular equilibrium internuclear distance [10, 11, 12, 13, 14]. A possible explanation as given by, for example, Seideman *et al* [11] is that the fragment ions do not undergo Coulomb explosion at the equilibrium internuclear distance, but at larger *critical* separations at which electron localization occurs and the ionization rate peaks. This phenomenon of peaks in the ionization rate at certain critical distances has been confirmed theoretically for H_2^+ [16, 17, 18, 19, 20, 21, 22, 23, 24, 116, 114]. For many-electron systems, an alternative possible explanation for reduced fragment kinetic energies has been given by Safvan and Mathur [117] in terms of the significance of electron charge density in-between the nuclei. Brewczyk *et al* [118] have also recently discussed this matter. The value of knowing the ionization rates as a function of the internuclear separation, R , is that they can be used for predicting the energy spectra of the fragment ions and vice versa. Coulomb explosion at a critical distance larger than the equilibrium bond-length implies less energetic fragments.

The mechanisms giving rise to critical distances are still being discussed. The general concept of enhanced ionization in the tunnelling regime, often called Charge Resonance Enhanced Ionization (CREI), has been studied theoretically in qualitative and semi-classical terms [10, 11, 12, 18, 114, 113]. Physically, the mechanism is simply explained within the length-gauge molecular-orbital model. As the molecule dissociates, the symmetric double-well structure is broken by the presence of the external field, and the molecular bond reduces to *localized* polarized atomic orbitals. The atomic orbital is ionized when the fields of the laser and the other ion combine to lower the potential barrier and allow the electron to escape. As R varies, rough estimates of critical distances for enhanced ionization may be predicted classically from the height of the potential barrier between the nuclei with respect to the atomic energy level. These results, however, do not correspond well with detailed quantum calculations for H_2^+ [20]. This is in contrast to simulations applied to large molecules for which classical barrier models are effective [12]. The validity of the tunnelling approach is usually established by the value of the Keldysh parameter [119],

$$\gamma = \sqrt{|E_0|/2U_P}, \quad (7.1)$$

where E_0 is the binding energy of the electron to the atomic or molecular system and $U_P = (F_0/2\omega)^2$ is the ponderomotive energy with F_0 , the laser electric-field strength, and ω the angular frequency in atomic units. The range $\gamma \ll 1$ corresponds to tunnelling ionization by quasistatic fields, while the multiphoton regime in which the electron climbs a ladder of electronic states to reach the continuum through multiphoton absorption corresponds to $\gamma \gg 1$. While this

Table 7.1: Values of Keldysh parameters for the field-free $\text{H}_2^+(1s\sigma_g^+)$ orbital.

λ (nm)	I (W cm^{-2})	$R = 2 a_0$	$R = 6 a_0$	$R = 12 a_0$
212	3.5×10^{13}	10.1	7.9	7.4
212	1×10^{14}	6.0	4.7	4.3
600	3.5×10^{13}	3.6	2.8	2.6
600	1×10^{14}	2.1	1.7	1.5
800	3.5×10^{13}	2.7	2.1	1.9
800	1×10^{14}	1.6	1.2	1.2
1064	3.5×10^{13}	2.0	1.6	1.5
1064	7.1×10^{13}	1.4	1.1	1.0
1064	1×10^{14}	1.2	0.9	0.9

distinction of the physical character of the process is a guide rather than a rule, it is extremely useful for the discussion of phenomena. Table 7.1, for example, shows values of the Keldysh parameter for different wavelengths, intensities and internuclear separations studied in the literature. We note that γ decreases with increasing R due to the decrease in $|E_0|$. We also see that γ decreases with increasing intensity and wavelength due to its dependence on the ponderomotive potential. We will return to table 7.1 in chapter 9. Note in passing that it takes low frequencies and high intensities to approach the tunnelling regime. This is important since, the CREI model can clearly only be expected to offer the correct physical interpretation in the tunnelling regime. However, a great deal of experimental work [105] has been done on systems for which $\gamma \gg 1$ and thus is beyond the validity of the tunnelling model. Accordingly, in these cases, it is not clear how to interpret experimental results. Recently, we have addressed this problem applying the Floquet method to H_2^+ [22, 115, 9]. Results were, for example, obtained for linearly polarized light at intensities $\sim 10^{14} \text{W cm}^{-2}$ and using a wavelength of $\lambda = 248 \text{ nm}$, the fundamental mode of the KrF laser. These laser parameters correspond to $\gamma \sim 5$. The calculations show that critical distances in the multiphoton regime may be understood in terms of Resonance Enhanced Multiphoton Ionization (REMPI) peaks with the molecule ionized via excitation to intermediate states. It is important to note that some REMPI peaks can appear at R -values of similar magnitude to the critical distances predicted by the tunnelling models [22, 115]. This implies similar fragment ion spectra, and hence the experimental spectra are apparently *independent* of the underlying physical mechanism unless the resolution is sufficiently detailed. The REMPI peaks are characterized by diabatic passage through avoided crossings in the real parts of the Floquet quasienergies as the internuclear separation varies, with associated peaks in the ionization rates as true crossings occur in the imaginary parts of the quasienergies [19, 120]. In the tunnelling regime, the corresponding enhanced ionization mechanism has been investigated in detail for DC fields using the Floquet method [20, 21, 24]. When photoexcitation occurs, the nuclei move adiabatically along a single field-molecule potential surface,

and the peaks and troughs in the ionization rate occur as the real part of this quasienergy undergoes true crossings with the real parts of other quasienergies, with corresponding avoided crossings in the imaginary parts. This behaviour is also predicted by an analytical model [121]. Thus, Floquet calculations unambiguously reveal the differences between mechanisms leading to enhanced ionization in the multiphoton and tunnelling regimes, respectively. Note that the distinction between tunnelling and multiphoton regimes is not fully determined by the Keldysh parameter. For example, in experiments with strong femtosecond laser pulses, resonances are so dynamic that their influence on the ionization yield is vanishing [122]. This kind of pulse-dependent behaviour will not be studied within the Floquet approach used here.

A complete study of H_2^+ would require exploration of a large parameter range in bond-length, and molecular orientation as well as laser frequency, polarization and intensity. We confine our study to monochromatic linearly polarized light and take the molecular axis to be parallel with the polarization vector and, accordingly, only study dynamics of $\sigma_{g,u}^+$ -states. It is implicitly understood that the ionization is fast on the time scale of the nuclear dynamics for which reason the coupling between dissociation and ionization channels may be neglected and the electronic motion may be solved for by keeping the nuclei fixed. The present work follows previous time-independent treatments of H_2^+ in which high-frequency [19] and DC fields, applicable to low-frequency laser fields, were considered [21, 20, 24]. We extend and complement the investigations to the multiphoton regime where γ is always somewhat, but not largely, greater than unity. One of the main goals is to study how the phenomenon of enhanced ionization at large internuclear distances in the tunnelling regime extends into the multiphoton regime.

Our method of calculation is the non-perturbative Floquet method. This approach is reviewed in chapter 8 and related to wavepacket methods in section 8.1. Results of calculations are presented in chapter 9. At the equilibrium bond-length, $R = 2a_0$, emphasis is put on the study of the variation with angular frequency and intensity in the generalized cross-section for 6-photon ionization for the state adiabatically linked, with increasing laser intensity, to the field-free $1s\sigma_g^+$ ground state. As ω is scanned through the energy range pertaining to 6-photon ionization, REMPI peaks are observed in the generalized cross-section when the energy difference between the ground state and a higher-lying state corresponds to an integral number of ω . We study in particular the transition from the perturbative regime investigated by Baik *et al* [23] to the non-perturbative regime. As the intensity of the laser is increased, the positions and widths of the resonances are modified dramatically. Pronounced dips in the cross-section may be attributed to interference effects between neighbouring resonances (see figure 9.1). At a wavelength of 228 nm, corresponding to a photon energy of $\omega = 0.2$ au, and for intensities extending well into the non-perturbative regime, we may make comparisons with other theoretical results obtained by solving the time-dependent Schrödinger equation [16, 17] and by using the Padé method [23], respectively. At lower intensities, the agreement

between our calculations and results reported in [23] is good. At higher intensities, our results favour results obtained by the time-dependent calculations [16, 17].

In the multiphoton regime discussed here, there are no previous experimental results or non-perturbative calculations addressing the detailed variation in the quasienergy with internuclear separation, R . We illustrate the physics in this regime by the case of H_2^+ in a laser field of wavelength $\lambda = 248 \text{ nm}$, corresponding to the fundamental mode of the KrF laser. As R increases, a series of REMPI peaks and thresholds between j and $j - 1$ photon ionization where $\{j, j - 1\}$ is the minimum number of photons required for ionization, are scanned through. It is shown how the laser dipole coupling on resonance induces avoided crossings in the real part of the quasienergy, giving rise to bond softening (hardening), i.e., a change in the potential energy curve that weakens (strengthens) the molecular bond and decreases (increases) the barrier to dissociation. Bond-softening (hardening) and its implication on, for example, fragment ion kinetic energies is discussed in detail in the review by Giusti-Suzor *et al* [123]. The REMPI peaks may be identified with diabatic nuclear passage through these light-induced avoided crossings. In addition, we observe and identify a mechanism resulting in enhanced ionization over a broader range of bond-lengths: if a laser-induced avoided crossing in the real part of the quasienergy is passed adiabatically by the nuclei, the coupling to the continuum typically requires only one or a few photons after the passage, and the ionization rate stays high after a rapid increase at resonance leading to a Coulomb explosion of the molecule and corresponding fast protons. We identify this effect for bonds which are both softened and hardened by the field. We discuss the differences in the physics belonging to this kind of enhanced ionization and that encountered in the low-frequency case.

We also consider the intensity range of validity of the 2-state model, where the nuclear motion is restricted to the lowest bonding, $1s\sigma_g^+$, and antibonding, $2p\sigma_u^+$, field-free states. This is done in section 9.2. Traditionally, dissociation of H_2^+ has been described within this model (see, for example, the review by Giusti-Suzor *et al* [123]). Hence, excited and in particular continuum states have been neglected though this is a very poor approximation for high intensities. By comparing potential energy curves obtained with the 2-state and a 30-state approximation, in which the lowest 15 electronic states of each symmetry are considered, we confirm, as concluded by Muller [124], that the distortion of the potentials when including more states is much less in the length gauge than in the velocity gauge. This is particularly true for small bond-lengths ($R \leq 5 a_0$), where the considered energy levels are tightly bound. In general, however, the 30-state model calculations and the large-scale Floquet calculations, including the ionization channel, show that the 2-state-like curves are combinations of several quasienergies undergoing real-part avoided crossings. In the $\lambda = 248 \text{ nm}$ laser field, this results in the breakdown of the 2-state approximation at an intensity of $10^{14} \text{ W cm}^{-2}$. In addition, the ionization rates are so high that the coupling of the bonds to the continuum cannot be neglected. Consequently,

predictions of high intensity 2-state calculations have to be reconsidered, and if accurate nuclear dynamics calculations are required the imaginary parts of complex potential energy curves have to be included. To illustrate this point, we briefly address the question of laser-induced adiabatic stabilization and estimate that any vibrationally trapped state in the KrF-field will ionize within about 25 fs at an intensity of $10^{14} \text{ W cm}^{-2}$.

In section 9.3, we present accurate multiphoton Floquet ionization rates for H_2^+ for Keldysh parameters in the range $\gamma \sim 1 - 7$. Again we present a detailed study of the variation of ionization rate with bond-length. Additionally, we make quantitative comparisons between two complimentary non-perturbative theoretical methods for treating ionization (and dissociation) of molecules in intense laser fields: energy-domain Floquet calculations and time-domain wavepacket calculations. We therefore consider frequencies used in published wavepacket calculations rather than currently available experimental laser frequencies. When comparing with earlier wavepacket work [116], we discover a new, rich resonance structure previously overlooked (see figures 9.11 and 9.12). There are several bands of critical distances in the multiphoton regime, and these results do not precisely match the values predicted by the quasistatic field ionization model. The results are presented with the aim of establishing reliable bench-marks which will serve as tests of current and future wavepacket methods. Given sets of conflicting wavepacket results, Floquet results can indicate the reliability of the data. Finally, we present plots of dressed state densities illustrating laser-induced hybridization.

Chapter VIII

Floquet approach to multiphoton ionization of H_2^+

Our method of calculation is based upon the Floquet-Sturmian method (see, e.g., the review paper by Potvliege and Shakeshaft [125]). This method is applicable to the description of dynamics arising from periodic interaction potentials. In particular for H_2^+ in a monochromatic light-wave of angular frequency, ω , the wavefunction can be resolved into Floquet-Fourier components. As pointed out already by Shirley [126], the method is equivalent to the representation of the quantized field Hamiltonian by photon number states in the laser approximation.

As we confine our study to the case where the molecular axis is parallel with the polarization vector, $\boldsymbol{\epsilon}$, of the linearly polarized field, the Hamiltonian is invariant with respect to rotations about this axis. Consequently, the magnetic quantum number is conserved, and our study is restricted to the dynamics of $\sigma_{g,u}^+$ -states (since the field-free molecule is assumed to be prepared in the $1s\sigma_g^+$ or the $2p\sigma_u^+$ state). The Born-Oppenheimer approximation is introduced by assuming that the coupling between dissociation and ionization channels can be neglected due to the difference in time scales of nuclear and electronic dynamics when exposed to the action of the laser field. The problem of the electronic motion may, therefore, be solved by keeping the nuclei fixed. Consider the electron to have the coordinates \mathbf{r}_1 and \mathbf{r}_2 with respect to the nuclei, which we label 1 and 2. The internuclear axis is then given by $\mathbf{R} = \mathbf{r}_1 - \mathbf{r}_2$, and the electron coordinate is $\mathbf{r} = \frac{1}{2}(\mathbf{r}_1 + \mathbf{r}_2)$ with respect to the origin at the internuclear midpoint. Working in the Coulomb gauge and adopting the dipole approximation, the electronic Hamiltonian may be written in the form:

$$H = H_0 + V(t), \quad (8.1)$$

where

$$H_0 = -\frac{1}{2}\nabla^2 - \frac{1}{r_1} - \frac{1}{r_2} \quad (8.2)$$

represents the unperturbed molecular system, which is separable in prolate spheroidal coordinates (λ, μ, ϕ) with the pseudoradius given by (see figure 8.1):

$$\lambda = (r_1 + r_2)/R, \quad 1 \leq \lambda \leq \infty \quad (8.3)$$

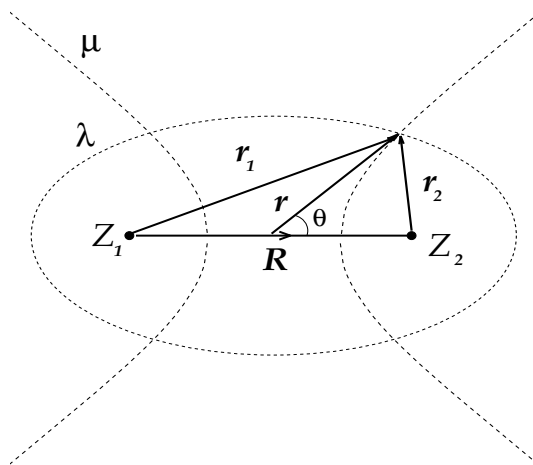


Figure 8.1: Coordinates for the two-centre molecular ion.

and the angular variable

$$\mu = (r_1 - r_2)/R, \quad -1 \leq \mu \leq 1. \quad (8.4)$$

The azimuthal angle is denoted by ϕ . As $r \rightarrow \infty$, we note that

$$\lambda \rightarrow 2r/R \quad \text{and} \quad \mu \rightarrow \cos\theta. \quad (8.5)$$

The prolate spheroidal coordinate system has been demonstrated to be useful also in an external field which prevents a separation of the coordinates [24, 21, 22, 115]. We use these coordinates in our calculations. The volume element is given by: $d\mathbf{r} = (\frac{1}{2}R)^3(\lambda^2 - \mu^2)d\lambda d\mu d\phi$. It is also common to refer to the cylindrical polar coordinates for these systems, and they are expressed as:

$$\rho = \frac{1}{2}R\sqrt{(\lambda^2 - 1)(1 - \mu^2)}, \quad z = \frac{1}{2}R\lambda\mu. \quad (8.6)$$

The interaction of the electron with the electromagnetic field is given by

$$V(t) = V_+e^{-i\omega t} + V_-e^{i\omega t}, \quad (8.7)$$

with $V_- = (V_+)^\dagger$. In the length gauge,

$$V_+ = (F/2)\boldsymbol{\epsilon} \cdot \mathbf{r}, \quad (8.8)$$

while in the velocity gauge

$$V_+ = (-F/2\omega)\boldsymbol{\epsilon} \cdot \nabla. \quad (8.9)$$

Given the periodic perturbation (8.7), Floquet's theorem tells us that solutions to the Schrödinger equation may be sought of the form¹

$$|\Psi(t)\rangle = e^{-i\mathcal{E}t}|G(t)\rangle, \quad (8.10)$$

where \mathcal{E} is the quasienergy to be discussed below, and $|G(t)\rangle$ is periodic, $|G(t)\rangle = |G(t + 2\pi/\omega)\rangle$. In actual experiments, the finite duration of the laser pulse will destroy the strict time periodicity and the actual field-molecule state will be a superposition of the Floquet states in (8.10). However, if the field varies slowly on the time scale of one laser cycle, the initial field-free state may be considered to evolve adiabatically into a single Floquet state [125]. The periodic state $|G(t)\rangle$ can be represented by the Fourier series

$$|G(t)\rangle = \sum_{N=-\infty}^{+\infty} e^{-iN\omega t}|G_N\rangle, \quad (8.11)$$

and the time-dependent Schrödinger equation, $i\partial_t|\Psi\rangle = H|\Psi\rangle$, is readily reduced to an infinite set of time-independent differential equations coupling next-neighbour harmonic components:

$$(\mathcal{E} + N\omega - H_0)|G_N^j\rangle = V_+|G_{N-1}^j\rangle + V_-|G_{N+1}^j\rangle. \quad (8.12)$$

We can convert this set of differential equations into an equivalent set of linear equations by expanding the components, $|G_N^j\rangle$, in a basis set. The basis is chosen to provide an accurate description of the bare molecule. This is done in terms of a normalized orthogonal Sturmian type basis, $\{\varphi_{mn}\}$, of Laguerre, L_m , and Legendre, P_n , functions

$$\varphi_{mn} = N e^{(-\beta/2)(\lambda-1)} L_m(\beta(\lambda-1)) P_n(\mu). \quad (8.13)$$

$N = (8\beta(n + \frac{1}{2})/R^3)^{1/2}$ is the normalization constant and the integer n is even or odd for σ_g^+ or σ_u^+ symmetry, respectively. Using recurrence relations for Laguerre and Legendre functions, the basis in (8.13) yields simple analytic matrix elements for H_0 as well as for the overlap and molecule-field coupling [23, 9]. The imposition of outgoing-wave boundary conditions means that the coupling to the continuum induced by the laser gives rise to a set of quasienergies $\mathcal{E}_j = E_j + \Delta_j - i\frac{1}{2}\Gamma_j$, where E_j is the field-free energy, Δ_j is the laser-induced AC Stark shift, and the imaginary part describes the exponential decay of the wavefunction density at a rate Γ_j . This method also yields the Floquet eigenvectors, which can be used for constructing the Floquet wavefunction. Clearly, the quasienergy is indeterminate to within multiples of the fundamental frequency. Thus \mathcal{E}_j is equivalent, in physical terms, to the sequence of harmonics: $\mathcal{E}_j \pm \omega, \mathcal{E}_j \pm 2\omega, \dots$

¹For systems under the influence of time-dependent periodic potentials one can use Floquet's theorem. It is exactly analogous to Bloch's theorem familiar from the study of systems with a potential periodic in configuration space. We will not attempt to describe the Floquet theory in detail, but simply outline the salient features of the theory and refer the reader to [125] for details.

The quasienergies are in practice determined by the complex-basis-function method [125, 19, 22] by choosing a suitable value for the complex scaling factor, β , in equation (8.13)². In the limit of a complete basis this is equivalent to the complex rotation technique [125, 19, 120], where the problem is solved with a complex Hamiltonian and a basis of real L^2 functions. The complex-basis-function method uses the real Hamiltonian of equation (8.1) with a complex basis. Ideally, all field-free states, including the continuum, are accurately presented in our calculation. In practice, we find a discrete set of eigenvalues. Some are real (or very nearly real) and negative. These correspond to bound (resonance) states. The remaining energies are complex with real parts that are positive and imaginary parts that are negative. The associated states of the molecule describe states of a discretized decaying continuum. The characteristic spatial extent that is covered by the basis is related to the energy spacing of the real parts of the continuum eigenvalues [127]: the energy spacing is proportional to the number of basis functions, so that the space accurately spanned by the basis is proportional to the number of basis functions.

The molecule-field interaction V_{\pm} can be expressed in the length or velocity gauges. There is no physical distinction between the use of either gauge for the calculation of the properties of a system interacting with light. Indeed this equivalence provides an important method for checking the accuracy of the results obtained. Therefore our calculations are performed in both velocity and length gauges. In the weak-field limit, our choice of β produces accurate field-free state energies up to internuclear distances $\sim 12 a_0$. In the table of Sharp [128], energies are presented for the lowest 15 σ -states of gerade and ungerade symmetry. At $R = 2 a_0$, for example, the relative difference between Sharp's data and our field-free states is smaller than 0.005 %.

The basis has to be chosen large enough to make results stable with respect to variations in the number of basis functions and the parameter β . We have established that $\beta = 2e^{-i\pi/9}$, 40-60 Laguerre functions, 5-6 Legendre functions per field-free symmetry, and 7-12 symmetry mixing blocks corresponding to 14-25 Floquet blocks with virtual emission of 4-8 photons and virtual absorption of 9-15 photons, give accurate results to at least 3 significant figures in the estimates of the ionization rate and to typically 6 significant figures in the real part of the quasienergy for the considered wavelengths and intensities.

8.1 Relation to wavepacket calculations

In general, wavepacket calculations are advantageous when one studies multiphoton ionization in ultrashort, strong laser fields. The Floquet method, on the other hand, is ideal under conditions of nearly monochromatic fields of slowly

²We refer the reader to appendix B for a discussion of the matrix structure and the inverse iteration scheme [120] used for finding the complex eigenvalues. In appendix C, we briefly discuss the complex-basis-function and the complex-scaling methods. A thorough discussion related to multiphoton ionization may be found in [125] and references therein.

varying amplitude. It can be used to predict photoelectron spectra and harmonic generation rates [121] and it can be extended to consider pulse profiles [129]. Recently it has been demonstrated [130, 131] in a study of stabilization of atomic hydrogen in circularly polarized light that the adiabatic single Floquet state approximation may be used to interpret results obtained by direct integration of the time-dependent Schrödinger equation, using a very short pulse of only ~ 12 fs [132]. Also, Piraux and Potvliege have studied time-dependent and Floquet methods for stabilization [133]. A fair comparison of wavepacket and Floquet methods for ionization rates of a given state presupposes that we can isolate a particular exponentially decaying Floquet state; the coupling to the continuum introduced by the laser makes all states into resonances with finite widths. This demands that the field is not strong enough to ionize the system before the periodicity of the field is established. In practical terms, this means that the lifetime of the resonance state should be several optical cycles. A more delicate point, however, concerns whether the resonance state is isolated or not. In the wavepacket approach, we might have two or more strongly-coupled resonances which allow population transfer (Rabi mixing). If this occurs, although the resonance states are well defined, the bound-state populations do not follow an exponential decay and the concept of ionization rate is not meaningful. From the Floquet viewpoint, based in the energy domain, the presence of an avoided crossing in the real part of the quasienergy, signifying an M -photon transition with $M = 1, 2, 3, \dots$ between field-free states, results in a partition of the field-free state into several dressed-states; the precise fractions depend on the dipole moments, intensity of light and pulse shape. This is important for several reasons, not least the fact that the mixing can be thought of as a laser-induced bond hybridization which mixes tightly-bound compact orbitals with loosely-bound diffuse orbitals. Thus, the comparison between Floquet and wavepacket results will be direct only if the time-dependent wavefunction can be interpreted as a single Floquet state, varying adiabatically as the field is turned on slowly [130]. Otherwise, wavepacket rates will either be a ‘best fit’ to the decay of several Floquet states for short pulse duration or will approximate either the longest living or most heavily populated Floquet state ionization rates for long pulses, with distortion due to transient terms. The Floquet calculations have the advantage that in principle rates for each dressed state may be calculated unambiguously, though in practice only a few relevant rates are calculated.

Explicitly, for H_2^+ , a comparison ([22] and section 9.2 below) performed at equilibrium separation, $R = 2 a_0$, at a laser frequency of $\omega = 0.200$ au and at laser intensities giving Keldysh parameters in the range $2 \leq \gamma \leq 8$, placing the study in the multiphoton regime, shows that rates obtained by the wavepacket method [16, 17] agree reasonably well with Floquet rates for the field-molecule state adiabatically linked with intensity to the field-free $1s\sigma_g^+$ ground state. In the tunnelling to the intermediate regime, comparisons between time-averaged DC Floquet rates [20] and the wavepacket rates for $\lambda = 1064$ nm and an intensity of $10^{14} \text{ W cm}^{-2}$ of Zuo and Bandrauk [18] also show reasonably good agreement, although for $R > 5 a_0$ the Floquet calculations suggest that the bulk of the

ionization takes place near the end of the pulse rise around intensity $7.1 \times 10^{13} \text{ W cm}^{-2}$. It was noted that at the second peak in the ionization rate at $R = 10 a_0 - 11 a_0$ the Floquet rate is higher than the time-dependent rate due to a noticeable portion of the ionization occurring at an angle to the molecular axis [20]. The signal characteristic of the tunnelling regime with two broad maxima in the ionization rate as a function of R is also seen in experiments on H_2^+ [110].

In the adoption of wavepacket methods to molecular problems, the two-centre nature of the molecule demands some simplifying assumptions. It is usual to consider an arrangement with the molecular axis parallel to the laser polarization direction. Chelkowski *et al* [116, 114] have performed full dynamic non-Born-Oppenheimer wavepacket calculations. Apart from having resulted in ionization and dissociation probabilities, these calculations have given useful insight into the stabilization of laser-induced vibrationally trapped states and the relative importance of the dissociation channel to the Coulomb explosion channel. The dissociative ionization process has been considered at wavelengths of $\lambda = 212 \text{ nm}$ [116] and $\lambda = 600 \text{ nm}$ [114]. From the Keldysh parameters in table 7.1, we note that the calculations at $\lambda = 212 \text{ nm}$ are in the multiphoton regime while the $\lambda = 600 \text{ nm}$ calculations are in the intermediate regime ($\gamma \sim 1$). The calculations, which include nuclear vibrations, have been performed in the length gauge. The electron is confined within a perfectly reflecting, impenetrable cylinder of radius $8 a_0$, and the one-dimensional nuclear motion is restricted to the axis of the cylinder. Cylindrical coordinates (ρ, ϕ, z) with this axis as the z -axis and the origin at the nuclear centre of mass are used. Pulses in which the field amplitude rises linearly from zero to its maximum over 1 fs and is maintained for up to 26 fs have been considered for $\lambda = 212 \text{ nm}$. These papers [116, 114] follow previous wavepacket calculations with fixed nuclei [16, 17, 18]. Ionization rates are calculated from an exponential fit to the decaying probability function inside a cylinder of appropriate size containing the bound states. The electron escape, or ionization process, is taken to occur across the ends of the cylinder [16]. The field amplitude rises to maximum over a few cycles and is then maintained at maximum until enough data has been accumulated to make the exponential fit. Using a similar method, fixed nuclei rates have been calculated in [116, 114] to analyze the results of the full dynamical non-Born-Oppenheimer calculations. Reference [17] uses an absorbing boundary for large ρ . We discuss the differences between these two models in section 9.3. It is difficult to obtain very accurate estimates for ionization rates using wavepacket methods. Typically, this approach offers estimates that are accurate to one or two significant figures at best.

We note in passing that considerable physical insight can also be gained from a colinear 1D model of H_2^+ described by Kulander *et al* [134]. However, the restricted motion of the electron prevents quantitative comparisons between 3D Floquet rates and rates obtained within this 1D model.

Chapter IX

Multiphoton ionization of H_2^+ : calculations and conclusions

9.1 Variation of ionization rates with frequency and intensity

We consider the variation of ionization rates with frequency and intensity for fixed R . The generalized j -photon ionization cross-section, defined by

$$\sigma_j = \omega\Gamma/I^j \quad (9.1)$$

with I the laser intensity, may be used to reveal non-perturbative behaviour as $\Gamma \propto I^j$ according to perturbation theory. Figure 9.1 shows σ_6 for the $1s\sigma_g^+$ ground state at $R = 2a_0$ as a function of laser frequency for different intensities. We avoid the 7- and 5-photon ionization thresholds because of difficulties in calculating a rate when many Rydberg states are involved: a similar problem is described in the review by Potvliege and Shakeshaft [125].

The resonances in figure 9.1 change position with increasing intensity. For example, the resonance situated at $\omega \approx 0.186$ au for an intensity of $5 \times 10^{12} \text{ W cm}^{-2}$ moves, due to the AC Stark shift, to $\omega \approx 0.195$ au at an intensity of $10^{14} \text{ W cm}^{-2}$. This particular resonance may be identified with an ionization channel going through a 4-photon transition to a higher-lying electronic state [23]. All the other spectral lines in figure 9.1 correspond to 5-photon resonance transitions. In the notation used for describing resonant enhanced multiphoton ionization (REMPI) an $M+N$ photon resonance denotes the fact that M -photon absorption leads to a resonance and additional N photons to ionization. In other words the different lines may be identified as 4+2 and 5+1 REMPI resonances.

The asymmetric non-Lorentzian shapes of the 5- and 4-photon resonances in figure 9.1 are also encountered in, for example, the 2-photon generalized cross-section of hydrogen [120, 19] and thus seem to be generic in character. At low intensities these shapes may be understood using a two-level analytical model [135] predicting that the rate in the vicinity of a resonance will be higher for red-shifted than for blue-shifted light due to a linear term in the detuning from the resonance. The drop in the rate for detunings to the blue may be further

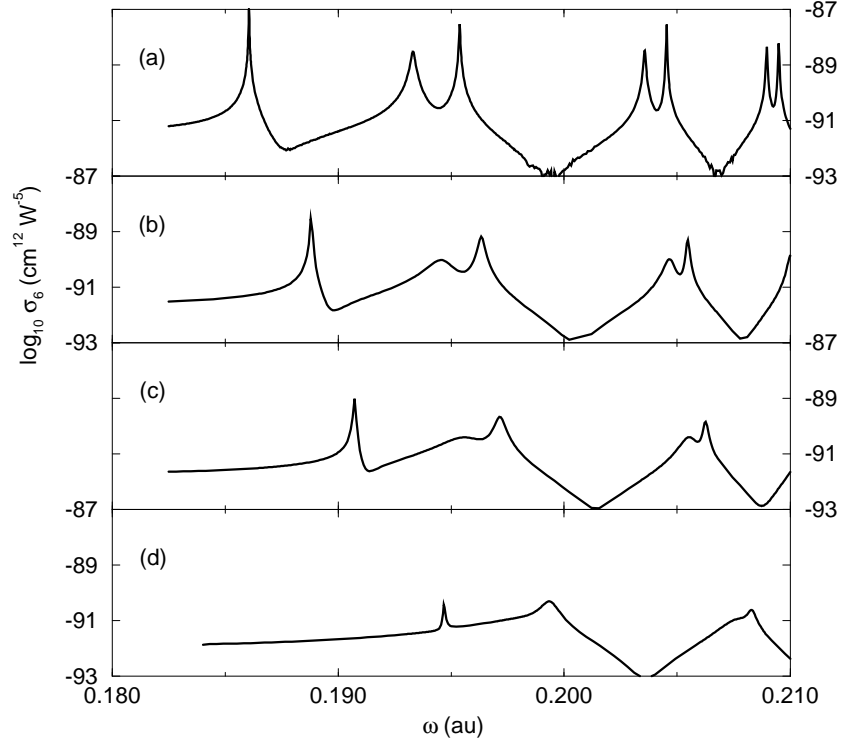


Figure 9.1: Generalized cross-section for 6-photon ionization of $H_2^+(1\sigma_g)$ at $R = 2a_0$ for varying laser frequency at intensities: (a) $5 \times 10^{12} \text{ W cm}^{-2}$, (b) $3 \times 10^{13} \text{ W cm}^{-2}$, (c) $5 \times 10^{13} \text{ W cm}^{-2}$, (d) $10^{14} \text{ W cm}^{-2}$.

enhanced by interference with a neighbouring resonance. This is exemplified by the pronounced dips clearly seen around $\omega = 0.2 \text{ au}$ and $\omega = 0.2075 \text{ au}$.

Besides shifting the positions of resonances, increasing the laser intensity may also gradually quench the resonant enhancement due to power broadening. This becomes particularly explicit in figure 9.1 when following, as a function of increasing intensity, the two resonances starting out at $\omega \approx 0.193 \text{ au}$ and $\omega \approx 0.195 \text{ au}$ which develop into a single broad feature at $\omega \approx 0.2 \text{ au}$. This intensity dependent shift also explains the very sudden enhancement of the ionization rate, as displayed in table 9.1, as the intensity is increased from $5 \times 10^{13} \text{ W cm}^{-2}$ to $10^{14} \text{ W cm}^{-2}$ for a frequency of $\omega = 0.2 \text{ au}$ ($\lambda = 228 \text{ nm}$). Table 9.1 compares ionization rates obtained by us with results obtained by other methods. These are based on the time-dependent Schrödinger equation [16, 17] and the Padé method [23]. Our velocity and length gauge rates are in accord up to within 3-6 figures. An exception to this appeared at $6 \times 10^{14} \text{ W cm}^{-2}$, where our basis in the length gauge only gave converged results for the real part of the quasienergy.

Table 9.1: Rates in s^{-1} for ionization of $\text{H}_2^+(1s\sigma_g)$ at $R = 2a_0$, $\omega = 0.2 \text{ au}$. The values of [17] are the revised ones reported in [23].

I (W cm^{-2})	Ionization rate (s^{-1})			
	[17]	[16]	[23]	Present([22])
5×10^{13}	6×10^7		1.3×10^8	1.1×10^8
1×10^{14}	3×10^{10}		2.1×10^{11}	1.4×10^{11}
2×10^{14}	4×10^{11}		1.0×10^{12}	1.6×10^{12}
3×10^{14}	4×10^{12}	3×10^{12}	5.7×10^{12}	5.5×10^{12}
3.9×10^{14}	2×10^{13}	1×10^{13}	1.6×10^{13}	1.4×10^{13}
5×10^{14}	3×10^{13}	5×10^{13}	4.5×10^{13}	3.4×10^{13}
6×10^{14}		2×10^{13}	9.5×10^{13}	2.5×10^{13}

The velocity gauge rate is fully converged. In general, the results of Baik *et al* [23] are in better agreement with our data than the results of Chelkowski *et al* [16]. However, at the highest intensities, 5×10^{14} and $6 \times 10^{14} \text{ W cm}^{-2}$, our rates are significantly lower and similar to rates obtained by Mies *et al* [17] and Chelkowski *et al* [16], respectively. Thus, it appears that resumming the perturbation series [23] overestimates the rate at these intensities. The drop in the rate as the intensity is changed from 5×10^{14} to $6 \times 10^{14} \text{ W cm}^{-2}$ may be understood by noting that the shift of the ground state with respect to the continuum for these high intensities is so large that we move across the threshold and into the regime where seven photons are needed for ionization. Note that the Keldysh parameter ranges from $\gamma \approx 8$ to $\gamma \approx 2$ as we pass through the intensities in the table. Even for $6 \times 10^{14} \text{ W cm}^{-2}$, the physical mechanisms, therefore, correspond to those in the multiphoton regime.

Chelkowski *et al* [16] also present time-dependent rates calculated at $R = 3a_0$. The time-dependent calculation involves strong mixing of at least two Floquet states as $R = 3a_0$ is close to a one-photon resonance between the $1s\sigma_g^+$ and $2p\sigma_u^+$ states. This is shown in figure 9.10. The precise mixture of the Floquet states will depend on the pulse shape of the laser. We return to the rates at $R = 3a_0$ in section 9.3. At the equilibrium separation, in contrast, the Floquet state adiabatically linked, with increasing intensity, to the field-free ground state dominates the time-dependent fixed-nuclear calculation.

9.2 Variation of ionization rates with internuclear separation

9.2.1 Diabatic and 2- and 30-state adiabatic potential energy curves

As the molecular bond-length increases for a fixed frequency of light a sequence of resonances will be encountered. This means that during the fragmentation process, dissociation or vibrationally excited channels can have enhanced ionization rates at a range of distances leading to a Coulomb explosion of the molecule.

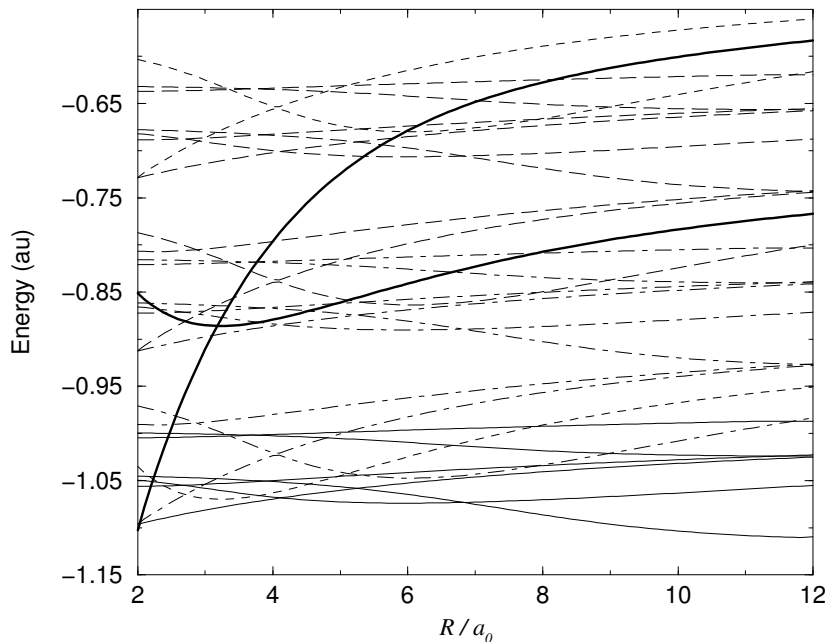


Figure 9.2: Potential energy curves as a function of R at $\lambda = 248$ nm: ———, the $1s\sigma_g^+$ and the 1-photon displaced $2p\sigma_u^+$ potential energy curves; - - -, 2-photon, - - -, 3-photon, - · -, 4-photon, ———, 5-photon displaced potential curves, respectively.

Figure 9.2 shows some field-dressed diabatic potential energy curves as function of internuclear separation for a wavelength of 248 nm. The curves simply show field-free electronic energies shifted by multiples of the photon energy with respect to the ground state. The contribution to the energy from the Coulomb repulsion between the two nuclei is not included. The bold curves correspond to the $1s\sigma_g^+$ state and the one-photon displaced $2p\sigma_u^+$ state. The fine curves represent higher-lying electronic states displaced by 2, 3, 4 or 5 photon energies with respect to the ground state, mimicking absorption of the corresponding number of photons. Concentrating, for the moment, on the $1s\sigma_g^+$ ground state: every crossing between its potential energy curve and another dressed state indicates the presence of a resonance condition. A crossing between the $2p\sigma_u^+$ state and another curve also corresponds to fulfilment of a resonance condition, but now the resonance is reached with one photon fewer compared with excitation from the ground state. Using figure 9.2, the various resonances in the ionization rate displayed in figure 9.6 are readily identified. However, we first examine

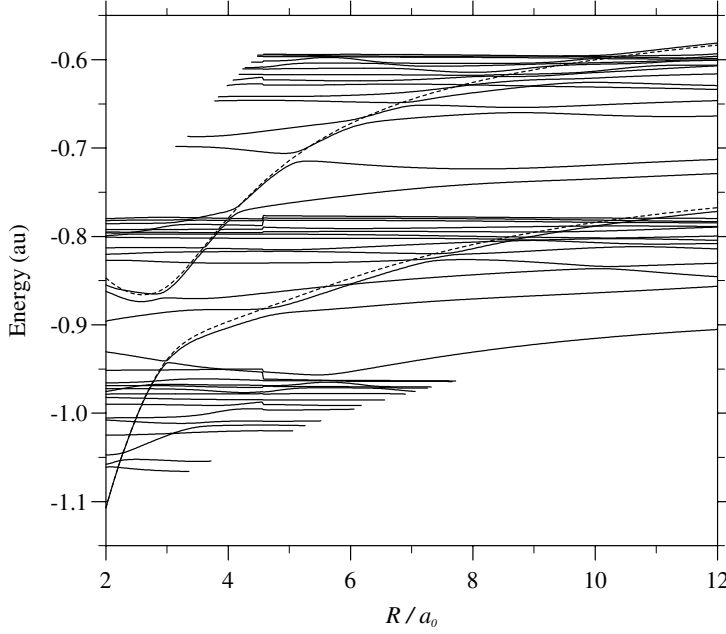


Figure 9.3: Length gauge adiabatic potential energy curves at $\lambda = 248$ nm, $I = 10^{14}$ W cm $^{-2}$ as a function of R : - - -, 2-state calculation; —, 30-state calculation.

the corresponding adiabatic field-dressed potential energy curves obtained by diagonalizing the full Hamiltonian at a given intensity. The resonance between the $1s\sigma_g$ and $2p\sigma_u$ state is particularly interesting since this 1-photon crossing is the only one taken into account in the 2-state model of nuclear dynamics (see the review of Giusti-Suzor *et al* [123] and references therein). Figures 9.3 and 9.4 show adiabatic potential energy curves in length and velocity gauges, respectively, at $\lambda = 248$ nm for an intensity of 10^{14} W cm $^{-2}$ in both 2- and 30-state models. We recall that by an N -state model we mean a calculation where the lowest $N/2$ bound electronic states of each symmetry, calculated from our full basis with $\beta = 2$, are taken into account (the real value of β means that only bound states are accounted for, see also appendix C). Figures 9.3 and 9.4 clearly illustrate the strong gauge dependence of calculations not including a complete set of states. This point has been discussed, for example, in the book by Cohen-Tannoudji *et al* [136]. We see by comparison with figure 9.2 how the bonds belonging to the $1s\sigma_g^+$ and $2p\sigma_u^+$ states are softened and hardened, respectively, at the 1-photon avoided crossing at $R \simeq 3 a_0$. Figures 9.3 and 9.4 show

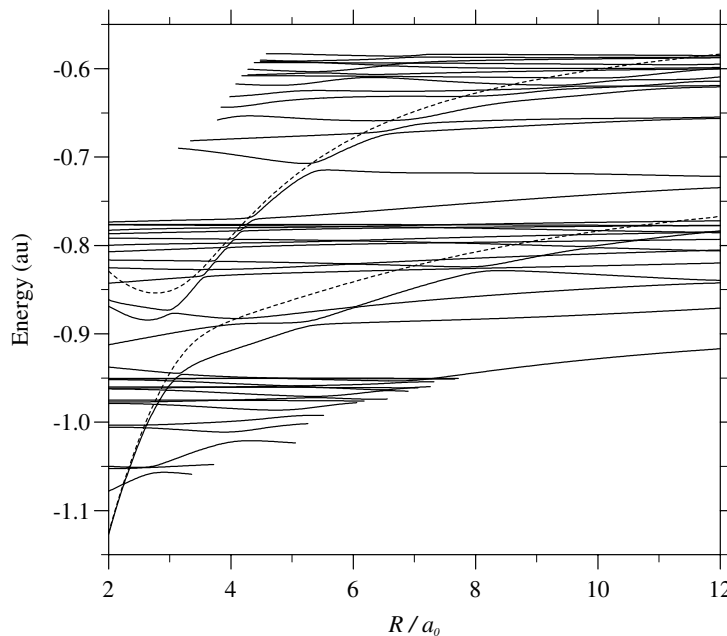


Figure 9.4: Velocity gauge adiabatic potential energy curves at $\lambda = 248$ nm, $I = 10^{14}$ W cm $^{-2}$ as a function of R : - - -, 2-state calculation; —, 30-state calculation.

that the potential energy curves corresponding to the 2-state calculation are made up, in the 30-state calculation, of contributions from several quasienergies with avoided crossings at various points along the “effective” 2-state-like curve having the $1s\sigma_g^+$ and $2p\sigma_u^+$ states as main components. As displayed in figure 9.4, the relative difference in the velocity gauge between the 2-state model and the more realistic 30-state calculation is about 5% near the 1-photon avoided crossing. In the length gauge, the agreement between the two models is much better. This supports conclusions of Muller [124], who obtained effective 2-state-like potential energy curves at various intensities using a time-dependent method with a real non-eigenstate basis set and found faster convergence with increasing basis size in the length gauge.

We thus confirm that 2-state nuclear dynamics calculations should be performed in the length gauge [123]. While this conclusion is valid where the 2-state model is applicable (see below), it might seem to contradict our statement from section 8 that the full Floquet calculations converge more easily in the velocity gauge. The convergence to three or more significant figures in the velocity

gauge is in fact more uniform across the range of R and set of quasienergies considered and may be obtained with a smaller basis than in the length gauge. Away from the 2-state-like quasienergies, the length gauge results vary noticeably on the scale of the figure with respect to the number of states included. The sudden shift in several quasienergies in figure 9.3 at about $R = 4.5 a_0$ is a numerical artifact of the basis set and vanishes when more states are added. Similarly, the positions of the distorting avoided crossings along the 2-state-like curves are converged to at least two figures in the 30-state velocity gauge figure, whereas the positions are still moving towards these converged values in the length gauge many-state calculations of figure 9.3. The generally slower convergence in the length gauge, especially with respect to spheroidal (and spherical) angle functions, is well known and has been discussed recently by Cormier and Lambropoulos [137], and also for Floquet calculations by Shakeshaft [138].

We note that the 2-state-like curves are combinations of several quasienergies undergoing real-part avoided crossings in the many-state calculations above as well as in the full Floquet calculations below. We may consider how realistic it is to construct these curves and ignore the remaining parts of the quasienergies corresponding to excited diabatic states. A full discussion requires details of nuclear dynamics and curve crossings. Although a dynamical simulation is quite feasible, we may make some initial judgements based on the curvatures, \mathcal{F}_i , of the two diabatic curves ($i = 1, 2$) at the avoided crossing. According to the Landau-Zener model (see, e.g., [139]), the probability of a single diabatic passage through an avoided crossing can be written as¹

$$P_{LZ} = \exp\left(-\frac{\pi}{2} \frac{\Omega_g^2}{\hbar v_0 |\mathcal{F}_2 - \mathcal{F}_1|}\right), \quad (9.2)$$

illustrating how the non-adiabatic transition depends on the difference between the curvatures and the energy gap, Ω_g , at the crossing point. In equation (9.2), v_0 is the relative velocity of the two nuclei. If the curvatures differ substantially at a crossing and the two curves approach each other to within, say, less than 0.1 % of the energy value, it seems reasonable to treat the crossing as effectively diabatic. Contrarily, if the gradients are of the same order of magnitude and the curves do not approach each other within, say, 1 % of the energy value, it may be necessary to include both quasienergies in a nuclear dynamics calculation rather than combine the two together as a 2-state-like single curve. For the wavelength $\lambda = 248$ nm, Figures 9.3 and 9.4 indicate that the 2-state approximation breaks down at an intensity of 10^{14} W cm⁻² with some noticeable strong resonances and several overlapping avoided crossings. If the nuclei were to follow the adiabatic path at such a crossing, then rapid ionization would result since the ionization rate along the adiabatic path increases greatly as the dominant field-free component of the quasienergy becomes a highly excited state requiring many fewer photons to ionize. We demonstrate this effect for bonds that are softened and hardened by the field in the Floquet calculations

¹Equation (3) of reference [22] contains a misprint.

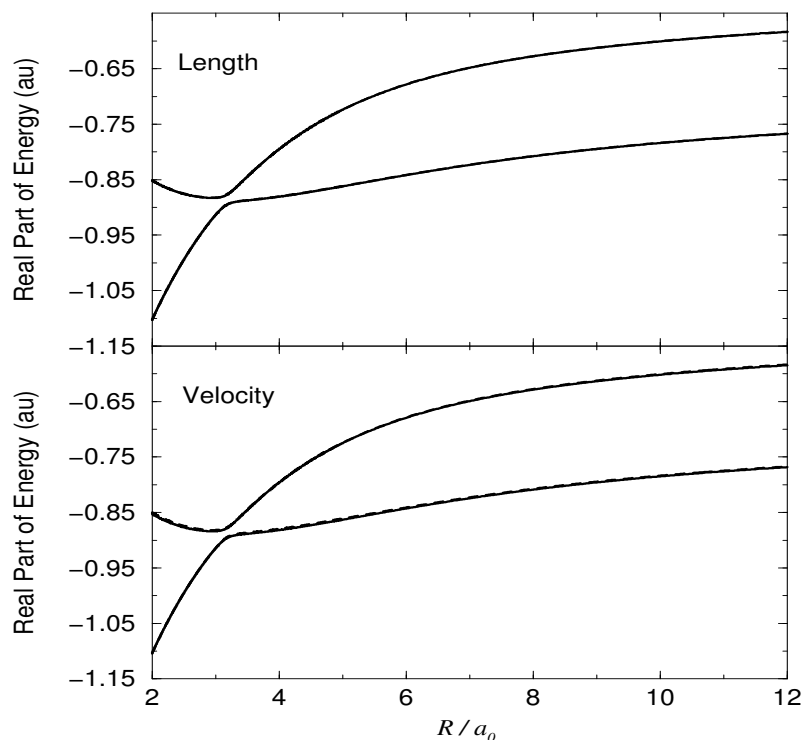


Figure 9.5: Real parts of quasienergies as functions of R at $\lambda = 248$ nm, $I = 5 \times 10^{12}$ W cm $^{-2}$ in length and velocity gauges: —, Floquet calculation; - - -, 2-state calculation.

below (figures 9.7 and 9.9). At lower intensities, the diabatic (perturbative) form of the potential energy curves means that this ionization mechanism is less important. The occurrence of this form of enhanced ionization results in critical distances for ionization over a broader range of R -values than critical distances associated with REMPI-peaks. They are results of multiphoton processes and are, therefore, different in form to the critical distances arising from DC-like tunnelling and over-the-barrier transitions [20, 21, 24].

9.2.2 Large-scale Floquet calculations

We present large-scale Floquet results for a wavelength of 248 nm and for intensities of 5×10^{12} and 10^{14} W cm $^{-2}$. Figure 9.5 shows real parts of quasienergies for an intensity of 5×10^{12} W cm $^{-2}$. As may be seen from the figure, the difference between the full Floquet results and the 2-state energies is negligible in both gauges and the only noticeable avoided crossing is the 1-photon reso-

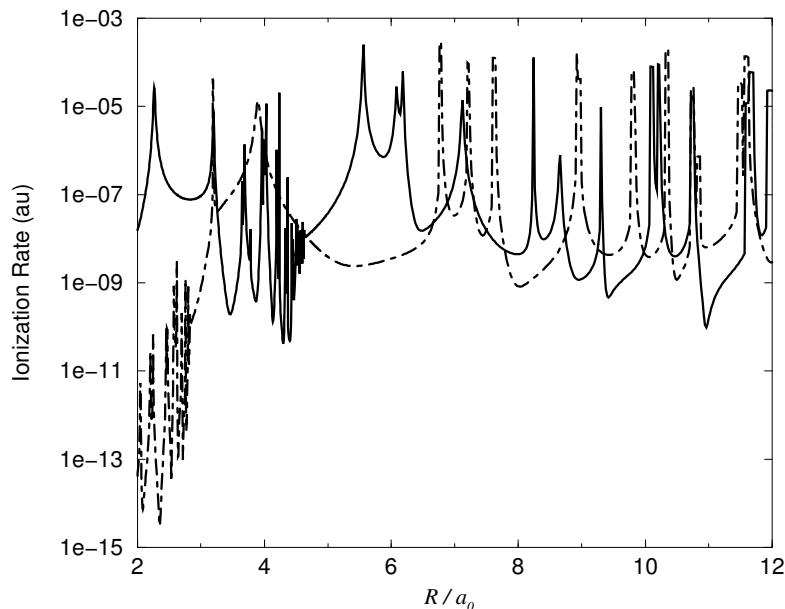


Figure 9.6: Ionization rates as functions of R at $\lambda = 248$ nm, $I = 5 \times 10^{12}$ W cm $^{-2}$: —, upper state in figure 9.5; - - -, lower state in figure 9.5.

nance between the $1s\sigma_g^+$ state and the $2p\sigma_u^+$ state. At this intensity the 2-state approximation is, accordingly, justified and accurate. The “diabatic” crossings manifest themselves as REMPI peaks in the ionization rates shown in figure 9.6. Figure 9.6 displays the ionization rate as a function of R at $I = 5 \times 10^{12}$ W cm $^{-2}$ for both the upper and lower real parts of the quasienergies displayed in figure 9.5. Since the potential energy curves follow adiabatic paths at the one-photon resonance at $R = 3.2 a_0$, the “dominant” component of the two field-molecule states interchanges after the crossing. If the passage is neither diabatic nor adiabatic, both Floquet states (and possibly others, to a lesser extent) are populated at the crossing and it becomes necessary to consider rates from both curves. Ho and Chu [140] as well as Potvliege and Shakeshaft [121] discuss dynamics near curve crossings for atomic systems (see also figure 9.10). The ionization rate of atomic hydrogen, H(1s), at $\lambda = 248$ nm and $I = 5 \times 10^{12}$ W cm $^{-2}$ is 1.40×10^{-6} au [141]. Hence, the separated atomic limit is not reached at $R = 12 a_0$. The current basis set does not allow for an accurate determination of the rate at much larger internuclear distances. This is because single-centre behaviour of the wave

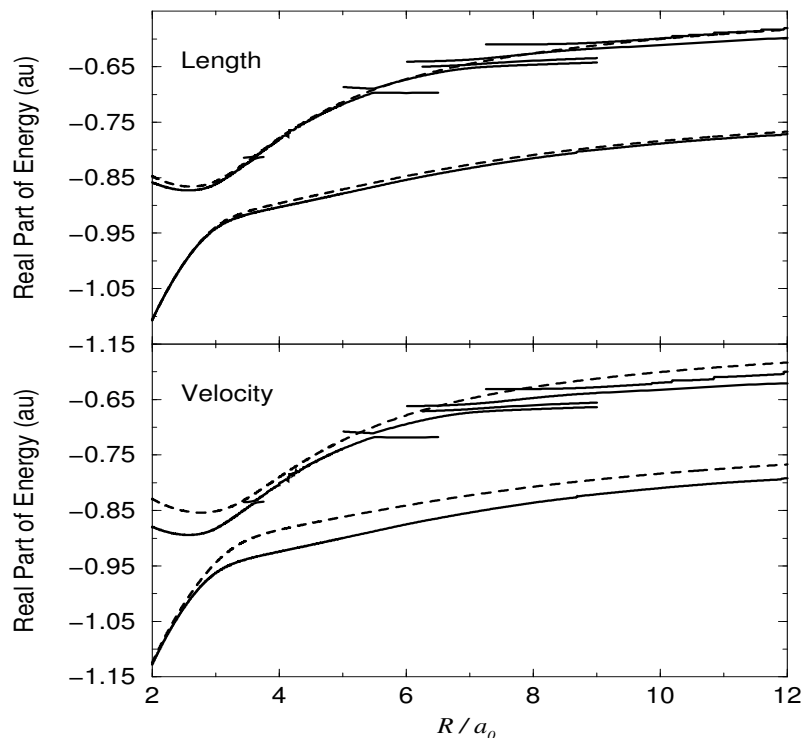


Figure 9.7: Real parts of quasienergies as functions R at $\lambda = 248$ nm, $I = 10^{14}$ W cm $^{-2}$ in length and velocity gauges: —, Floquet calculation; - - -, 2-state calculation.

functions around one nucleus is more pronounced and many more functions of the prolate spheroidal angular coordinate, μ , of equation (8.4) are required to account accurately for this behaviour.

In the outer region ($R \geq 5 a_0$), where 4 photons are required to ionize the molecular ion, the full curve in figure 9.6 is characterized by a series of well separated resonances which may be identified as 3-photon resonances, except the lower structure in the double peak situated at $R \approx 6 a_0$, which is a 2-photon resonance. In the same outer region, the dot-dashed curve displays line shapes corresponding to 2-photon resonances. The inner region ($R \leq 5 a_0$) is characterized by two Rydberg series, the first passing through the 5-photon ionization threshold just below $R = 3 a_0$ and the second passing through the 4-photon threshold at $R \approx 4.8 a_0$. The resonances in the first Rydberg series all arise from 5-photon excitations, whereas the resonances in the latter originate from 4-photon transitions. As mentioned in sections 8 and 9.1, the cut-offs of the Rydberg series depend on the size of the basis. For example, decreasing our

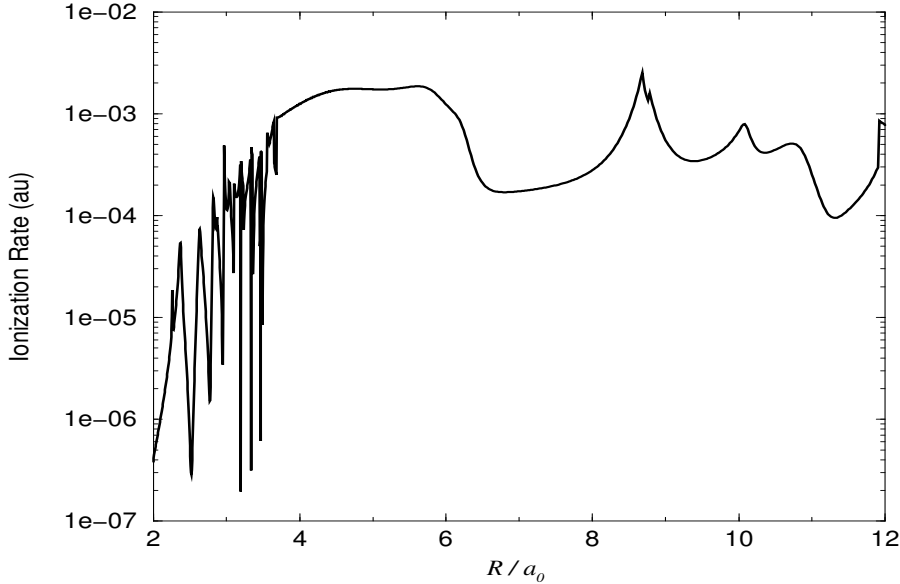


Figure 9.8: Ionization rates as functions of R at $\lambda = 248$ nm, $I = 10^{14}$ W cm $^{-2}$ for the lower 2-state-like potential curve in figure 9.7.

basis size by 25% will typically increase the distance from the cut-off to the threshold, ΔR , by $0.02 a_0$. In figure 9.6 $\Delta R \simeq 0.15 a_0$. The threshold regions are the only values of R for which our results are not converged. For $5 a_0 \leq R \leq 6 a_0$ the difference in the rates is up to a factor of 10^5 at the resonances in the upper state rates. Coulomb explosion is, accordingly, much more likely to occur for nuclei moving on the upper adiabatic curve in figure 9.5.

Figures 9.7, 9.8 and 9.9 show equivalent results for an intensity of 10^{14} W cm $^{-2}$. We see similar general features to the low intensity curves but with dramatic distortion and broadening of resonances due to the stronger field. Again at the threshold regions for 5- and 4-photon ionization there are unconverged rates at $R \simeq 4.2 a_0$ in figure 9.8 and at $R \simeq 5.1 a_0$ in figure 9.9 with widths $\Delta R \simeq 0.5 a_0$ and $\Delta R \simeq 0.3 a_0$, respectively. From figure 9.7 we find that the 2-state curves are closer to the exact curves in the length gauge, but the 2-state model, in particular the upper state, breaks down at several avoided crossings as discussed above in connection with figures 9.3 and 9.4. On the upper state rate graph (figure 9.9), we continue ionization rates along the adiabatic paths at these crossings to see whether critical distances with enhanced ionization over an extended R -range arise. This seems possible at $R \simeq 3.5 a_0$, $R \simeq 5.5 a_0$ and

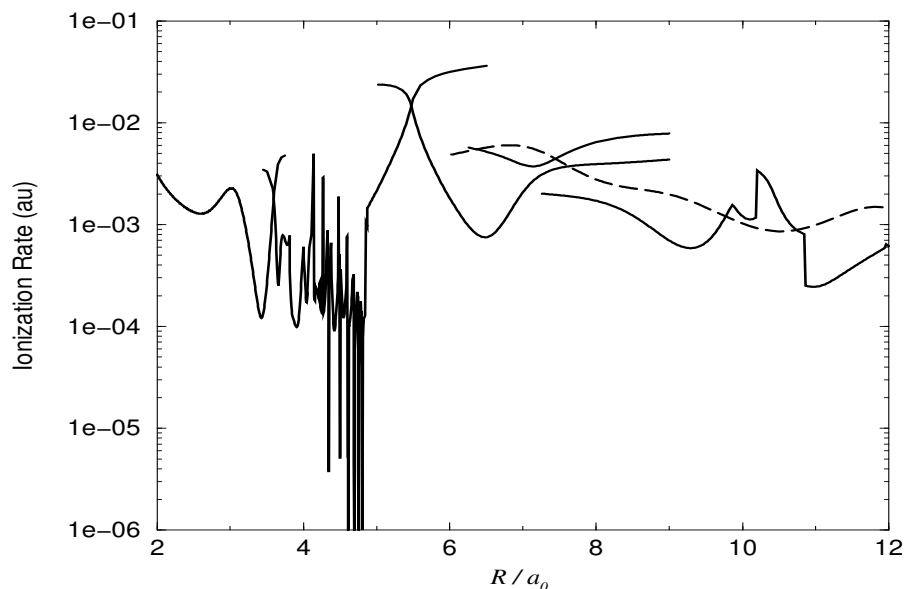


Figure 9.9: Ionization rates as functions R at $\lambda = 248$ nm, $I = 10^{14}$ W cm $^{-2}$ for the upper potential curves in figure 9.7.

from $R \simeq 7 a_0$. In all cases the ionization rate rises and stays high after the crossing. Around $R \simeq 4.2 a_0$ the 2-state-like curve in figure 9.7 jumps among several quasienergies. We note that the potential curves jump slightly at certain other points on figure 9.7: these jumps are crossings that we have taken to be diabatic but for which the adiabatic path may need to be taken into account in very detailed nuclear dynamics calculations. From figures 9.7 and 9.9, we see that the 2-state approximation breaks down completely between $R \simeq 7 a_0$ and $R \simeq 10 a_0$, and we show rates for several nearby quasienergies. The dashed line on figure 9.9 corresponds to the real part of the quasienergy shown on figure 9.7 from $R = 6 a_0$ to $R = 12 a_0$ and is drawn dashed for ease of identification. The Keldysh parameter varies from $\gamma \approx 5$ at $R = 2 a_0$ for the lower state to $\gamma \approx 3$ at larger R and for the upper state. The ionization rate of atomic hydrogen at $\lambda = 248$ nm and $I = 10^{14}$ W cm $^{-2}$ is 6.56×10^{-4} au [141], in accordance with the full curves at $R = 12 a_0$ on figures 9.8 and 9.9, although again the separated atomic limit is not yet reached.

The influence of the ionization channel on possible vibrational trapping has been investigated recently using wavepacket approaches [116, 114, 134]. At a wavelength of 248 nm and at an intensity of 10^{14} W cm $^{-2}$, we may use figures

9.7 and 9.9 for estimating the average ionization rate over the range of internuclear distances relevant for adiabatic stabilization, $3 a_0 \leq R \leq 4 a_0$ [142], to be about 10^{-3} au. Thus, within ~ 30 optical cycles, corresponding to ~ 25 fs, any vibrationally trapped state will ionize (see also [143]). This estimate is of the same order of magnitude as found in [116]. It is intriguing to note from figure 2 of reference [142] that the lowest light-induced vibrational trapped state at the intensity and frequency considered here has its classical turning point near $R \simeq 3.5 a_0$ at which internuclear separation, as seen from figure 9.9, enhanced ionization due to adiabatic nuclear motion is predicted to occur. This might lead to an even faster depletion than estimated above.

We note that the rates of figures 9.8 and 9.9 are velocity gauge rates and are converged to four significant figures.

9.3 Comparisons of wavepacket and Floquet ionization rates

First we consider results obtained at a frequency of $\omega = 0.200$ au. In order to label the Floquet states, we begin by recapitulating some general features of the real parts of the quasienergies. Figure 9.10 shows Floquet energies calculated using the 2-electronic state model. In this model we use our basis with a real value of the parameter β for calculating accurate field-free bound states. Labelling these states with united atom limit prefixes, we then use the two lowest states, $1s\sigma_g^+$ and $2p\sigma_u^+$, as basis functions of model Floquet calculations. This model does not include ionization, but gives approximate values of the real parts of the full Floquet quasienergies which may then be used in nuclear dynamics calculations [123]. Except at resonant transitions, we may label individual Floquet states according to their dominating field-free source states. Thus, the two Floquet states adiabatically linked with intensity to the field-free $1s\sigma_g^+$ and $2p\sigma_u^+$ states will be referred to as the Floquet- $1s\sigma_g^+$ and Floquet- $2p\sigma_u^+$ states, respectively. This assignment, however, breaks down at $R = 3 a_0$, where a 1-photon resonance gives rise to an avoided crossing and causes the two field-free states to mix strongly. Here we refer to the upper and lower energy Floquet states as $|+\rangle$ and $|-\rangle$, respectively. Away from the avoided crossing, the $|+\rangle$ state, for example, is labelled Floquet- $1s\sigma_g^+$ for $R > 3 a_0$ and Floquet- $2p\sigma_u^+$ for $R < 3 a_0$. The labelling presented in figure 9.10 is convenient in the present section since we only need to discuss quasienergies at and beyond the avoided crossing. In section 9.2, we discussed rates also for smaller values of R and therefore simply referred to the curves as upper and lower. The distortion to the real parts of the quasienergies, and diabatic passage through additional avoided crossings introduced by the inclusion of excited states and the continuum in the full Floquet calculations, was discussed in section 9.2.

Table 9.2 compares Floquet results with wavepacket results at $R = 3 a_0$. We present two Floquet rates as we are at the avoided crossing, and both states will contribute to the wavepacket calculations. The Floquet rates in table 9.2 are calculated using the velocity gauge: our length gauge rates, while in general agreement, are not fully converged at the higher intensities shown. As seen

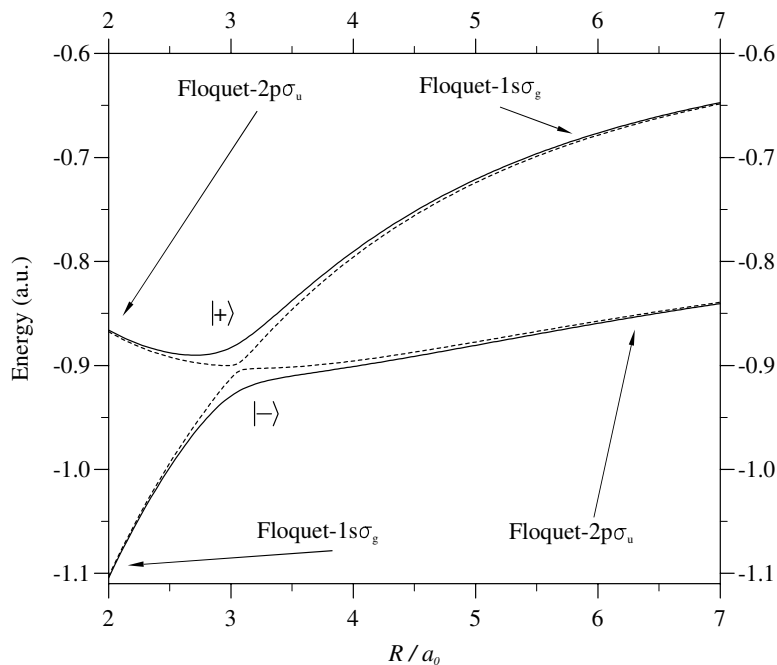


Figure 9.10: Dressed electronic potentials for $\omega = 0.200$ au calculated using the 2-electronic state model. Length gauge results are shown for intensities $10^{12} \text{ W cm}^{-2}$ (dashed curve) and $3.5 \times 10^{13} \text{ W cm}^{-2}$ (full curve). In the low intensity limit, the curves correspond to the energy of the $1s\sigma_g^+$ and $2p\sigma_u^+$ states, the latter shifted down by the photon energy, ω .

when comparing with results presented in section 9.2, the agreement between Floquet and wavepacket rates is not as good as for $R = 2 a_0$ in the same field. This is to be expected as a *single* Floquet state adiabatically linked to the field-free ground state dominates at equilibrium separation. Generally speaking, the wavepacket rates are in between the two Floquet rates of table 9.2. The rates belonging to the $|-\rangle$ -state seem to be slightly more consistent with the wavepacket calculations than those from the $|+\rangle$ -state. [16]. At an intensity of $10^{14} \text{ W cm}^{-2}$, there is a 2-photon $1s-2s$ resonance in hydrogen for $\omega = 0.200$ au and two Floquet rates are shown. Not surprisingly, the agreement between Floquet and wavepacket rates is not as good at the avoided crossing as when a single Floquet state dominates, which is the case for the other intensities shown. In the case of hydrogen, Floquet rates are not available above an intensity of $4.5 \times 10^{14} \text{ W cm}^{-2}$ as many Rydberg states are required for convergence [144].

Table 9.2: Rates in 10^{14}s^{-1} for ionization of $\text{H}_2^+(1s\sigma_g^+)$ at $R = 3 a_0$ and of $\text{H}(1s)$ for $\lambda = 228 \text{ nm}$ ($\omega = 0.200 \text{ au}$).

I (W cm^{-2})	H_2^+ : ionization rates (10^{14}s^{-1})			
	Wavepacket [17]	Wavepacket [16]	$ -\rangle$	$ +\rangle$
1×10^{14}	0.22	0.2	0.41	2.1
2×10^{14}	1.1	0.6	1.8	0.92
3×10^{14}	1.2	0.7	0.24	1.8
3.9×10^{14}	1.2			
4×10^{14}		1.5	0.12	3.1
5×10^{14}	1.6	1.5	0.88	3.9

I (W cm^{-2})	$\text{H}(1s)$: ionization rates (10^{14}s^{-1})	
	Wavepacket [16]	Floquet [144]
1×10^{14}	0.6	1.9/4.8
2×10^{14}	2	3.0
3×10^{14}	4	4.7
4×10^{14}	5	6.1

We now consider quasienergies as functions of R at frequencies of $\omega = 0.2100 \text{ au}$ and $\omega = 0.2149 \text{ au}$, the latter being equivalent to a wavelength of 212 nm . Figure 9.11 shows Floquet rates over a continuous range of internuclear separations for an intensity of $3.5 \times 10^{13} \text{ W cm}^{-2}$. The upper panel (a) shows rates at $\omega = 0.2100 \text{ au}$ and the lower panel (b) shows rates at $\omega = 0.2149 \text{ au}$. In the $\lambda = 212 \text{ nm}$ case, rates obtained by the wavepacket method as presented in [116] are included. The Floquet results are velocity gauge rates. The pattern of the Floquet rates is similar to that found previously in section 9.2 for $\lambda = 248 \text{ nm}$. At equilibrium separation, 6 photons are required to ionize the field-free molecule, the low-intensity 5-photon threshold is around $R \sim 2.2 a_0$, the 4-photon threshold is around $R \sim 3.5 a_0$ for both frequencies, and the 3-photon threshold is around $R \sim 7.6 a_0$ and $R \sim 6.7 a_0$ for $\omega = 0.2100 \text{ au}$ and $\omega = 0.2149 \text{ au}$, respectively. The rates in figure 9.11(b) have the same pattern as those for $\omega = 0.2100 \text{ au}$, but the resonances are shifted to smaller R -values as the photon energy is larger. Results are converged everywhere except at the Rydberg series approaching the AC Stark shifted thresholds. For internuclear distances where 4 photons are needed for ionization, we see a series of REMPI peaks which mainly correspond to 3-photon resonances with excited states. In particular we note a 3-photon resonance near the maximum wavepacket rate at $R = 6 a_0$. For larger R -values the rates belonging to the Floquet- $1s\sigma_g^+$ state are smooth, whereas the rates belonging to the Floquet- $2p\sigma_u^+$ state have two broad resonances. These are REMPI peaks corresponding to 2-photon resonances with the AC Stark-shifted $3p\sigma_u^+$ and $4f\sigma_u^+$ excited states. The resonances are broad because the bound state energies vary more slowly as a function of R in this region. To emphasize the diabatically passed avoided crossing in the real part of

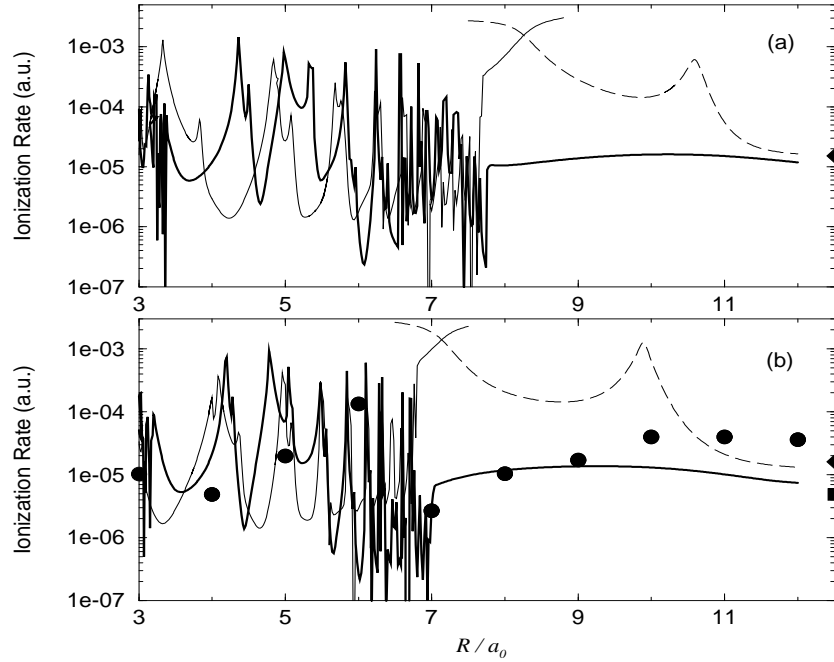


Figure 9.11: Ionization rates as functions of R at (a) $\omega = 0.2100$ au and (b) $\omega = 0.2149$ au ($\lambda = 212$ nm), $I = 3.5 \times 10^{13}$ W cm $^{-2}$. The thick (full) and thin (full and dashed) curves show rates for fixed nuclei pertaining to the Floquet- $1s\sigma_g^+$ and Floquet- $2p\sigma_u^+$ states, respectively. To emphasize the diabatically passed avoided crossing in the real part of the quasienergy, introduced by the $2p\sigma_u^+-3p\sigma_u^+$ resonance transition, the outer part of the Floquet- $2p\sigma_u^+$ state rate is drawn dashed. The circles are rates from [116]. $H(1s)$ rates are shown by a diamond (Floquet approach [144]) and a square (wavepacket method [116]).

the quasienergy, introduced by the $2p\sigma_u^+-3p\sigma_u^+$ resonance transition, the outer part of the Floquet- $2p\sigma_u^+$ state rate is drawn dashed. This is also done in figure 9.12. The $1s\sigma_g^+$ ground state energy is lower than the $2p\sigma_u^+$ state energy, and there are no 2-photon resonances in this range of R to give structure to the Floquet- $1s\sigma_g^+$ rate.

Figure 9.12 shows rates calculated at $\lambda = 212$ nm ($\omega = 0.2148$ au) for an intensity of 10^{14} W cm $^{-2}$. The peaks have Stark shifted, and away from the Rydberg series the peaks have broadened. We note that overlapping rates occur at avoided crossings with excited Floquet states in the real parts of the quasienergies as in section 9.2 and in reference [22]. Both figure 9.11 and figure 9.12 show rates for atomic hydrogen calculated by the Floquet method [144] and the wavepacket method [116]. For convenience these have been put in the figures at $R = 12.5 a_0$. The agreement between the hydrogenic Floquet and wavepacket

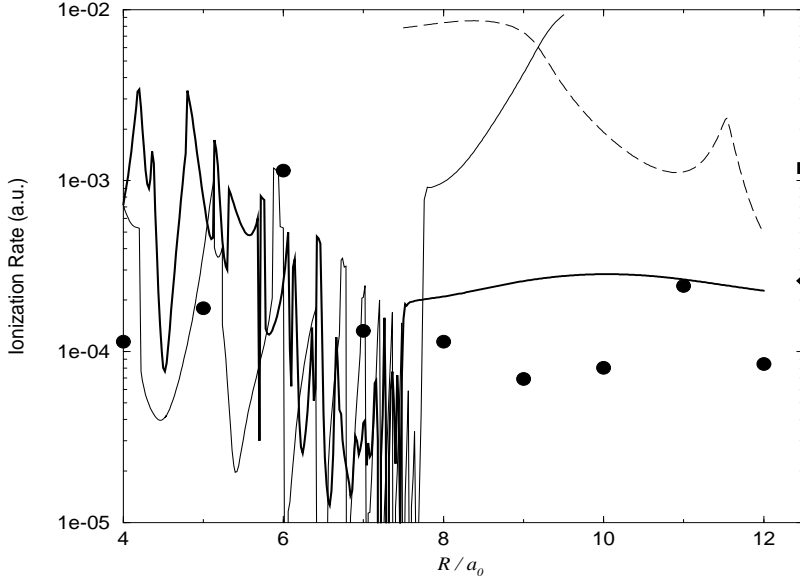


Figure 9.12: Ionization rates as functions of R at $\omega = 0.2149$ au ($\lambda = 212$ nm), $I = 10^{14}$ W cm $^{-2}$. The thick (full) and thin (full and dashed) curves show rates for fixed nuclei pertaining to the Floquet- $1s\sigma_g^+$ and Floquet- $2p\sigma_u^+$ states, respectively. To emphasize the diabatically passed avoided crossing in the real part of the quasienergy, introduced by the $2p\sigma_u^+ - 3p\sigma_u^+$ resonance transition, the outer part of the Floquet- $2p\sigma_u^+$ state rate is drawn dashed. The circles are rates from [116]. H($1s$) ionization rates are shown by a diamond (Floquet approach [144]) and a square (wavepacket method [116]).

rates is not as good as one might expect. The discrepancy is actually worse than is typically the case in table 9.2. A comparison between the H($1s$) and the H $_2^+$ rates shows that the separated atomic limit has not yet been reached. The H $_2^+$ Floquet rates do, however, seem to approach the H($1s$) Floquet rates more than is the case with the wavepacket rates. The molecular H $_2^+$ rates obtained by the wavepacket method [116] follow the Floquet data roughly, but do not agree well. We address this numerical discrepancy in greater detail below. Here we first note that the sparse wavepacket data for the rate as a function of R give a *false impression*. Clearly, figures 9.11(b) and 9.12 show that the R -dependent wavepacket rates do not account for the rich resonance structure revealed by the Floquet calculation: while wavepacket estimates of ionization rates for bond-lengths at intervals of $1 a_0$ appear to have the same broad double-peak structure as found in the DC-like case [21], it appears that this coarse grid has overlooked

the true dependence of the ionization rate described by a complex structure of REMPI peaks. The first broad peak centred at $R = 6 a_0$ is correctly attributed to a 3-photon resonance; as noted above, the REMPI peaks in the 4-photon ionization region are mainly due to 3-photon resonances. The second maxima at $R = 11 a_0$ was indicated to be correlated with a tunnelling resonance characteristic of the CREI mechanism. Noting that the Keldysh parameter at $R = 11 a_0$ in figures 9.11 and 9.12 is $\gamma \simeq 7.4$ and $\gamma \simeq 4.4$, respectively, this actually places the study well within the multiphoton regime. We, therefore, interpret the enhanced ionization rate at $R = 11 a_0$ in terms of REMPI from the Floquet- $2p\sigma_u^+$ state. Taking into account the non-adiabatic laser pulse rise in the wavepacket calculation, we envisage a significant population of the $2p\sigma_u^+$ state and our interpretation is natural. Hence, we identify the maxima at $R = 11 a_0$ as due to a REMPI peak corresponding to the 2-photon $2p\sigma_u^+ - 4f\sigma_u^+$ resonance. We note that the higher peaks in the ionization rate in figures 9.11 and 9.12 correspond to lifetimes of 20-30 optical cycles for an intensity of $3.5 \times 10^{13} \text{ W cm}^{-2}$ and about 10 optical cycles (5 cycles at the top of the $3p\sigma_u^+$ Floquet- $2p\sigma_u^+$ peak) for an intensity of $10^{14} \text{ W cm}^{-2}$. These figures give approximate limits to the sizes of fixed nuclear pulses at these values of R that the Floquet results may model, although the pulses can be longer with dynamic nuclei as R varies between the peaks.

The ionization rates and real parts of the quasienergies as functions of R can be used for estimating the energy spectra of the fragment ions. In table 3 of reference [116], an approximate semi-classical method was used for this purpose: assuming that the electron is ejected at a particular critical distance, R_C , the kinetic energy of the protons is equal to the Coulomb explosion energy, $1/R_C$, plus the energy gained from dissociation along the repulsive $2p\sigma_u^+$ field-free potential starting at estimated initial values of R , corresponding to turning points of vibrational states of the molecule and ending at R_C . We have applied this method using our detailed ionization data and reproduced fragment ion distribution features to the same $\pm 5\%$ accuracy as in [116].

The values of ionization rates obtained by Floquet and wavepacket methods differ widely in absolute terms. We now discuss these numerical differences. There are two main reasons why wavepacket and Floquet rates do not match. The first is that wavepacket calculations may involve a combination of Floquet states, both our two main Floquet states and other states, giving an average ionization rate different from our Floquet rates. It may be argued that this averaging might quench some of the resonance structure, but this would need verification by calculating wavepacket rates over a fine grid of R values. The other reason for the discrepancy is connected with the application of the wavepacket method. To this end, we first study table 9.3.

Table 9.3 shows some H_2^+ bound state energies calculated within prolate spheroids of various fixed maximum values, λ_m , of the pseudoradius (8.3). As in our main calculations, we use Legendre functions for describing the motion in the spheroidal angle coordinate, μ . The functions of the pseudoradius, λ , are now polynomials constructed to be zero on the outer boundary. We use

Table 9.3: Electronic eigenenergies of field-free σ^+ -states using the Lobatto basis functions with the electron confined within a spheroid of varying size. z_m and ρ_m are the semi-major and semi-minor axes of the spheroid, respectively, along the internuclear axis and perpendicular to it in cylindrical coordinates. The energies are in atomic units with respect to the ionization limit of H.

$\rho_m = 8.00a_0$					
$R = 2a_0, z_m = 8.06a_0$		$R = 6a_0, z_m = 8.54a_0$		$R = 12a_0, z_m = 10.00a_0$	
σ_g^+	σ_u^+	σ_g^+	σ_u^+	σ_g^+	σ_u^+
-1.10263	-0.66749	-0.67850	-0.65714	-0.58080	-0.580 68
-0.35215	-0.22072	-0.30836	-0.15734	-0.23872	-0.171 81
-0.21697	-0.02493	-0.19427	-0.09540	-0.04057	-0.017 67
-0.00462	0.15515	-0.02482	0.19254	-0.03991	0.113 72
0.06986	0.32347	0.09111	0.26784	0.04633	0.142 30
0.14588	0.34728	0.20606	0.30522	0.27516	0.449 26
$\rho_m = 20.00a_0$					
$R = 2a_0, z_m = 20.02a_0$		$R = 6a_0, z_m = 20.22a_0$		$R = 12a_0, z_m = 20.88a_0$	
σ_g^+	σ_u^+	σ_g^+	σ_u^+	σ_g^+	σ_u^+
-1.10263	-0.66753	-0.67864	-0.65731	-0.58350	-0.583 39
-0.36086	-0.25541	-0.31249	-0.22743	-0.24866	-0.192 09
-0.23578	-0.13633	-0.24755	-0.14593	-0.19286	-0.191 10
-0.17759	-0.12632	-0.15515	-0.12001	-0.13588	-0.103 03
-0.13000	-0.06792	-0.13245	-0.08462	-0.10226	-0.094 18
-0.09653	-0.06310	-0.08341	-0.04088	-0.09761	-0.050 15
$\rho_m = 40.00a_0$					
$R = 2a_0, z_m = 40.01a_0$		$R = 6a_0, z_m = 40.11a_0$		$R = 12a_0, z_m = 40.45a_0$	
σ_g^+	σ_u^+	σ_g^+	σ_u^+	σ_g^+	σ_u^+
-1.10263	-0.66753	-0.67864	-0.65731	-0.58350	-0.583 39
-0.36086	-0.25541	-0.31249	-0.22743	-0.24866	-0.192 09
-0.23578	-0.13731	-0.24755	-0.14600	-0.19292	-0.191 16
-0.17768	-0.12664	-0.15529	-0.12275	-0.13640	-0.105 45
-0.13079	-0.08593	-0.13401	-0.09088	-0.10644	-0.104 15
-0.10544	-0.08084	-0.09377	-0.07784	-0.10286	-0.068 26

Lobatto shape functions [145], which are Lagrange interpolation polynomials constructed from the endpoints, and Gauss-Lobatto quadrature abscissae in the range $1 \leq \lambda \leq \lambda_m$. For each set of polynomials, only one function is non-zero at each abscissa and end-point. We recall that the field-free Hamiltonian is separable in prolate spheroidal coordinates and all matrix elements in the λ -coordinate are calculated exactly using Gauss-Legendre quadrature. Lobatto shape functions are often used with the associated (approximate) Gauss-Lobatto quadrature in the discrete variable representation: the Gauss-Lobatto quadrature becomes exact in the limit of large numbers of functions [145]. Results in table 9.3 are converged with respect to the number of basis functions. The values z_m and ρ_m show the semi-major and semi-minor axes of the spheroid,

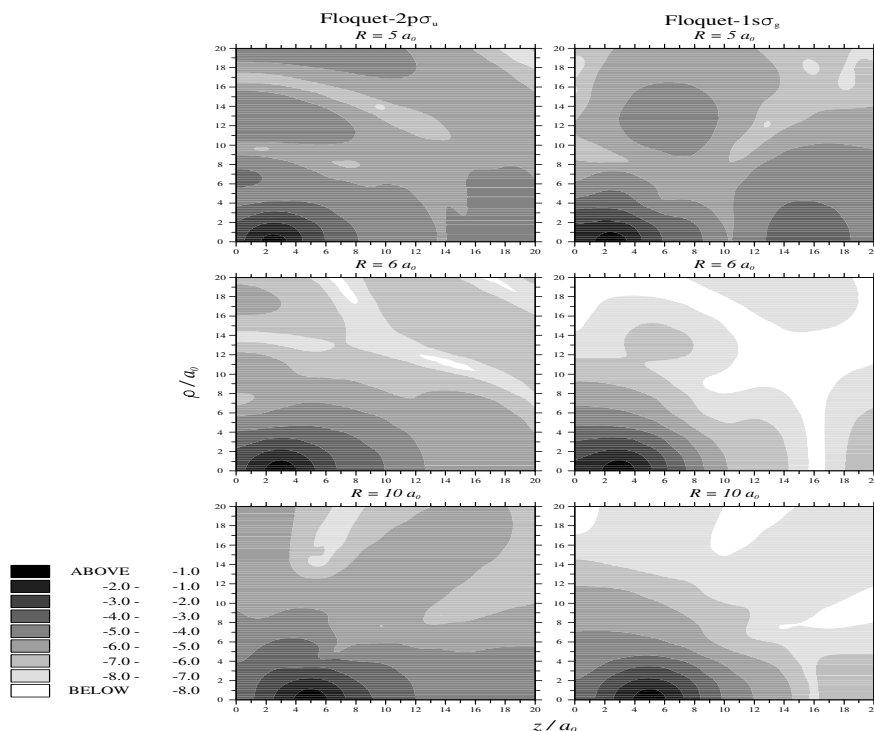


Figure 9.13: Contour plots of the logarithm of the time averaged Floquet wavefunction density, $\log_{10} |\Phi_j(\lambda, \mu)|$, for various R at an intensity of $3.5 \times 10^{13} \text{ W cm}^{-2}$ and at $\omega = 0.2149 \text{ au}$.

respectively, along the internuclear axis and perpendicular to it in cylindrical coordinates: $z_m = (R/2)\lambda_m$ and $\rho_m = (R/2)(\lambda_m^2 - 1)^{1/2}$. The main purpose of table 9.3 is to illustrate the variation of excited state energies with the size of the spheroid. Similar behavior occurs for bound states calculated in cylinders of varying radii. We do not present these results here as the calculations are cumbersome and slowly convergent, requiring two sets of polynomial bases and numerical integration over the Coulomb potential.

From table 9.3 we conclude that by confining the electron within a cylinder of radius $8a_0$ [116], the excited field-free states of the system will be raised in energy if the wavefunction describing them should extend beyond this radius. The REMPI peaks in the confined cylinder model [16, 116, 114] will thus change position to take account of these energy differences, for example to larger internuclear distances where the energy gap is relatively smaller. This would imply

that the wavepacket results overestimate the bond-lengths at which REMPI occurs. We note that if the superimposed values on figure 9.11 are shifted slightly to the left, the agreement between Floquet and time-dependent results is improved. The AC Stark shifting will also be affected by the cylinder model: this will distort the comparison of figure 9.12. Finally on this point, in figure 9.13 we show for a wavelength of 212 nm and an intensity of $3.5 \times 10^{13} \text{ W cm}^{-2}$ sample contour plots of the modulus of the function

$$\Phi_j(\lambda, \mu) = \frac{\omega}{2\pi} \int_0^{2\pi/\omega} dt \Psi_{Tj}^*(\mathbf{r}, t) \Psi_j(\mathbf{r}, t), \quad (9.3)$$

where $\Psi_j(\mathbf{r}, t)$ is the Floquet wavefunction and $\Psi_{Tj}(\mathbf{r}, t) = \Psi_j^*(\mathbf{r}, -t)$ is its time-reversed counterpart [20, 121]. Φ_j is normalized such that

$$(R^3/8) \int_1^\infty d\lambda \int_{-1}^1 d\mu (\lambda^2 - \mu^2) \Phi_j(\lambda, \mu) = \int_{-\infty}^\infty dz \int_0^\infty d\rho \rho \Phi_j(\lambda, \mu) = 1. \quad (9.4)$$

We note that the time-averaging procedure in equation (9.3) means that the plots are symmetric about $z = 0$ and that the restriction to σ^+ -states for field parallel transitions makes the results independent of the azimuthal angle.

The plots in figure 9.13 give an indication of electron density extending beyond the cylinder of radius $8a_0$. We find that if we integrate Φ_j over $|z| \leq 40a_0$ and $\rho \leq 8a_0$, the resulting value is significantly different from unity. The Floquet- $2p\sigma_u^+$ state gives an integral of 0.6 at $R = 5a_0$ and the Floquet- $1s\sigma_g^+$ one of 0.96. At $R = 6a_0$ and $10a_0$, the integrals differ from unity within the second or third decimal place. This quantifies the extent of the electron density beyond $\rho = 8a_0$.

Rather than confining the electron within a cylinder, the use of an absorbing boundary at some appropriate radius has three important advantages: the energy spectrum of the excited states is not perturbed by the boundary, the molecular cloud is allowed to expand and to occupy excited (bound) states, and finally artificial back-scattering of radial photoelectrons, which would suppress ionization, is ideally eliminated. Such an approach has, for example, been used by Mies *et al* [17].

Apart from showing electron density beyond the radius of $8a_0$, figure 9.13 is very interesting due to the fact that it shows the laser-induced hybridization effect with excited field-free states. This is visible when compared with similar plots for field-free states, which may be found in [146]. Comparing with figure 9.11, $R = 5a_0$ in figure 9.13 corresponds to a maximum in both Floquet state rates, and $R = 6a_0$ is a minimum between REMPI peaks. $R = 10a_0$ corresponds to a peak in the Floquet- $2p\sigma_u^+$ state and smooth behavior for the Floquet- $1s\sigma_g^+$ state. At the ionization rate peaks, it may be seen that the electron density spreads out from around the nuclei, both along $\pm z$ and perpendicular to the z -axis.

According to the Keldysh criterion, and for the intensity range in question the case of $\lambda = 212 \text{ nm}$, corresponding to figures 9.11-9.12 above, is firmly in

the multiphoton regime. This is clearly seen from table 7.1 and the discussion in section 7. For the case of $\lambda = 600$ nm, the CREI mechanism has also been advanced to explain the results [114]. This wavelength is not yet amenable to Floquet calculations at the intensities considered, as there are many overlapping Floquet states and avoided crossings. Also, the large number of Floquet blocks required makes the calculations cumbersome. While the Keldysh parameter from table 7.1 suggests the intermediate, if not the multiphoton regime if the mechanism were CREI, we would expect the results shown in figure 4 of Chelkowski *et al* [114] for 10^{14} W cm $^{-2}$ to be essentially the same as those for $\lambda = 1064$ nm in figure 1 of Zuo and Bandrauk [18]. This expectation is due to the fact that quasistatic field processes such as CREI are independent of frequency to first order [24, 20]. The two figures are, however, quite distinct. There are several peaks visible in figure 4 of Chelkowski *et al* [114] with the sample spacing of $0.5 a_0$ in the internuclear separation, so we expect REMPI to be an important influence also at $\lambda = 600$ nm. A method of predicting enhanced ionization for these intermediate cases which are neither properly in the tunnelling or the multiphoton regimes would be of considerable interest.

Finally, with regard to table 7.1, we see from the $\lambda = 1064$ nm intensity 10^{14} W cm $^{-2}$ values that the Keldysh parameter can be as high as $\gamma \sim 1$ with the CREI mechanism reasonably explaining ionization rates for AC fields [20, 18]. In view of the discussion above for a wavelength of $\lambda = 600$ nm, the values suggest that at a lower intensity of 3.5×10^{13} W cm $^{-2}$ ionization rates at $\lambda = 1064$ nm may not be properly explained by the CREI mechanism.

9.4 Conclusions

We emphasize the differences between the multiphoton regime studied here and the tunnelling regime to which the DC work of [21, 20, 24] is applicable. In both cases, quasienergies are found of the fixed-nuclear system for given laser frequencies, intensities and values of R . Then effective electronic field-molecule potential energy curves are constructed as functions of R from the real parts of the quasienergies with the imaginary parts giving the ionization rate. In the multiphoton case, these potentials are obtained from a combination of several adiabatic quasienergies: the diabatic path is taken through a real-part avoided crossing where such an avoided crossing is not too distinct as discussed in section 9.2. The justification for this is that the dominant field-free bound states of interest follow the diabatic path. We then have an associated sharp resonance in the ionization rate with a peak where the imaginary parts of the quasienergies have a genuine crossing. This procedure breaks down as intensity increases and we cannot ignore the adiabatic path: the one-photon crossing between the $1s\sigma_g^+$ and $2p\sigma_u^+$ states is a special case of this need to take account of the adiabatic path, where we have two important mixed bound states with similar energies. For crossings with highly excited states, we have the possibility of enhanced ionization with corresponding critical distances where the ionization rate rises suddenly at the avoided crossing and stays high along the adiabatic path, as

opposed to the narrow resonances along the diabatic path. In the DC case, however, critical distances arise in a completely different way [24, 21]. In this case, we follow a single quasienergy as a function of R . The critical distances with enhanced ionization occur when the real part of the quasienergy has genuine crossings with real parts of other quasienergies: the imaginary parts have corresponding avoided crossings which appear as peaks in the ionization rate (relatively broad with respect to the multiphoton resonances). An analytical model of these two alternative real and imaginary part pairings of avoided and real crossings is given by Potvliege and Shakeshaft [121] in a treatment developed from that of reference [135].

Time-averaged DC rates with or without modifications from perturbation theory seem to give reasonable results for 1064 nm AC fields [20, 24]. As $\gamma \rightarrow 1_+$, we see the breakdown of the diabatic approach to effective potential curves. The wavelength range between 248 nm and 1064 nm will require careful treatment as the multiphoton AC approach may become extremely cumbersome with many more Floquet blocks and closely spaced quasienergies. Time-dependent approaches [116, 114, 134] may be more straightforward in these cases although they do not allow for as detailed a high-energy-resolution study of the quasienergies of the many-level quantum system as the Floquet approach as discussed in section 9.3. We note that the 2-state model in the length gauge gives good agreement with the full Floquet curves for $\gamma \gg 1$, and also in the DC case. We may conjecture that in the intermediate range (248 nm - 1064 nm) the 2-state curves represent some sort of average potential from several closely spaced quasienergies with similar real and imaginary parts, as suggested by figures 9.7 and 9.9.

It will require careful experimental effort to confirm the behaviour of the ionization rates shown in figures 9.6, 9.8, 9.9, 9.11 and 9.12. For the $2p\sigma_u^+$ state the R -scan can, in principle, be done by using appropriately tailored femtosecond pulses to excite the ground state ($v = 0$) H_2^+ to the antibonding state followed by, for example, a KrF 248 nm probe pulse. For a discussion of the practical approach to optical quantum control of molecular dynamics, we refer the reader to the work of Wilson and co-workers [147, 148]. The rates for the $1s\sigma_g^+$ state may be examined by a Raman process or a strong 2-photon excitation of low frequency, though this might cause the bond to break if many photons are absorbed. In the case of H_2^+ the vibrational timescale is short introducing additional experimental difficulties. Alternatively, the REMPI effects reported here may be observed in “slower” systems, such as D_2^+ or Li_2^+ or other alkalis.

We have presented results of calculations of multiphoton ionization rates and field-molecule quasienergies as functions of laser frequency, intensity and internuclear separation. The generalized 6-photon ionization cross-section shows how resonances shift and get quenched as the intensity is increased. Non-perturbative features are seen at intensities above $5 \times 10^{12} \text{ W cm}^{-2}$. For fixed laser frequency and internuclear distance, the AC Stark shift in a particular resonance line explains the sudden increase in the ionization rate presented in table 9.1, as the intensity is increased from 5×10^{13} to $10^{14} \text{ W cm}^{-2}$. Besides

being essential for our discussion of the validity of the 2-state approximation, figures 9.2-9.4 were useful, by identifying resonance positions, in the discussion of the variation in the ionization rate with internuclear separation, shown in figures 9.6, 9.8 and 9.9. Special emphasis was put on the difference in the physical mechanisms belonging to the critical distances with enhanced ionization discussed here and the ones encountered in the low-frequency case. The full assessment of the effects of enhanced ionization through adiabatic nuclear passage of avoided crossings has to await future detailed nuclear dynamics calculations. In connection with figures 9.7-9.9, we also noted that any vibrationally stabilized state could ionize completely within 25 fs in the KrF laser field operated at an intensity of $10^{14} \text{ W cm}^{-2}$. Stabilization of trapped states may, accordingly, only be observed at times shorter than this depletion time, making an experimental verification very difficult.

Additionally, we have presented results which have been compared with existing wavepacket calculations, including a representation of the Floquet wavefunction indicating laser-induced orbital-hybridization. With special reference to figures 9.11 and 9.12, we have shown that the Floquet method permits a very detailed study of the resonance states. This leads to a better understanding of laser-induced avoided crossings and hence fragment ion energy spectra. Regarding the dissociative ionization mechanisms for $\omega \sim 0.2 \text{ au}$, we have emphasized that the existence of critical distances and the consequent enhancement of ionization rates are attributed to REMPI and not CREI. Furthermore, our conjecture is that REMPI processes will be the dominant feature of ionization for $\lambda = 600 \text{ nm}$ and intensities up to $10^{14} \text{ W cm}^{-2}$. The CREI mechanism, although very important in the tunnelling regime, should not be applied as a universal mechanism for enhanced ionization across all frequencies. Our studies seem to indicate an upper limit of about $\gamma \sim 1$ for the validity of the CREI tunnelling model. The correct mechanism is of theoretical interest for a proper description of dissociative ionization. However, it remains to be seen whether an experiment can resolve this question [15].

The Floquet ionization rates have been presented as reliable benchmarks for wavepacket codes. In some implementations of the wavepacket method it has been shown to give results quite different from the Floquet rates. In other cases the agreement is reasonable. Wavepacket methods, particularly those including nuclear dynamics [116, 114], are an extremely powerful tool for the description and analysis of molecular dynamics in intense laser fields. It is hoped that the Floquet method will address such problems in the near future [23].

Chapter X

Finale

This thesis has been concerned with two main topics: laser-assisted electron-atom scattering and multiphoton ionization of H_2^+ . Conclusions and summaries have been given in appropriate chapters. For a short self-contained resumé, the reader is referred to appendix D.

10.1 Outlook

The results presented in this thesis point towards some obvious directions of future work.

10.1.1 Laser-assisted electron scattering

A recent paper by Jaroń and Kamiński [48] attributed the discrepancy between theory and the experimental results of Wallbank and Holmes [26, 27] to off-shell effects. We have initiated a study of off-shell effects in the case of laser-assisted Coulomb potential scattering. In this case the exact field-free off-shell scattering T -matrix is available and a clear assessment of the effect should be possible.

10.1.2 Dissociative ionization of H_2^+

Some obvious extensions of the work presented here would include extension of the Floquet calculations to lower frequencies where more experiments are performed. The extension is not easy from a calculational point of view as many more Floquet blocks are needed. Also the analysis of the quasienergies becomes complicated as many more energies are present.

It would be interesting to calculate high harmonic generation with the Floquet approach to look for two-centre effects in the harmonic spectrum.

Calculation of ionization rates for fixed nuclei as a function of the angle between the laser polarization and the internuclear axis will be of relevance in the discussion of field alignment effects.

The full dissociative ionization dynamics may be studied either by calculating nuclear dynamics on the complex potential energy surfaces obtained by the Floquet approach or by using the wavepacket method. Currently, we are implementing the Floquet approach. It is very cumbersome and time-demanding. Contemplating increasing interest in the short pulse regime (~ 10 fs) the wavepacket approach is to be preferred, as short pulses means short propagation times.

Appendix A

The weak-field soft-photon approximation

In this appendix, we add the four terms $\mathcal{T}^{(0)}$, $\mathcal{T}_a^{(1)}$, $\mathcal{T}_b^{(1)}$ and $\mathcal{T}^{(2)}$ of equations (4.38), (4.42), (4.43) and (4.44) of section 4.1 to obtain the weak-field soft-photon T -matrix element of equation (4.47)

$$\begin{aligned}
\mathcal{T}_l^{\text{WFSP}} &= \mathcal{T}_l^{(0)} + \mathcal{T}_{l,a}^{(1)} + \mathcal{T}_{l,b}^{(1)} + \mathcal{T}_l^{(2)} \\
&= J_l(L) \langle \mathbf{q}_f | V + VG^+(q_i^2/2)V | \mathbf{q}_f \rangle \\
&+ \frac{A_0}{2} (J_{l+1}(L) \langle \mathbf{q}_f | VG^+(q_i^2/2)(\hat{\mathbf{p}} - \mathbf{q}_i) \mathbf{d} G^+(q_i^2/2)V | \mathbf{q}_i \rangle \\
&+ J_{l-1}(L) \langle \mathbf{q}_f | VG^+(q_i^2/2)(\hat{\mathbf{p}} - \mathbf{q}_i) \mathbf{d}^* G^+(q_i^2/2)V | \mathbf{q}_i \rangle). \quad (\text{A.1})
\end{aligned}$$

Here we have used the summation theorems of equations (4.45) and (4.46) and introduced the vector \mathbf{d} of equation (4.7). For notational convenience, we have ignored an overall phase factor, $\exp[-il\tau]$, with τ given by (3.9). The expression we have to consider in order to simplify equation (A.1) is

$$\langle \mathbf{q}_f | VG^+(q_i^2/2)(\hat{\mathbf{p}} - \mathbf{q}_i) G^+(q_i^2/2)V | \mathbf{q}_i \rangle. \quad (\text{A.2})$$

By noting that $\hat{\mathbf{p}} = [\hat{\mathbf{p}}^2 + V, \mathbf{r}]$, and then using the following identities

$$\begin{aligned}
G^+(E) \hat{\mathbf{p}} G^+(E) &= i[G^+(E), \mathbf{r}] \\
\nabla_{\mathbf{q}_f} \langle \mathbf{q}_f | &= \langle \mathbf{q}_f | (-i\mathbf{r}) \\
\nabla_{\mathbf{q}_i} | \mathbf{q}_i \rangle &= (i\mathbf{r}) | \mathbf{q}_i \rangle \\
\frac{\partial}{\partial E} G^+(E) &= -G^+(E)G^+(E),
\end{aligned} \quad (\text{A.3})$$

we obtain

$$\begin{aligned}
&\langle \mathbf{q}_f | VG^+(q_i^2/2)(\hat{\mathbf{p}} - \mathbf{q}_i) G^+(q_i^2/2)V | \mathbf{q}_i \rangle = \\
&(\nabla_{\mathbf{q}_f} + \nabla_{\mathbf{q}_i}) \langle \mathbf{q}_f | VG^+(E)V | \mathbf{q}_i \rangle \\
&+ \langle \mathbf{q}_f | V \mathbf{q}_i \frac{\partial}{\partial E} G^+(E)V | \mathbf{q}_i \rangle |_{E=q_i^2/2}.
\end{aligned} \quad (\text{A.4})$$

For a local potential, V , we have

$$(\nabla_{\mathbf{q}_f} + \nabla_{\mathbf{q}_i})\langle \mathbf{q}_f | VG^+(E)V | \mathbf{q}_i \rangle = 0, \quad (\text{A.5})$$

and we therefore get

$$\begin{aligned} & \langle \mathbf{q}_f | VG^+(q_i^2/2)(\hat{\mathbf{p}} - \mathbf{q}_i)G^+(q_i^2/2)V | \mathbf{q}_i \rangle = \\ & (\nabla_{\mathbf{q}_f} + \nabla_{\mathbf{q}_i})T_{\mathbf{q}_f, \mathbf{q}_i}(q_i^2/2) \\ & + \langle \mathbf{q}_f | V \mathbf{q}_i \frac{\partial}{\partial E} G^+(E)V | \mathbf{q}_i \rangle |_{E=q_i^2/2}, \end{aligned} \quad (\text{A.6})$$

where we have introduced the T -matrix, $T_{\mathbf{q}_f, \mathbf{q}_i}(q_i^2/2)$. Defining the half-shell T -matrix

$$T_{\mathbf{q}_i}(\mathbf{Q}) = \langle \mathbf{q}_f + \mathbf{Q} | V + VG^+(q_i^2/2)V | \mathbf{q}_i \rangle, \quad (\text{A.7})$$

we can express the rhs of equation (A.6) as

$$\begin{aligned} \nabla_{\mathbf{q}_i} T_{\mathbf{q}_i}(\mathbf{Q}) & \equiv (\nabla_{\mathbf{q}_f} + \nabla_{\mathbf{q}_i})T_{\mathbf{q}_f, \mathbf{q}_i}(q_i^2/2) \\ & + \langle \mathbf{q}_f | V \mathbf{q}_i \frac{\partial}{\partial E} G^+(E)V | \mathbf{q}_i \rangle |_{E=q_i^2/2}. \end{aligned} \quad (\text{A.8})$$

Thus, we have

$$\langle \mathbf{q}_f + \mathbf{Q} | VG^+(q_i^2/2)(\hat{\mathbf{p}} - \mathbf{q}_i)G^+(q_i^2/2)V | \mathbf{q}_i \rangle = \nabla_{\mathbf{q}_i} T_{\mathbf{q}_i}. \quad (\text{A.9})$$

Equation (4.47) is derived by inserting (A.9) into equation (A.1).

Appendix B

Inverse iteration and LU decomposition

In this appendix, we outline how to find complex eigenvalues of the Floquet eigenvalue problem iteratively. Inverse iteration has been discussed extensively in the literature [120, 35]. A brief discussion is included for completeness.

Following Potvliege and Shakeshaft [125], we introduce the Floquet Hamiltonian

$$H_{MN} = (H_0 - N\omega)\delta_{N,M} + V_+\delta_{n,M+1} + V_-\delta_{N,M-1}, \quad (\text{B.1})$$

and express equation (8.12) as

$$\sum_M H_{MN}|G_M\rangle = \mathcal{E}|G_N\rangle, \quad (\text{B.2})$$

which gives rise to a sparse tridiagonal matrix equation in Fourier components. Expanding (B.2) in our basis (8.13), and introducing an initial guess, \mathcal{E}_0 , at the eigenvalue, an infinite linear eigenvalue system emerges

$$(\underline{\mathbf{H}} - \mathcal{E}_0\underline{\mathbf{O}})\underline{x} = (\mathcal{E} - \mathcal{E}_0)\underline{\mathbf{O}}\underline{x}. \quad (\text{B.3})$$

In practice, of course, this system is truncated. The number of Floquet blocks and basis functions necessary to obtain converged quasienergies was discussed in section 8. In equation (B.3), \underline{x} is the column vector that consists of all the expansion coefficients, and $\underline{\mathbf{O}}$ is the overlap matrix of the basis functions. Finally, $\underline{\mathbf{H}}$ is the tridiagonal matrix representation of the Hamiltonian, H_{MN} . The photon absorption and emission interaction terms, V_+ and V_- , form blocks adjacent to the diagonal. With our basis (8.13), all the matrix elements of the blocks making up $\underline{\mathbf{H}}$ and $\underline{\mathbf{O}}$ can be evaluated analytically in closed form. The block matrices are also sparse, at most quintidiagonal [23, 9].

The overlap matrix in (B.3) may be decomposed into $\underline{\mathbf{O}} = \underline{\mathbf{L}}\underline{\mathbf{L}}^T$, where $\underline{\mathbf{L}}$ is a lower triangular matrix and $\underline{\mathbf{L}}^T$ is its upper triangular transpose. Matrix multiplication from the left by $\underline{\mathbf{L}}^{-1}$ then gives

$$\underline{\mathbf{A}}\underline{y} = (\mathcal{E} - \mathcal{E}_0)\underline{y}, \quad (\text{B.4})$$

where $\underline{\mathbf{A}} = \underline{\mathbf{L}}^{-1}(\underline{\mathbf{H}} - \mathcal{E}_0 \underline{\mathbf{O}})(\underline{\mathbf{L}}^T)^{-1}$. Equation (B.4) is satisfied by the exact eigenvector and the exact complex eigenvalue. The numerical problem is solved by supplying an initial guess of the eigenvector, \underline{y}_0 , and then solving the linear equations successively

$$\underline{\mathbf{A}} \underline{y}_n = \underline{y}_{n-1}. \quad (\text{B.5})$$

Then the solution \underline{y}_n will be closer to the eigenvector with eigenvalue \mathcal{E} than \underline{y}_{n-1} as may be seen from an expansion in eigenvectors of $\underline{\mathbf{A}}$ [149]. The corresponding improved eigenvalue is found by solving equation (B.4). In practice the initial guess, \underline{y}_0 , can be picked at random [149] as long as it is not exactly orthogonal to the eigenvector. Normally the choice $\underline{y}_0 = (1, 1, 1, \dots, 1)$ followed by normalization will do fine [120].

The diagonalization of the linear system in equation (B.4) can be done very efficiently by taking advantage of the block tridiagonal structure. The matrix $\underline{\mathbf{A}}$ can be factored into lower (L) and upper (U) block matrices. This allows for a sequential diagonalization of the matrix problem with a minimum of storage [120, 35]. As a result, the size of the largest system of inhomogeneous linear equations equals the size of the largest diagonal block. The number of operations scales proportional to the number of Fourier components (Floquet blocks) and proportional to the cube of the size of the diagonal blocks [120].

Our calculations are carried out on the Durham IBM work station cluster. We use the publicly available package ARPACK for finding the eigenvalues iteratively. The linear algebra manipulations are made using subroutines from the ESSL library especially adapted to the IBM architecture. Our software has been modified to allow for an implementation on the Durham Silicon Graphics machine using NAG and ARPACK packages only. For further details on the programs, we refer the reader to [9].

Appendix C

Complex-scaling and complex-basis-function methods

In this appendix, we sketch how to obtain complex eigenvalues by (i) the complex-scaling method, in which the Hamiltonian coordinates are rotated in the complex plane, and the basis functions are represented by real square integrable functions, and (ii) the use of the real Hamiltonian with complex-basis-functions. In either case, the problem involves finding eigenvalues of a non-Hermitian complex symmetric matrix. The method used for the matrix diagonalization is outlined in appendix B.

The complex-scaling method has been extensively described, e.g., in the review by Junker [150]. The complex-basis-function method has been applied successfully to multiphoton ionization processes by Potvliege and Shakeshaft [125] and Plummer and McCann [19] as well as in the work presented in chapter 9. Faisal also gives a short account of the method [35].

The Hamiltonian in equation (8.1), supports no bound states, rather all states are resonances due to the presence of the field and the corresponding coupling to the continuum through the periodic interaction, $V(t)$. As explained in section 8, each field-molecule state is characterized by a complex quasienergy $E = E_0 + \Delta - i\Gamma/2$, where E_0 is the field-free energy, Δ the AC Stark shift, and Γ the total ionization rate. Floquet states shifted in energy by an integral number of angular frequency are describing equivalent physical states. Normally, we chose to consider the state which is adiabatically linked with intensity to the un-shifted field-free state of energy E_0 .

As is well known from scattering theory, a resonance state is characterized by a pole in the S -matrix in the complex energy plane. As the S -matrix describes the ratio of outgoing to incoming waves, this state has no incoming components. The asymptotic wave function is thus proportional to the Siegert state, $e^{ik_p r}$, at the pole $k = k_p$ in the complex k -plane. In the upper half of the complex k -plane, the corresponding solution is thus a normalizable eigenfunction of the Schrödinger equation with energy $k_p^2/2$, and due to the Hermiticity of the Hamiltonian the pole is purely imaginary. Poles in the upper semi-plane

are, accordingly, associated with bound states of the system. Poles in the lower semi-plane are not restricted in the same way, but may be seen to be associated with resonances.

We may gain insight into the the complex-scaling method by studying the behaviour of the Siegert state as the r -coordinate is rotated: $r \rightarrow r_\theta = re^{i\theta}$. Formally, the rotated Hamiltonian has the same solutions as the un-rotated. We specialize to a resonance state (with complex k -value $k_p = ke^{i\alpha}$, $0 \leq -\alpha \leq \pi/2$). Inserting $kre^{i(\alpha+\theta)}$ into the Siegert state, we see that the resonance energy $k_p^2/2$ will belong to the discrete spectrum of the rotated Hamiltonian when $\sin(\alpha + \theta) > 0$, i.e. when $\theta > -\alpha$. The continuum scattering states are on the line $\theta + \alpha = 0$. The bound state spectrum is not influenced by the rotation as long as $0 < -\theta < \pi/2$. The continuum energy spectrum is thus rotated by 2θ into the lower half of the complex energy plane, and complex eigenvalues of the rotated Hamiltonian are revealed in the sector $[-2\theta; 0]$. From the calculational point of view, the calculation of the spectrum is now free from the continuum cuts along the positive real axis. Consequently, the spectrum of the rotated Hamiltonian may be found on a basis of L^2 -functions. In practice the value of the complex rotation, θ , is found by trial and error and stability of results.

The complex-scaling and the complex-basis-function method are equivalent. This may be seen by noting that the matrix elements

$$H_{ij}^\theta = \int dr \psi_i^*(r) H(re^{i\theta}) \psi_j(r) \quad (\text{C.1})$$

encountered in the diagonalization of the rotated Hamiltonian generally may be written as

$$\int_0^\infty dr f(r). \quad (\text{C.2})$$

Integrating now along the closed r -contour: 0 to R , along the semi-circle from R to $Re^{-i\theta}$ and back to 0, we get a zero from Cauchy's integral theorem. The contribution to the integral from the semi-circle is zero as $R \rightarrow \infty$ as the basis functions $\{\psi_i, \psi_j\}$ are square integrable. We therefore get

$$\int_0^\infty dr f(r) = \int_0^{e^{-i\theta}\infty} dr f(r) = e^{-i\theta} \int_0^\infty dr f(re^{-i\theta}), \quad (\text{C.3})$$

and, consequently

$$H_{ij}^\theta = e^{-i\theta} \int dr \psi_i^*(re^{i\theta}) H(r) \psi_j(re^{-i\theta}), \quad (\text{C.4})$$

which shows the equivalence of the two methods.

Appendix D

Resumé

Non-linear laser-matter interactions are studied. In particular, non-perturbative theories of laser-assisted electron-atom scattering processes are discussed. Additionally, multiphoton ionization of the hydrogen molecular ion is studied in detail using the Floquet approach.

Laser-assisted electron-atom scattering processes can be classified as allowed or classically forbidden depending on the scattering geometry, the intensity and frequency of the laser, and on the number of exchanged photons. The applicability of different theoretical models is investigated and it is shown in which regimes these apply. The so-called impulse approximation is valid in both classically allowed and forbidden scattering arrangements. The evaluation of this approximation becomes extremely difficult in cases where closed analytical expressions for the off-shell scattering amplitude are not available. This makes alternative approximation schemes very interesting. The weak-field soft-photon approximation is one such model. It applies in the weak-field regime independently of geometrical constraints. The quality of the weak-field soft-photon theory is in particular high for one-photon exchange processes as substantiated by comparison with exact theoretical calculations and experimental data. The peaked impulse approximation represents a generalization of the celebrated Kroll-Watson approximation of laser-assisted scattering and applies in a wider range of the classically allowed region than the weak-field soft-photon approximation. The peaked impulse approximation fails in the classically forbidden region. A systematic analysis provides a clear identification of the relevant order parameters of the theories.

The weak-field soft-photon approximation is generalized to include atomic potentials which support resonances. In the classically forbidden region, former theories predict laser-assisted electron-atom scattering resonances to appear as pure Breit-Wigner peaks on a vanishingly small background. The present theory includes higher-order terms and shows that the background amplitude may compete with the resonance part to produce characteristic Fano-type resonance signals. Considering tunable radiation fields, it is shown that the laser may induce resonance-interference effects. The shapes of overlapping resonances are

in general determined by an interplay between resonance scattering amplitudes and a laser-controlled contrast parameter. Characteristic spectral features in the laser-induced overlap between fine-structure components are uniquely related to the distinctly different interference properties of direct and spin-flip amplitudes.

The influence of dispersion on quantum interference in two-colour laser-assisted scattering processes is discussed. The dispersion of the initial state of the probe system, be it a quantum object itself or a macroscopic system in a classical interference experiment, is in general an essential element in the analysis of quantum interference phenomena. The general situation is briefly discussed with particular reference to generic cases in two-colour atomic-physics experiments. The effect of dispersion is, at first sight, somewhat counter-intuitive: if the probe is dispersion-free, no interference occurs except in special cases, while *quantum interference* gains full weight in the *classical limit*, where the dispersion is large. Experiments in which a continuous transition between the two regimes may be observed are proposed.

The last part of the thesis is devoted to an investigation of multiphoton ionization of the hydrogen molecular ion. Multiphoton ionization rates from the dressed $1s\sigma_g^+$ and $2p\sigma_u^+$ states are calculated within the non-perturbative Floquet framework. The mechanisms for enhanced ionization in the multiphoton regime are studied as a function of laser frequency, laser intensity *and* internuclear separation. These mechanisms are contrasted with those that apply in the tunnelling regime. For linearly polarized light and parallel transitions, we determine ionization rates for a range of internuclear separations, and a new rich structure of multiphoton resonances is found. These features are not reproduced by quasistatic field models. The values of ionization rates as well as their bond-length dependence are studied and compared with wavepacket calculations where these are available. Differences between results and reasons for discrepancies are discussed. Furthermore, the intensity range of validity of the 2-electronic state model is explored and the question of laser-induced adiabatic stabilization is discussed.

Bibliography

- [1] L. B. Madsen and K. Taulbjerg, *Phys. Rev. A* **52**, 2429 (1995).
- [2] J. L. Peacher, D. H. Madison, R. P. McEachran, and I. Bray, *J. Phys. B: At. Mol. Opt. Phys.* **30**, 3445 (1997).
- [3] A. Weingartshofer, J. K. Holmes, G. Claude, M. Clarke, and H. Krüger, *Phys. Rev. Lett.* **39**, 269 (1977).
- [4] A. Weingartshofer, J. K. Holmes, J. Sabbagh, and S. L. Chin, *J. Phys. B: At. Mol. Phys.* **16**, 1805 (1983).
- [5] T. E. Glover, R. W. Schoenlein, A. H. Chin, and C. W. Shank, *Phys. Rev. Lett.* **76**, 2468 (1996).
- [6] J. M. Schins, P. Breger, P. Agostini, R. C. Constantinescu, H. G. Muller, G. Grillon, A. Antonetti, and A. Mysyrowicz, *Phys. Rev. Lett.* **73**, 2180 (1994).
- [7] D. M. Volkov, *Z. Phys.* **94**, 250 (1935).
- [8] M. Gavrila, ed., *Atoms in Intense Laser Fields* (Academic, Boston, 1992).
- [9] M. Plummer, J. F. McCann, and L. B. Madsen, *Computer Physics Communication*, p. in print (1998).
- [10] K. Codling, L. J. Frasinski, and P. A. Hatherly, *J. Phys. B: At. Mol. Opt. Phys.* **22**, L321 (1989).
- [11] T. Seideman, M. Y. Ivanov, and P. B. Gorkum, *Phys. Rev. Lett.* **75**, 2819 (1995).
- [12] J. H. Posthumus, L. J. Frasinski, M. R. Thompson, W. Shaikh, and K. Codling, *J. Phys. B: At. Mol. Opt. Phys.* **28**, L349 (1995).
- [13] E. Constant, H. Stapelfeldt, and P. B. Gorkum, *Phys. Rev. Lett.* **76**, 4140 (1996).
- [14] J. H. Posthumus, A. J. Giles, M. R. Thompson, W. Shaikh, A. J. Langley, L. J. Frasinski, and K. Codling, *J. Phys. B: At. Mol. Opt. Phys.* **29**, L525 (1996).

- [15] M. R. Thompson, M. K. Thomas, P. F. Taday, J. H. Posthumus, A. J. Langley, L. J. Frasinski, and K. Codling, *J. Phys. B: At. Mol. Opt. Phys.* **30**, 5755 (1997).
- [16] S. Chelkowski, T. Zuo, and A. D. Bandrauk, *Phys. Rev. A* **46**, R5342 (1992).
- [17] F. H. Mies, A. Giusti-Suzor, K. C. Kulander, and K. J. Schafer, *Super-Intense Laser-Atom Physics* (Plenum, New York, 1993).
- [18] T. Zuo and A. D. Bandrauk, *Phys. Rev. A* **52**, R2511 (1995).
- [19] M. Plummer and J. F. McCann, *J. Phys. B: At. Mol. Opt. Phys* **28**, 4073 (1995).
- [20] M. Plummer and J. F. McCann, *J. Phys. B: At. Mol. Opt. Phys* **29**, 4625 (1996).
- [21] M. Plummer and J. F. McCann, *J. Phys. B: At. Mol. Opt. Phys* **30**, L401 (1997).
- [22] L. B. Madsen and M. Plummer, *J. Phys. B: At. Mol. Opt. Phys* **31**, 87 (1998).
- [23] M.-G. Baik, M. Pont, and R. Shakeshaft, *Phys. Rev. A* **54**, 1570 (1996).
- [24] Z. Mulyukov, M. Pont, and R. Shakeshaft, *Phys. Rev. A* **54**, 4299 (1996).
- [25] B. Wallbank and J. K. Holmes, *Phys. Rev. A* **48**, R2515 (1993).
- [26] B. Wallbank and J. K. Holmes, *J. Phys. B: At. Mol. Opt. Phys.* **27**, 1221 (1994).
- [27] B. Wallbank and J. K. Holmes, *J. Phys. B: At. Mol. Opt. Phys.* **27**, 5405 (1994).
- [28] N. M. Kroll and K. M. Watson, *Phys. Rev. A* **8**, 804 (1973).
- [29] F. Ehlotzky, A. Jaroń, and J. Z. Kamiński, *Phys. Rep.* **297**, 64 (1998).
- [30] D. W. Schumacher, F. Weiche, H. G. Muller, and P. H. Bucksbaum, *Phys. Rev. Lett.* **73**, 1344 (1994).
- [31] S. Watanabe, K. Kondo, Y. Nabekawa, A. Sagiasaka, and Y. Kubayashi, *Phys. Rev. Lett.* **73**, 2692 (1994).
- [32] N. J. Mason, *Rep. Prog. Phys.* **56**, 1275 (1993).
- [33] M. H. Mittleman, *Introduction to the Theory of Laser-Atom Interactions* (Plenum, New York, 1982).

- [34] M. H. Mittleman, *Introduction to the Theory of Laser-Atom Interactions* (Plenum, New York, 1993).
- [35] F. H. M. Faisal, *Theory of Multiphoton Processes* (Plenum, New York, 1987).
- [36] I. Rabadán, L. Méndez, and A. S. Dickinson, *J. Phys. B: At. Mol. Opt. Phys.* **27**, L535 (1994).
- [37] I. Rabadán, L. Méndez, and A. S. Dickinson, *J. Phys. B: At. Mol. Opt. Phys.* **29**, 163 (1996).
- [38] L. B. Madsen and K. Taulbjerg, *J. Phys. B: At. Mol. Opt. Phys.* **31**, 4701 (1998).
- [39] A. Weingartshofer, M. Clarke, J. K. Holmes, and C. Jung, *Phys. Rev. A* **19**, 2371 (1979).
- [40] S. Bivona, R. Burlon, R. Zangara, and G. Ferrente, *J. Phys. B: At. Mol. Phys.* **18**, 3149 (1985).
- [41] P. Zoller, *J. Phys. B: At. Mol. Phys.* **13**, L249 (1980).
- [42] S. Geltman, *Phys. Rev. A* **51**, R34 (1995).
- [43] S. Varró and F. Ehlotzky, *J. Phys. B: At. Mol. Opt. Phys.* **28**, 1613 (1995).
- [44] L. B. Madsen and K. Taulbjerg, *J. Phys. B: At. Mol. Opt. Phys.* **28**, 5327 (1995).
- [45] A. Cionga, L. Dimou, and F. H. M. Faisal, *J. Phys. B: At. Mol. Opt. Phys.* **30**, L361 (1997).
- [46] D. Charlo, M. Terao-Dunseath, K. M. Dunseath, and J.-M. Launay, *J. Phys. B: At. Mol. Opt. Phys.* **31**, L539 (1998).
- [47] N. J. Kylstra and J. C. Joachain, *Phys. Rev. A* **58**, R26 (1998).
- [48] A. Jaroń and J. Z. Kamiński, *Phys. Rev. A* **56**, R4393 (1997).
- [49] D. B. Milošević and F. Ehlotzky, *J. Phys. B: At. Mol. Opt. Phys.* **30**, 2999 (1997).
- [50] D. B. Milošević, *J. Phys. B: At. Mol. Opt. Phys.* **28**, 1869 (1995).
- [51] D. B. Milošević, *Phys. Rev. A* **53**, 619 (1996).
- [52] F. Trombetta, *Europhys. Lett.* **15**, 411 (1991).
- [53] L. B. Madsen and K. Taulbjerg, *J. Phys. B: At. Mol. Opt. Phys.* **30**, 1599 (1997).

- [54] Y. N. Demkov and V. N. Ostrovsky, *Zero-range potentials and their application in atomic physics* (Plenum, New York, 1988).
- [55] I. J. Berson, *J. Phys. B: At. Mol. Phys.* **8**, 3078 (1975).
- [56] W. Becker, J. K. McIver, and M. Confer, *Phys. Rev. A* **40**, 6904 (1989).
- [57] W. Becker, S. Long, and J. K. McIver, *Phys. Rev. A* **41**, R4112 (1990).
- [58] W. Becker, S. Long, and J. K. McIver, *Phys. Rev. A* **50**, 1540 (1994).
- [59] M.-Q. Bao and A. F. Starace, *Phys. Rev. A* **53**, R3723 (1996).
- [60] C. Jung and H. S. Taylor, *Phys. Rev. A* **23**, 1115 (1981).
- [61] D. Andrick and H. Bader, *J. Phys. B: At. Mol. Opt. Phys.* **17**, 4549 (1984).
- [62] H. Bader, *J. Phys. B: At. Mol. Opt. Phys.* **19**, 2177 (1986).
- [63] B. Wallbank, J. K. Holmes, S. C. MacIsaac, and A. Weingartshofer, *J. Phys. B: At. Mol. Opt. Phys.* **25**, 1265 (1992).
- [64] U. Fano, *Phys. Rev.* **124**, 1866 (1961).
- [65] K. Taulbjerg, *J. Phys. B: At. Mol. Phys.* **13**, L337 (1980).
- [66] M. Gavrilă and J. Z. Kamiński, *Phys. Rev. Lett.* **52**, 613 (1984).
- [67] M. Gavrilă, *Atoms in Intense Laser Fields* (Academic, Boston, 1992).
- [68] K. C. Kulander, K. J. Schafer, and J. L. Krause, *Atoms in Intense Laser Fields* (Academic, Boston, 1992).
- [69] J. D. Jackson, *Classical Electrodynamics* (Wiley & Sons, Inc., New York, 1962).
- [70] B. H. Bransden and M. R. C. McDowell, *Charge Exchange and the Theory of Ion-Atom Collisions* (Oxford University Press, Oxford, 1992).
- [71] K. Taulbjerg, R. O. Barrachina, and J. H. Macek, *Phys. Rev. A* **41**, 207 (1990).
- [72] E. J. Kelsey and L. Rosenberg, *Phys. Rev. A* **19**, 756 (1979).
- [73] M. Abramowitz and I. A. Stegun, *Handbook of Mathematical Functions* (Dover Publications, Inc., New York, 1965).
- [74] H. R. Reiss, *Phys. Rev. A* **22**, 1786 (1980).
- [75] B. Wallbank and J. K. Holmes, *J. Phys. B: At. Mol. Opt. Phys.* **29**, 5881 (1996).
- [76] D. Andrick and A. Bitsch, *J. Phys. B: At. Mol. Phys.* **8**, 393 (1975).

- [77] M. H. Mittleman, Phys. Rev. A **20**, 1965 (1979).
- [78] S. Varró and F. Ehlotzky, Phys. Rev. A **47**, 715 (1993).
- [79] L. B. Madsen, *Progress report on laser-assisted dynamical processes* (Institute of physics and astronomy, Aarhus, 1996).
- [80] L. B. Madsen and K. Taulbjerg, ICOMP VII, Abstracts **1**, A60 (1996).
- [81] R. J. Glauber, Phys. Rev. **131**, 2766 (1963).
- [82] B. Wallbank, V. W. Conners, J. K. Holmes, and A. Weingartshofer, J. Phys. B: At. Mol. Phys. **20**, L833 (1987).
- [83] B. Wallbank, J. K. Holmes, and A. Weingartshofer, J. Phys. B: At. Mol. Phys. **20**, 6121 (1987).
- [84] F. H. Mies, Phys. Rev. **175**, 164 (1968).
- [85] R. P. McEachran and A. D. Stauffer, J. Phys. B: At. Mol. Phys. **16**, 4023 (1983).
- [86] J. E. Furst, D. E. Golden, M. Mahgerfteh, J. Zhou, and D. Mueller, Phys. Rev. A **40**, 5592 (1989).
- [87] N. H. Brunt, G. C. King, and F. Read, J. Phys. B: At. Mol. Phys. **10**, 1289 (1977).
- [88] D. C. Thompson, Proc. Roy. Soc. A **294**, 160 (1966).
- [89] P. G. Burke and C. J. Joachain, *Theory of Electron-Atom Collisions* (Plenum, New York, 1995).
- [90] L. B. Madsen and K. Taulbjerg, J. Phys. B: At. Mol. Opt. Phys. **30**, L419 (1997).
- [91] L. B. Madsen and K. Taulbjerg, *Photonic, Electronic and Atomic Collisions* (World Scientific Publishing, Singapore, 1998).
- [92] R. P. Feynman, R. B. Leighton, and M. Sands, *The Feynman Lectures on Physics vol 3* (Addison-Wesley, Reading, MA, 1965).
- [93] W. K. Wootters and W. H. Zurek, Phys. Rev. D **19**, 473 (1979).
- [94] O. Carnal and J. Mlynek, Phys. Rev. Lett. **66**, 2689 (1991).
- [95] D. W. Keith, C. R. Ekstrom, Q. A. Turchette, and D. E. Pritchard, Phys. Rev. Lett. **66**, 2693 (1991).
- [96] M. O. Scully, B.-G. Englert, and H. Walther, Nature **351**, 111 (1991).

- [97] T. J. Herzog, P. G. Kwait, H. Weinfurter, and A. Zeilinger, *Phys. Rev. Lett.* **75**, 3034 (1995).
- [98] U. Eichmann, J. C. Bergquist, J. J. Bollinger, J. M. Gilligan, W. M. Itano, D. J. Wineland, and M. G. Raizen, *Phys. Rev. Lett.* **70**, 2359 (1993).
- [99] N. Bohr, *Quantum Theory and Measurement* (Princeton University Press, Princeton, NJ, 1983).
- [100] F. W. Byron, P. Francken, and C. J. Joachain, *J. Phys. B: At. Mol. Phys.* **20**, 5487 (1987).
- [101] G. Kracke, J. S. Briggs, A. Dubois, A. Maquet, and V. Vénierd, *J. Phys. B: At. Mol. Opt. Phys.* **27**, 3241 (1994).
- [102] T. Pfau, S. Spatler, C. Kurtsiefer, C. R. Ekstrom, and J. Mlynek, *Phys. Rev. Lett.* **73**, 1223 (1994).
- [103] A. L'Huillier, another, another, another, another, another, and another, *J. Nonlinear Opt. Phys. Materials* **4**, 647 (1995).
- [104] V. Vénierd, T. Taib, and A. Maquet, *Phys. Rev. A* **54**, 721 (1996).
- [105] K. Codling and L. J. Frasinski, *J. Phys. B: At. Mol. Opt. Phys.* **26**, 783 (1993).
- [106] G. R. Kumar, P. Gross, C. P. Safvan, F. A. Rajgara, and D. Mathur, *Phys. Rev. A* **53**, 2562 (1996).
- [107] G. R. Kumar, P. Gross, C. P. Safvan, F. A. Rajgara, and D. Mathur, *J. Phys. B: At. Mol. Opt. Phys.* **29**, L95 (1996).
- [108] K. Vijayalakshmi, V. R. Bhardwaj, and D. Mathur, *J. Phys. B: At. Mol. Opt. Phys.* **30**, 4065 (1997).
- [109] T. D. G. Walsh, F. A. Ilkov, and S. L. Chin, *J. Phys. B: At. Mol. Opt. Phys.* **30**, 2167 (1997).
- [110] G. N. Gibson, M. Li, C. Guo, and J. Neira, *Phys. Rev. Lett.* **79**, 2022 (1997).
- [111] J. Ludwig, H. Rottke, and W. Sandner, *Phys. Rev. A* **56**, 2168 (1997).
- [112] D. Normand, L. A. Lompré, and C. Cornaggia, *J. Phys. B: At. Mol. Opt. Phys.* **25**, L497 (1992).
- [113] J. H. Posthumus, J. Plumridge, M. K. Thomas, K. Codling, L. J. Frasinski, A. J. Langley, and P. F. Taday, *J. Phys. B: At. Mol. Opt. Phys.* **31**, L553 (1998).

- [114] S. Chelkowski, A. Conjusteau, T. Zuo, and A. D. Bandrauk, Phys. Rev. A **54**, 3235 (1996).
- [115] L. B. Madsen, M. Plummer, and J. F. McCann, Phys. Rev. A **58**, 456 (1998).
- [116] S. Chelkowski, T. Zuo, A. Atabek, and A. D. Bandrauk, Phys. Rev. A **52**, 2977 (1995).
- [117] C. P. Safvan and D. Mathur, J. Phys. B: At. Mol. Opt. Phys. **27**, 4073 (1994).
- [118] M. Brewczyk, K. Rzazewski, and C. W. Clark, Phys. Rev. Lett. **78**, 191 (1997).
- [119] L. V. Keldysh, Sov. Phys. JETP **20**, 1307 (1965).
- [120] A. Maquet, S.-I. Chu, and W. P. Reinhardt, Phys. Rev. A **27**, 2946 (1983).
- [121] R. M. Potvliege and R. Shakeshaft, Phys. Rev. A **40**, 3061 (1989).
- [122] S. L. Chin, C. Rolland, P. B. Gorkun, and P. Kelly, Phys. Rev. Lett. **61**, 153 (1988).
- [123] A. Giusti-Suzor, F. H. Mies, L. F. DiMauro, and E. C. and B Yang, J. Phys. B: At. Mol. Opt. Phys. **28**, 309 (1995).
- [124] H. G. Muller, *Coherence Phenomena in Atoms and Molecules in Laser Fields* (Plenum, New York, 1992).
- [125] R. M. Potvliege and R. Shakeshaft, *Atoms in Intense Laser Fields* (Academic, Boston, 1992).
- [126] J. H. Shirley, Phys. Rev. **138**, B979 (1965).
- [127] B. Piraux and R. Shakeshaft, Phys. Rev. A **49**, 3903 (1994).
- [128] T. E. Sharp, Atomic data **2**, 119 (1971).
- [129] P. G. Burke and V. M. Burke, J. Phys. B: At. Mol. Opt. Phys **30**, L383 (1997).
- [130] J. Zakrzewski and D. Delande, J. Phys. B: At. Mol. Opt. Phys. **28**, L667 (1995).
- [131] E. Huens, B. Pireaux, A. Bugacov, and M. Gajda, Phys. Rev. A **55**, 2132 (1997).
- [132] M. Gajda, B. Pireaux, and K. Rzazewski, Phys. Rev. A **50**, 2528 (1994).
- [133] B. Piraux and R. M. Potvliege, Phys. Rev. A **57**, 5009 (1998).

- [134] K. C. Kulander, F. H. Mies, and K. J. Krause, *Phys. Rev. A* **53**, 2562 (1996).
- [135] C. R. Holt, M. G. Raymer, and W. P. Reinhardt, *Phys. Rev. A* **27**, 2971 (1983).
- [136] C. Cohen-Tannoudji, J. Dupont-Roc, and G. Grynberg, *Photons et atomes: Introduction à l'électrodynamique quantique* (InterEditions/Editions du CNRS, Paris, 1987).
- [137] E. Cormier and P. Lambropoulos, *J. Phys. B: At. Mol. Opt. Phys.* **29**, 1667 (1996).
- [138] R. Shakeshaft, *Z. Phys. D: At. Mol. and Clusters* **8**, 47 (1988).
- [139] L. D. Landau and E. M. Lifshitz, *Quantum Mechanics* (Pergamon, New York, 1977).
- [140] T.-S. Ho and S.-I. Chu, *Chem. Phys. Lett.* **141**, 315 (1995).
- [141] H. C. Day, private communication (1997).
- [142] A. Giusti-Suzor and F. H. Mies, *Phys. Rev. Lett.* **68**, 3869 (1992).
- [143] M. Plummer and J. F. McCann, *J. Phys. B: At. Mol. Opt. Phys.* **28**, L119 (1995).
- [144] R. M. Potvliege, private communication (1997).
- [145] D. E. Manolopoulos, *Numerical grid methods and their application to Schrödinger's Equation* (Kluwer Academic, The Netherlands, 1993).
- [146] D. R. Bates, K. Ledsham, and A. L. Stewart, *Phil. Trans. Roy. Soc. London* **246**, A215 (1953).
- [147] J. L. Krause, R. M. Whitnell, K. R. Wilson, Y. Yan, and S. Mukamel, *J. Chem. Phys.* **99**, 6562 (1993).
- [148] B. Kohler, V. V. Yakovlev, J. Che, J. L. Krause, M. Messina, K. R. Wilson, N. Schwenter, R. M. Whitnell, and Y. Yan, *Phys. Rev. Lett.* **74**, 3360 (1995).
- [149] W. H. Press, S. A. Teukolsky, W. T. Vetterling, and B. P. Flannery, *Numerical Recipes in Fortran* (Cambridge University Press, Cambridge, 1986).
- [150] B. R. Junker, *Adv. At. Mol. Phys.* **18**, 207 (1982).